A THEORETICAL STUDY ON THE PERFORMANCE OF SURFACE PLASMON RESONANCE SENSOR FOR HEALTHCARE APPLICATION

Thesis Submitted for the Award of the Degree of

DOCTOR OF PHILOSOPHY

in

PHYSICS

By

Tanwin Mohammad Salauddin Ashrafi

Registration Number: 42000027

Supervised By

Dr. Goutam Mohanty (23352)

Department of Physics (Assistant Professor)

Lovely Professional University

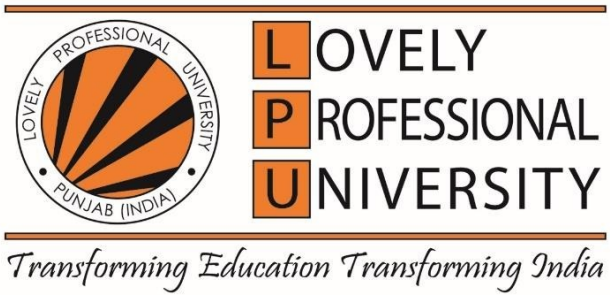

LOVELY PROFESSIONAL UNIVERSITY, PUNJAB

2025

DECLARATION

I, hereby declared that the presented work in the thesis entitled "A theoretical study on the performance of surface plasmon resonance sensor for healthcare application" in fulfilment of degree of **Doctor of Philosophy (Ph. D.)** is outcome of research work carried out by me under the supervision of Dr. Goutam Mohanty, working as Assistant Professor, in the Department of Physics, School of Chemical Engineering and Physical Sciences of Lovely Professional University, Punjab, India. In keeping with general practice of reporting scientific observations, due acknowledgements have been made whenever work described here has been based on findings of other investigators. This work has not been submitted in part or full to any other University or Institute for the award of any degree.

(Signature of Scholar)

Name of the scholar: Tanwin Mohammad Salauddin Ashrafi

Registration No.: 42000027

Department/school: Department of Physics, School of Chemical Engineering and Physical Sciences

Lovely Professional University,

Punjab, India

CERTIFICATE

This is to certify that the work reported in the Ph. D. thesis entitled "A theoretical study on the performance of surface plasmon resonance sensor for healthcare application" submitted in fulfillment of the requirement for the award of degree of **Doctor of Philosophy (Ph.D.)** in the Department of Physics, School of Chemical Engineering and Physical Sciences, is a research work carried out by Tanwin Mohammad Salauddin Ashrafi, 42000027, is bonafide record of his/her original work carried out under my supervision and that no part of thesis has been submitted for any other degree, diploma or equivalent course.

Goutam Mohanty

(Signature of Supervisor)

Name of supervisor: Dr. Goutam Mohanty

Designation: Assistant Professor

Department/school: Department of Physics, School of Chemical Engineering and Physical Sciences

University: Lovely Professional University,

ABSTRACT

Surface Plasmon Resonance (SPR) is a phenomenon occurring when transverse magnetic (TM) polarized light strikes a metal-dielectric interface at a specific angle, causing collective oscillations of free electrons (plasmons) on the surface. This resonance leads to an attenuation in the reflected light, which is highly sensitive to changes in the refractive index (RI) of the medium surrounding the interface. Widely used in biosensing, SPR detects molecular binding events on the sensor surface by monitoring shifts in resonance angle or intensity, enabling real time analysis of biomolecular interactions. Its high sensitivity, label free detection, and real time monitoring capabilities make SPR a powerful tool in various fields including biophysics and medical diagnostics. In the present thesis, the combination of III-V wurtzite nitrides and 2-dimensional (2D) materials is explored to enhance the overall performance of SPR based sensors. Here the overall performance is analyzed in terms of sensitivity, detection accuracy (DA), full width at half maxima (FWHM), figure of merit (FOM) and evanescent electric field (EF) intensity. To compute these parameters, the N-layer transfer matrix method (TMM) is employed and is implemented in high level computational environments such as MATLAB and the COMSOL Multiphysics environment. Furthermore, the study moves beyond theoretical analysis to practical applications, showing the effectiveness of Wurtzite Nitride - TMDC heterostructures in detecting honey adulteration.

In the initial phase, different SPR configurations are optimized through the incorporation of various materials for the prism (Sapphire, BK7, SF10, SF11, and SF5) and different active noble metals (Silver, Gold, and Copper). This study is carried out in the presence of an alcoholic sensing medium at varying concentrations (0%, 20%, 50%, 80%, and 100%). Analysis of the SPR sensor's performance reveals that the BK7 based configuration exhibits the highest sensitivity across all noble metals, with sensitivity peaking at 80% alcohol concentration. Additionally, among active metals, Gold (Au) demonstrates the highest sensitivity compared to Silver (Ag) and Copper (Cu) in all SPR configurations.

In the second phase, the study integrates different heterostructures, combinations of semiconductor and 2D materials, for the analysis of SPR sensor’s performance. In this context, semiconductors used are silicon (Si) and III-V nitrides (i.e., Aluminium

Nitride (AlN), Gallium Nitride (GaN) and Indium Nitride (InN)). The 2D materials are considered Graphene and Transition Metal Dichalcogenide (TMDC) materials (i.e., Molybdenum Disulfide (MoS_2), Tungsten Disulfide (WS_2), Molybdenum Diselenide ($MoSe_2$), and Tungsten Diselenide (WSe_2)). In the first step, the performance is analyzed using the heterostructure of GaN-2D materials between Silver and sensing medium in the SPR configuration. The findings indicate that incorporating GaN enhances sensitivity by 32.60% compared to silicon, while WS_2 improves it by a factor of 8.55% relative to other family members of TMDC. Moreover, the estimated value of sensitivity for the GaN-WS_2 based structure of SPR sensor is highest among all other configurations, with value of 186.59 (°/RIU). Also, other parameters such as DA, FOM and EF enhancement factor outperform other semiconductor-TMDC based SPR configurations. In the second step, the performance is analyzed utilizing AlN-2D materials heterostructure between Silver and sensing medium in the SPR configuration. It is observed that AlN-WS_2 based SPR structure outperforms other configurations with highest sensitivity and superior values of DA, FOM and EF at sensor interface. In the third step, the performance is analyzed using InN-2D materials heterostructure between Silver and sensing medium in the SPR configuration. It is observed that InN-WS_2 based SPR structure outperforms other configurations with highest sensitivity 175.838 (°/RIU), and superior values of DA, FOM and EF at sensor interface. Finally, the comparative study reveals that the heterostructure GaN-WS_2, AlN-WS_2 and InN-WS_2 gives an effective impact on the overall performance parameters of the Ag based SPR configuration.

In the third phase, the study extended to check the overall performance by incorporating the heterostructure AlN-TMDC on the surface of Ag-Au bimetal surface of SPR configuration. Here bimetal layer is optimized with 46 nm Ag and 4 nm Au by looking at the SPR reflectance minima and competitive FWHM value. The analysis reveals that the AlN-WS_2 heterostructure on bimetal based SPR configuration shows better performance in comparison to other AlN-TMDC heterostructures. The values of sensitivity and FOM are 179.00063 (°/RIU) and 46.134 (RIU^{-1}), respectively, with a DA value of 0.7293.

Abstract

The study expands its scope by utilizing proposed SPR structure built with III-V Nitride and WS_2 heterostructures for detecting honey adulteration. The experimental measurement of refractive indices in various adulterated honey samples is followed by a thorough computational study, which includes an in-depth investigation of overall sensor performance. The InN-WS_2 heterostructure-based SPR sensor exhibits a significant shift in resonance angle, providing notable sensitivity for detecting honey adulterants compared to other heterostructure based SPR configurations. Its maximum magnitude of EF at the interface makes InN-WS_2 a suitable choice for constructing a highly sensitive, accurate, and reliable SPR sensor for honey screening.

In summary, the present work introduces an innovative strategy to enhance SPR sensor performance by incorporating different heterostructures, particularly III-V Nitride semiconductors and TMDC materials. The pioneering aspect of this study lies in the shift from theoretical research to practical applications, demonstrating the effectiveness of the proposed SPR sensor in detecting honey adulteration, addressing real world biosensing challenges in food safety.

ACKNOWLEDGEMENT

I would like to express my deepest gratitude to my research guide, Dr. Goutam Mohanty, for giving me the opportunity for me to pursue a higher education under his guidance. His unwavering support, insightful advice, and continuous motivation help me throughout my academic journey. I will continue to apply the research ethics and skills that I have learned from him in my future endeavors.

I extend my heartfelt appreciation to G.M. Momin Women's College for their meaningful support during this remarkable journey. I am grateful to my family for their prayers and continuous support, without which I would not have accomplished this important milestone in my life. Their faith in my abilities has been a constant source of inspiration, and I am truly grateful for the sacrifices they have made to support me in this quest.

Finally, I am grateful to Almighty Allah for keeping me safe and directing me towards the right route during moments of uncertainty.

TABLE OF CONTENTS

Table of Contents

Table of Contents

LIST OF TABLES

LIST OF FIGURES

List of Figures

List of Figures

LIST OF ABBREVIATIONS

ATR	: Attenuated Total Reflection
AuNPs/T	: Thymine-Modified Gold Nanoparticles
BLG	: β-Lactoglobulin
COMSOL	: COMputational SOLutions
CPU	: Central Processing Unit
DA	: Detection Accuracy
DNA	: Deoxyribonucleic acid
E. coli	: Escherichia coli
EF	: Electric Field
EM	: Electromagnetic Wave
EW	: Evanescent Wave
FOM	: Figure of Merit
FWHM	: Full Width at Half Maximum
FSS	: Financial Sector Surveillance
H1N1	: Influenza A Virus
HAV	: Hepatitis A Virus
He-Ne	: Helium Neon
HWHM	: Half Width at Half Maximum
mAb	: Monoclonal Antibodies
MATLAB	: Matrix Laboratory
MXene	: 2D transition metal carbide and nitride
NG	: Not Given
NIR	: Near-Infrared Region

List of Abbreviations

NP	: Nucleoprotein
RI	: Refractive Index
RIU	: Refractive Index Unit
RNA	: Ribonucleic acid
Rmin	: Minimum Reflection Intensity
SAM	: Self-Assembled Monolayer
SARS-CoV-2	: Severe Acute Respiratory Syndrome Coronavirus 2
SP	: Surface Plasmon
SPP	: Surface Plasmon Polariton
SPR	: Surface Plasmon Resonance
SPR-HAVP1	: Surface Plasmon Resonance- Hepatitis A Virus Major Polyoma Virus Capsid Protein
SPW	: Surface Plasmon Wave
TE	: Transverse Electric
Ti3C2Tx	: Titanium Carbide
TIR	: Total Internal Reflection
TM	: Transverse Magnetic
TM- mAb	: Thrombomodulin Monoclonal Antibodies
TMDC	: Transition-Metal Dichalcogenide
TMM	: Transfer Matrix Method
VP1	: Major Polyoma Virus Capsid Protein
2D	: 2-dimensional

LIST OF SYMBOLS

c	: Speed of Light in Vacuum
ε_0	: Permittivity of Vacuum
μ_0	: Free Space Permeability
ω	: Angular Frequency
ω_p	: Angular Plasma Frequency
n	: Refractive Index
$\vec{E}$	: Electric field intensity
$\vec{D}$	: Dielectric displacement
$\vec{B}$	: Magnetic flux density (magnetic field)
$\vec{H}$	: Magnetic field intensity (magnetic field)
E_i	: Amplitude of Incident light Electric field intensity
E_r	: Amplitude of Reflected light Electric field intensity
E_t	: Amplitude of Transmitted light Electric field intensity
ε_r	: Relative Permittivity of material
$\varepsilon(\omega)$	: Relative complex permittivity
ε_1	: Dielectric constant of the metal
ε_2	: Dielectric constant of the dielectric
$\chi(\omega)$	: Electric Susceptibility

List of Symbols

λ	: Wavelength
θ	: Angel of Incident
θ_R	: Angle of Resonance
β	: Propagation Constant
γ	: Damping Factor
k_0	: Propagation wave vector in vacuum
k_{sp}	: Surface plasmon wave vector
$\Delta\theta$	: Shift in resonance angle
ρ_{ext}	: External charge density
M	: Transfer matrix$^{\rightarrow}$
r	: Reflection coefficient vector
r_p	: Reflection coefficient vector for p mode
t_p	: Transmission coefficient vector for p mode
P	: Power of incident light
R	: Reflectance
I_i	: Incident Light Intensity
I_r	: Reflected Light Intensity
I_t	: Transmitted Light Intensity

CHAPTER 1

INTRODUCTION

This chapter serves as a comprehensive introduction to the multifaceted realm of biosensors, with a particular focus on Surface Plasmon Resonance sensors. The research objectives are structured and centred on enhancing the overall performance of SPR sensors. The subsequent structure of the thesis is detailed, providing a roadmap for the study.

Chapter 1

1.1 Introduction

A sensor is an instrument used to change a physical/chemical quantity into a noticeable and quantifiable signal [1]. We regularly come across different types of sensors in our daily lives, and this happens frequently, sometimes without us realizing it. These sensors dominate the world in which we live. The basic scheme of a typical sensor is essential for understanding how sensors convert physical signals into useful data for analysis and display. To illustrate this, Fig 1.1 presents the basic scheme of a typical sensor, breaking it into five key components.

Fig. 1.1 Functional flow diagram of a typical sensor and its components.

As shown in Fig. 1.1, the typical sensor consists of five components: physical signals, sensing element or transducer, associated electronic or signal conditioning, data analysis, and output display. The system detects physical signals, such as temperature, pressure, light, chemical concentration, or biological interaction, through a sensing element. The raw signal is processed through signal conditioning processes, such as amplification, filtering, or analog-to-digital conversion, to improve its quality and compatibility with subsequent stages. The conditioned signal is then analyzed and interpreted using algorithms or computational methods to extract relevant information. The final processed data is converted into a form that is easily understandable or actionable, such as a visual display, audible alarm, or a digital signal transmitted to a control system for further action. Not only are sensors crucial for many academic research endeavors, but they also play a pivotal role in modern industries, with applications in food production and routine monitoring activities such as medical therapeutics, water quality, air quality, transport, and numerous others. Among the countless sensors, Surface Plasmon Resonance (SPR) sensors have evolved significantly

since their inception in 1983 as a tool for gas detection and biomolecular interaction monitoring [2–4].

Researchers have investigated many ways to improve the capabilities of SPR based sensors during the past few decades, leading to groundbreaking developments in the field. This study provides a comprehensive exploration of the advancements in SPR technology, focusing on innovative materials, structural configurations, and their applications in different sensing scenarios.

This work first investigates various noble metals, bimetallic layers, and prism materials with the purpose of optimizing SPR based sensors. The integration of innovative materials, such as semiconductors like wurtzite nitride and two dimensional (2D) materials like Transition Metal Dichalcogenides (TMDCs) is examined further for enhancement in sensor performance. Further, the study addresses food adulteration to detect contaminants in the food using proposed SPR sensors that incorporate wurtzite nitride semiconductor material and tungsten disulfide (WS_2) for heightened sensitivity and accuracy. This study highlights the ongoing evolution of SPR technology, paving the way for future advancements in sensing applications.

1.2 Brief History of Biosensors

Biosensors, which work as analytical devices converting biological responses into electric signals, have a significant history rooted in the invention of the Clark oxygen electrode by Leland Clark. This pioneering device is acknowledged as the first biosensor [5]. Biosensors operate on the principle of converting a biological response into a measurable electric signal.

Biosensors operate by capturing the interaction of target analytes with biomolecular recognition elements (BRE) such as antibodies, nucleic acids, enzymes, bacteria, and viruses. This interaction is measured in real time, and BRE can be immobilized on the transducer's surface [6]. A biosensor combines a biological component, such as enzymes or antibodies, with an electrical component to produce

measurable signals. This electronic component monitors, records, and transmits data based on physiological changes or the presence of different biological or chemical compounds in the surrounding environment.

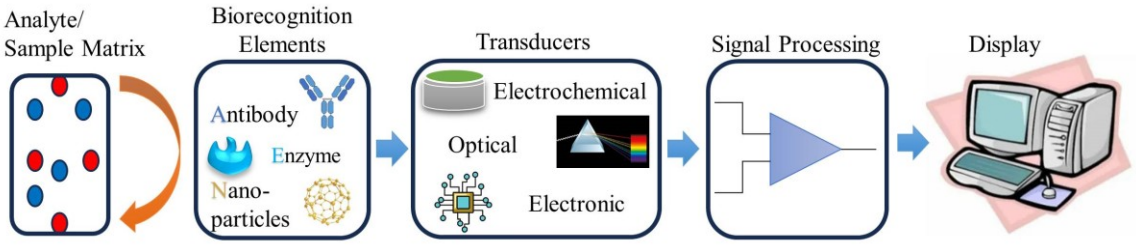

Fig. 1.2 Fundamental components of a typical biosensor

The fundamental components of a typical biosensor are shown in Fig. 1.2. The component of typical biosensor includes:

- *Analyte or Sample Matrix*: The substances of concern, such as glucose, alcohol, or ammonia, whose components are being identified or discovered.
- *Biorecognition Elements*: A biomolecule or biological element that has the ability to recognize the target analyte. Antibodies, RNA or DNA, and enzymes are examples of it. The interaction between BRE with analytes produces signals in a variety of forms, including, heat, charge or mass change, light, and microbial products. This process is known as Biorecognition.
- *Transducer*: This device plays a crucial role in biosensors, converting the biorecognition affair into a measurable electrical signal. Transducers can be categorized broadly as electrochemical, optical, thermal, and electronic depending on the operating principle.
- *Signal Processing Unit:* The signal that has been transduced is processed and prepared appropriately for display. The transducer's electrical signals are amplified and converted to digital form. This processing is necessary for quantifying the signals and processing them for interpretation.
- *Display:* The display unit, typically a computer or printer, serves as the user interpretation system. It generates output in numerical, graphical, or tabular

formats, making the corresponding response readable and understandable to the user. The format of the output can be customized to meet the end user's specific requirements. Overall, biosensors play a vital role in real time monitoring and detection of target substances, finding applications across various industries and sectors [7].

Biosensors, instrumental in translating biological recognition events into measurable signals, are categorized based on their transducers, as shown in Fig. 1.3. These encompass electrochemical, optical, thermal, electronic, and gravimetric biosensors. Optical biosensors a significant subset of biosensors, have witnessed substantial advancements impacting various applications.

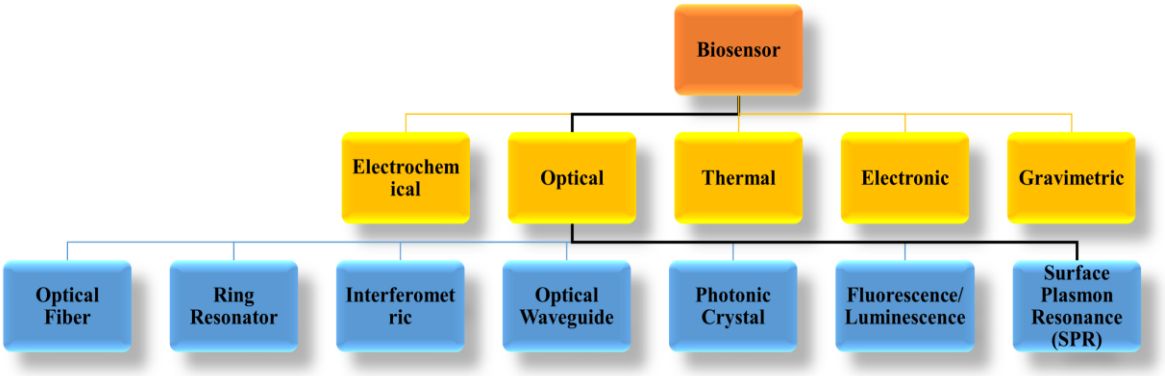

Fig. 1.3 Classification of biosensor

Optical biosensors utilize light for operation and play a pivotal role in medical diagnostics, environmental monitoring, and food safety. This type of biosensors includes diverse structures such as Optical Fiber, Ring Resonator, Interferometric, Optical Waveguide, Photonic Crystal Fluorescence/Luminescence and SPR Biosensors [8]. Broadly, optical biosensors can be categorized into two groups based on their functional roles: sensing platforms and sensing techniques. Sensing platforms refer to physical structures or systems that facilitate the sensing process, such as optical waveguides, Ring resonator, Optical waveguides, Optical fiber, and Photonic crystals serving as the foundation for interaction between the target and the sensor. In contrast, sensing techniques are specific methods employed to detect or measure the target analyte, like

fluorescence, surface plasmon resonance, or Raman scattering, which define how the interaction is analyzed to yield meaningful data. These optical biosensor types underline diverse structures and functionalities, emphasizing ongoing developments in sensitivity, miniaturization, and versatility. SPR Biosensors, a pivotal type of optical biosensors, play a distinctive role in this scenario. This type of sensor involves surface plasmon waves (SPWs) at the metal-dielectric interface, showcasing breakthroughs in material application for improved specificity and sensitivity. For an in-depth exploration of the principles of plasmons, Surface Plasmon Polaritons (SPP), and the Lorentz-Drude Model provides a profound enhancement to one's understanding of the underlying physics that governs SPR, discussed in chapter 2. The trajectory of optical biosensing, particularly SPR, is poised for innovation and integration with emerging technologies in the forthcoming decade.

1.3 Motivation

The motivation behind the proposed research in biosensors stems from a dynamic interplay of factors within the realms of modern science and industry. With a greater focus on life sciences achievements, there is a growing demand for advanced molecular detection technologies. Biosensors, particularly SPR sensors are among the most prominent molecular sensing devices, offer a wide range of applications, including gas detection, chemical sensing, and biomolecular sensing. In healthcare, SPR sensors have improved diagnostics by allowing real-time and label-free detection of biomarkers, hence promoting early detection of diseases and personalized medication. Their higher sensitivity and specificity make them indispensable tools in disease diagnosis, measuring treatment effectiveness, and drug development. The search for improvement in sensitivity and accuracy in measurements motivates the need to improve the overall performance parameters of traditional SPR sensors. Beyond healthcare, biosensors play a pivotal role in various industries, including food processing, environmental monitoring, and quality control. The proposed research, focused on integrating wurtzite nitrides and 2D materials into SPR sensors, promises to elevate their sensitivity and accuracy across a spectrum of

scenarios, thereby contributing to the continual advancement of analytical science and its applications.

1.4 Objective of the Present Research

- To study theoretically the nature of reflectance and plasmon dip for different prism material based SPR configuration.
- To study theoretically the nature of reflectance variation with the introduction of two-dimensional material in the different noble metal based SPR configurations.
- To investigate the variation of plasmon dip and hence sensitivity in the presence of 2D-materials in single metal/ bimetallic SPR structure.
- To analyze theoretically the effect of various wurtzite nitride semiconductors and their alloys on the performance of SPR sensors.
- To explore the effect of wurtzite nitrides semiconductor and its alloys on the overall performance of SPR sensor for healthcare applications.

1.5 Structure of the Thesis

In this subsection, the organization and layout of thesis are delineated, offering readers a navigational guide through its content.

Chapter 1 Introduction

The chapter begins with an introduction that delineates the significance of sensors in daily life, their prevalence in industrial applications, and an overview of SPR sensors. The subsequent section delves into a brief history of biosensors. The chapter provides context for the proposed research. The motivation and specific objectives of the present research are outlined in this chapter. Finally, the chapter concludes by the thesis outline.

Chapter 2 Theoretical background of surface plasmon resonance and literature review

The chapter offers an extensive review of SPR, exploring its fundamental concepts, the electromagnetic theory of SPR, and the dispersion relation. It delves into

the principles of plasmons, surface plasmon (SP) and SPP, introducing the Lorentz-Drude model to enhance the understanding of SPR. The investigation extends to the metal-dielectric interface for exciting surface waves, and the utilization of Attenuated Total Reflection (ATR) is also examined. The chapter explores the application of SPR in detection sensor systems. This chapter serves as the cornerstone for comprehending SPR, laying the essential groundwork for subsequent chapters. The literature review offers an inclusive overview of the properties and research history of metal/bimetal, 2D materials (Graphene, TMDC), and III-V nitrides, setting the groundwork for a deeper understanding of these materials in SPR research.

Chapter 3 Computational Methodology

This chapter focuses on the possible practical structure of SPR based sensors. It explores innovative approaches to enhance sensor performance. The chapter explores innovative strategies, incorporating combinations of wurtzite nitride semiconductors with 2D materials and advanced structural designs to improve sensor capabilities. Various prism materials, metals, and configurations involving wurtzite nitride semiconductor and 2D materials are scrutinized. To assess sensor parameters, numerical models are utilized. The chapter provides a comprehensive exploration of advancements in SPR technology, emphasizing the role of novel materials and structural configurations in enhancing sensor performance.

Chapter 4 Optimization of SPR Configurations: Exploring the Influence of Noble Metals and Prism Materials

This chapter specifically examines how the sensitivity of SPR sensors varies based on different prism materials when subjected to an alcoholic sensing medium. The study compares sensitivity across various prism materials and noble metals, with a particular emphasis on the influence of high refractive index prism materials. The results indicate that prism materials with low refractive indices result in a maximum shift in resonance angle compared to those with high refractive indices. This substantial shift in resonance angle corresponds to the highest sensitivity of the sensor.

Chapter 5 Enhancement of SPR Performance: Investigating the Impact of III-V Group Nitrides in Conjunction with 2D Materials

This theoretical exploration conducts a comparative study aimed at optimizing SPR sensor performance by integrating varied heterostructures between different semiconductors and 2D materials. It compares the efficiency of different semiconductor and 2D material combinations, highlighting the potential of GaN-WS_2, AlN-WS_2, and IN-WS_2 heterostructures. The chapter provides comparative insights into heterostructures for enhancing SPR sensor performance.

Chapter 6 Performance of SPR sensor in the presence of various heterostructures on the single/ bimetal surface

This chapter delves into the functionality of single/bimetal based SPR sensors. It explores the design of bimetallic structures, emphasizing the advantages of the Ag-Au bimetallic SPR structure. The study highlights the use of aluminum nitride (AlN) and TMDC in a heterostructure, enhancing sensor stability and responsiveness. The outcomes reveal the benefits of bimetallic structures over single metallic layers.

Chapter 7 Application: Detection of honey adulteration using III-V nitride and Tungsten Disulfide based SPR sensor

This chapter applies the developed SPR sensor designs to address a real world problem detecting honey adulteration. It explores the utilization of wurtzite nitride semiconductor material with WS_2 in SPR sensor design. The proposed sensor, particularly InN-WS_2 based, demonstrates high sensitivity and strong evanescent electric field (EF), surpassing alternative structures. The study aims to contribute to the development of highly sensitive SPR sensors for detecting honey adulteration in the biomedical and food industries.

Chapter 8 Conclusion and Future Aspects

In conclusion, this research has covered the foundational aspects of SPR sensors, establishing a theoretical framework that sets the stage for advancements. The

computational methodology revealed innovative strategies, incorporating novel materials and designs to enhance SPR sensor performance. Optimization efforts explored the influence of noble metals, prism materials, and heterostructures, emphasizing specific configurations and materials for maximizing sensor sensitivity. The practical application focused on addressing honey adulteration, where the InN-WS_2 based SPR sensor demonstrated exceptional sensitivity. Moving forward, the research opens doors for additional exploration, particularly in discovering further synergies within the promising combination of III-V Nitrides and 2D materials.

CHAPTER 2

THEORETICAL BACKGROUND OF SURFACE PLASMON RESONANCE AND LITERATURE REVIEW

This study explores the principles of SPR sensors and their applications. It delves into plasmonic concepts, including SPP based on the Lorentz-Drude Model, offering insights into electron behavior in metallic materials. The wave equation and geometric aspects of the metal-dielectric interface to excite surface waves are also covered in this study. Dispersion relations are examined for exciting surface plasmons. ATR is explored as a method to excite SPP. The later sections focus on practical applications of SPR based sensors, laying the groundwork for future advancements in research and technology.

Chapter 2

2.1 Introduction

Surface plasmon resonance (SPR) is a powerful optical biosensor that utilizes SPWs for detection and has several applications in chemical research, environmental monitoring, and biological sensing. The chapter discussed the theoretical background of SPR, introducing specific concepts such as plasmon waves and surface plasmon polariton (SPP). Additionally, it explored the application of the Lorentz-Drude model to understand the behaviour of charge in metals. Next, it delves into the interaction of electromagnetic waves (EMs) with the metal-dielectric interface. The discussion on dispersion relations and the stimulation of SPP are explored in depth within the chapter.

Moreover, the chapter also delves into the different methods of exciting SPPs, such as prism coupling and attenuated total reflection (ATR). It highlighted the importance of these methods in studying the properties of various plasmonic materials for exciting SPP. These methods serve as invaluable tools for probing the unique characteristics of materials such as semiconductors and two-dimensional (2D) materials, providing deep insights into their behaviour and potential applications in this field. Finally, the chapter continues by discussing current research trends and future directions in the study of SPR, emphasizing the on going advancements in this area of study. A solid grasp of these fundamental concepts of SPR is essential for the development of biosensors and other applications such as environmental monitoring and food safety. In summary, this chapter offers a comprehensive overview of the theoretical framework that underpins the field of SPR. It also highlights the key advancements and current challenges in the field.

2.2 Surface Plasmon Resonance (SPR)

In 1902, when Wood illuminated a metallic diffraction grating on a mirror with polarized light, he made a significant observation. He noticed the appearance of narrow bright and dark bands in the diffracted light spectrum. This remarkable event marked the first documented observation of SPR, a pivotal discovery that laid the foundation for a wide range of applications in optics, sensing, and spectroscopy [9,10]

. Building on this discovery, significant progress was achieved in SPR technology in the following decades. The first attempt to make SPR an effective tool in chemical sensing made in 1983 in an experiment for gas detection and biomolecular interaction monitoring [11]. This event was a crucial turning point in the application of SPR for practical objectives.

Further progress achieved in 1990 with development of multilayer CO sensor system with the SPR technique. which is studied with computer simulation and later verified with experimental results [12]. By 1993, SPR had broadened its applications to include the development of fiber-optic remote temperature sensors, demonstrating its adaptability beyond conventional sensing applications [13]. These advancements not only broadened the range of SPR technology but also facilitated its extensive use across several fields. Over time, it has flourished as a pivotal tool in the field of biosensing, revolutionizing our ability to detect and analyze biological molecules and interactions [14].

An SPR sensor device typically comprises three main components: an optical system, supporting electronics, and a sensor data acquisition and processing system. The optical system initiates the excitation of surface plasmons (SP), leading to the generation of an output light wave, which is subsequently detected and processed by the supporting electronics. The encoded SPR signal carried by this output light wave acts as the sensor data acquisition [9]. The detector signal is converted into a sensor output signal with the help of processing system. These properties led to the development of SPR based analytical instruments as a new tool for studying molecular interactions.

2.2.1 Basic concept of Plasmon

Plasmons are triggered by specific optical frequencies and represent the cohesive vibrations of the electron cloud within metals in relation to stationary positively charged ions. Plasmons can be excited because of interactions between photons and the electron cloud within metals. Plasmon can be found in the bulk or at surface of conducting materials, as well as in the vicinity of conducting particles [15].

Plasmons can be considered as quasiparticles because they result from the quantization of plasma oscillation.

2.2.2 Surface Plasmons Polariton (SPP) / Surface Plasmon Wave (SPW)

When an electromagnetic wave (EM) travels through a material medium, its electromagnetic field induces polarization within the medium. These induced polarizations lead to the mechanical displacement of charges, resulting in a coupling between the electromagnetic field and the charges. This coupled phenomenon is referred to as polariton [16,17]. A surface plasmon polariton (SPP), also known as a surface plasmon wave (SPW), is a unique phenomenon that occurs when an EM propagates along the line of contact of dielectric material and metal. In this scenario, the EW behaves akin to quasi-free electron plasma, leading to the formation of an SPP or SPW. This coupled excitation is characterized by the collective oscillation of electrons at the dielectric-metal interface, resulting in a distinctive surface wave [18]. SPP are indeed two-dimensional EMs, propagate along the boundary between metal and dielectric medium. The study of metal-dielectric interfaces has become critical, but understanding the phenomenon of polariton through the Lorentz-Drude Model comes first. The material's permittivity is an important parameter for the study of EM interaction with matter.

2.2.3 Lorentz-Drude Model

The Lorentz model and the Drude model are theoretical models used to examine the optical and electrical characteristics of metals. These models were created independently and then combined to generate the Lorentz-Drude model, which offers a more detailed account of electron behavior in metals. Metals are considered classical electron gas in the Drude model with electrons freely moving in a lattice of positive ions. The velocity of electrons is thought to be random, similar to that of a gas of classical particles. The model proposes that electrons collide with the lattice ions, causing scattering and eventual resistance. It also includes the idea of drift velocity, in which electrons gain an average velocity due to the applied electric field. The Drude model gives a fundamental knowledge of electrical conduction but has shortcomings when it comes to defining metal optical characteristics. The Lorentz

model accounts for electron harmonic oscillations in response to an electromagnetic field of light. The Lorentz model is very useful for understanding how electrons interact with incident electromagnetic radiation, which is necessary for describing phenomena such as dispersion and metal refractive index (RI). The Lorentz-Drude model is more comprehensive and adaptable, explaining a wide range of phenomena such as electrical conduction, optical characteristics, and the frequency-dependent behaviour of electrons in metals. H. Lorentz attempted to use the Maxwell Equation to describe light-matter interaction. His research concluded by defining a frequency dependent function for material permittivity using a series of differential equations and a harmonic oscillator framework for the electron-nucleus system. An angular frequency and a wave vector are linked with the dielectric function. The Drude model is based on metal electric conductivity. According to the Drude model, metal is made up of a collection of positively charged ions from which a few electrons are detached. In this model, metals specifically are considered free in the lattice formed by arranged ions. As a result, electrons can easily move in the presence of an external field [19]. The first approach in this context is to exemplify the free electron in metal as an electron gas that can freely move within the metal. Electrons were explained as being coupled to a simple spring-like restoring force in the original Lorentz model, which helped explain their oscillatory motion in response to an applied electric field. The Lorentz-Drude model, on the other hand, eliminates the restoring force component and instead concentrates on the mobility of free electrons in the presence of applied fields, accounting for scattering by lattice ions. The optical properties of metals can be understood using the plasma model, which describes the behavior of free electrons moving within a fixed lattice of positive ion cores. This model captures the essential dynamics of the "electron sea" as it responds to external stimuli, such as an applied electric field E. To analyze this response, a simple equation of motion for an individual electron in the plasma is formulated. However, a more comprehensive understanding requires incorporating the Lorentz-Drude model, which accounts for both free-electron behavior (Drude model) and bound-electron resonances (Lorentz model). The plasma frequency (ω_p) is a critical parameter that can determine the optical characteristics of the metal, may be computed by mathematically modeling the

interaction of light with the material. For instance, refer to Fig. 2.1, which illustrates a metallic slab with a breadth (L) and a cross-sectional area (A). This slab has N free electrons per unit volume.

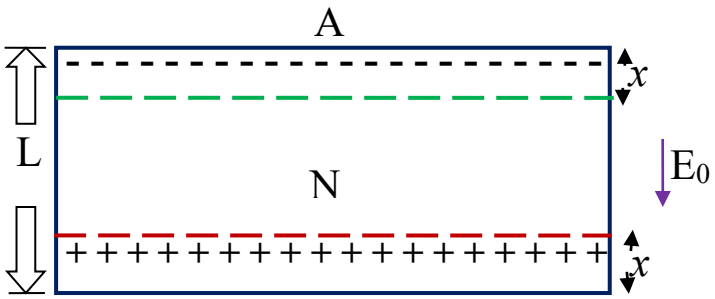

Fig. 2.1 Oscillations of conduction electrons in metal under the influence of a static electric field E_0

When the framework is initially subjected to a static electric field of strength E_0, electrons are drawn upward, leaving a positive charge region at the bottom. It will be interesting to investigate how the charge distribution changes when the static field is abruptly deactivated at time t = 0. Let x denote the displacement of the electron distribution from its equilibrium position. Therefore, the total electric charge present in the slab's top region can then be calculated as:

$$Q = -Ne \tag{2.1}$$

Where e is the charge of a single electron. Similarly, then total charge in the region at the bottom of the slab is given by,

$$Q = Ne \tag{2.2}$$

As shown by the diagram, for the small displacements (x << L), the surface charge densities on the top and bottom regions are:

$$\sigma_{bottom} = -\sigma_{top} = \sigma = Nex \tag{2.3}$$

Using Gauss`s Law, each plate contains electric field of $\sigma/2\varepsilon_0$. Therefore, the total electric field within framework is:

$$E_{tot} = \frac{\sigma}{\varepsilon_0} = \frac{Nex}{\varepsilon_0} \tag{2.4}$$

The electron cluster with effective optical mass *m* of each electron at the upper part of the stab, moves freely and can be subjected to Newton's second law with collisions from occurring with force F. This leads to the force equation,

$$F = QE_{tot} = Nm\ddot{x} \tag{2.5}$$

$$\therefore (-Ne)\left(\frac{Nex}{\varepsilon_0}\right) = Nm\ddot{x}$$

$$\ddot{x} = \frac{-Ne^2x}{m\varepsilon_0} \tag{2.6}$$

The solution for above second order differential equation leads to,

$$x(t) = x_0 e^{-\omega_p t} + C \tag{2.7}$$

Where,

$$\omega_p = \sqrt{\frac{Ne^2x}{m\varepsilon_0}} \tag{2.8}$$

Here, ω_p is referred to as plasmonic frequency, which represents the characteristic frequency of oscillation for a collective assembly of free electrons. This value is a fundamental parameter in the study of plasma and plasmonic phenomena, describing the natural resonant oscillations of the system.

To extend this analysis, we consider the interaction of a free electron with an external light source. In this case, the electric field of the incident light can be expressed as:

$$\tilde{E}(t) = E_0 e^{-i\omega t} + C \tag{2.9}$$

This expression describes the oscillating electric field of the light wave. Here, is E_0 the amplitude of the electric field, and ω is the angular frequency of the light. The constant *C* represents any additional static component of the field, which can vary depending on the system setup. Due to damping, the electric field will have an impact on the force acting on the electron. Therefore, the force acting on the electron with the damping factor γ will have the equation,

$$\tilde{F}(t) = m\ddot{\tilde{x}} = -e\tilde{E}(t) - 2m\gamma\dot{\tilde{x}} \tag{2.10}$$

$$\ddot{\tilde{x}} + 2\gamma\dot{\tilde{x}} = \frac{-e\tilde{E}(t)}{m}$$

This leads to solution.

$$\tilde{x}(t) = x_0 e^{-i\omega t} + C \tag{2.11}$$

$$x_0 = \frac{-e E_0 / m}{\omega^2 + 2i\omega\gamma}$$

By calculating susceptibility, we are effectively analyzing how a material's electron density reacts to varying frequencies of incident light. To find susceptibility, the polarization will be $\vec{P}(\omega) = -eNx_0$ equal to the linear susceptibility through the relation $\vec{P} = \varepsilon_0 \chi(\omega) E_0$

$$\vec{P} = -eNx_0 = \varepsilon_0 \chi(\omega) E_0 \tag{2.12}$$

$$\therefore \varepsilon_0 \chi(\omega) E_0 = \frac{-e^2 NE / m}{\omega^2 + 2i\omega\gamma}$$

This leads to susceptibility equation, using 2.8,

$$\chi(\omega) = \frac{-e^2 NE_0 / \varepsilon_0 m}{\omega^2 + 2i\omega\gamma} = \frac{-\omega_p^2}{\omega^2 + 2i\omega\gamma} \tag{2.13}$$

The damping term $(2i\omega\gamma)$ in the denominator ensures that the system accounts for energy dissipation, which is essential in materials where loss mechanisms are present, such as in metals and semiconductors. Further, relative complex permittivity $\varepsilon(\omega)$ is defined by the Lorentz-Drude Model as [20] :

$$\varepsilon(\omega) = \varepsilon_r(\omega) + i\varepsilon_i(\omega) \tag{2.14}$$

The relative complex permittivity can also be expressed by electric susceptibility as,

$$\varepsilon(\omega) = 1 + \chi(\omega) \tag{2.15}$$

For metals, the equation can be reduced. Since metals have no bound electrons, the model does not include a restoring spring force, leading to $\omega_0 = 0$. Using Equations (2.13) and (2.15), the Lorentz-Drude Model for metals will be reduced [21]:

$$\varepsilon(\omega) = 1 - \frac{\omega_p^2}{(\omega^2 + 2i\omega\gamma)} \tag{2.16}$$

$$\varepsilon(\omega) = 1 - \frac{\omega_p^2(\omega^2 - 2i\omega\gamma)}{(\omega^2 + 2i\omega\gamma)(\omega^2 - 2i\omega\gamma)}$$

$$\varepsilon(\omega) = 1 - \frac{\omega_p^2 \omega^2}{(\omega^2 - 2i\omega\gamma)^2} - i\frac{2\omega_p^2 \omega\gamma}{(\omega^2 - 2i\omega\gamma)^2}$$

$$\varepsilon_r(\omega) = 1 - \frac{\omega_p^2 \omega^2}{(\omega^2 - 2i\omega\gamma)^2}$$

$$\therefore \varepsilon_r(\omega) = 1 - \frac{\omega_p^2}{(\omega^2 + 4\gamma^2)} \tag{2.17}$$

$$\Rightarrow \varepsilon_i(\omega) = \frac{\omega_p^2 (2\omega\gamma)}{(\omega^2 - 2i\omega\gamma)^2}$$

$$\therefore \varepsilon_i(\omega) = \frac{2\omega_p^2 \gamma}{\omega(\omega^2 + 4\gamma^2)} \tag{2.18}$$

For small damping case, i.e., for conduction electron in metal $\gamma = 0$,

$$\varepsilon_r(\omega) = 1 - \frac{\omega_p^2}{\omega^2} \tag{2.19}$$

The dispersion relation for free electron gas is given by:

$$k = \frac{n\,\omega}{c}$$

$$\therefore k^2 = \frac{n^2\omega^2}{c^2} = \frac{\varepsilon(\omega)\omega^2}{c^2}$$

using 2.19,

$$k^2 c^2 = \left(1 - \frac{\omega_p^2}{\omega^2}\right)\omega^2$$

$$\therefore k^2 c^2 = \omega^2 - \omega_p^2 \tag{2.20}$$

This illustrates that the propagation constant k can take a real value, enabling the wave to propagate with condition $\omega > \omega_p$. To confine the study, consider the following:

1. For $\omega > \omega_p$, $\varepsilon_r(\omega)$ become a positive real number. Consequently, there is zero absorption and the metal displays transparency to electromagnetic radiation.

2. For $\omega < \omega_p$, $\varepsilon_r(\omega)$ value becomes negative for metal. This means metal retains their metallic character. When an electromagnetic wave strikes on such a material from a dielectric, it is entirely reflected.

But for some noble metals show absorption with $\omega < \omega_p$, such as gold (Au), silver (Ag), copper (Cu) metals [22].

2.3 Electromagnetic Theory of SPR

To comprehend the phenomenon of SPR, one must first recognize the fundamental characteristics of SPP. To achieve the foregoing goal, study starts from the core concept of electromagnetic wave equation.

2.3.1 Wave Equation

Maxwell Equation of electromagnetism at macroscopic level are as follows [21]:

$$\vec{\nabla}.\vec{D} = \rho_{ext} \tag{2.21a}$$

$$\vec{\nabla}.\vec{B} = 0 \tag{2.21b}$$

$$\vec{\nabla} \times \vec{E} = -\frac{\partial \vec{B}}{\partial t} \tag{2.21c}$$

$$\vec{\nabla} \times \vec{H} = \bar{J}_{ext} + \frac{\partial \vec{D}}{\partial t} \tag{2.21d}$$

When there are no external charges or currents, the Maxwell Eqs. 2.21c and 2.21d can combine to obtain. As $\rho_{ext} = \vec{J}_{ext} = 0$,

$$\vec{\nabla} \times \vec{\nabla} \times \vec{E} = -\mu_0 \frac{\partial^2 \vec{D}}{\partial t^2} \tag{2.22}$$

$$\vec{\nabla} \times \vec{\nabla} \times \vec{E} = \vec{\nabla}\left(\vec{\nabla}.\vec{E}\right) - \vec{\nabla}^2 \vec{E} \tag{2.23}$$

$$\vec{\nabla}.\left(\varepsilon \vec{E}\right) = \vec{E}\left(\vec{\nabla}\varepsilon\right) + \varepsilon\left(\vec{\nabla}.\vec{E}\right)$$

as $$\vec{\nabla}.\vec{D} = \rho_{ext} = 0$$

$$\vec{D} = \varepsilon_0 \varepsilon \vec{E}$$

$$\therefore \frac{\vec{\nabla}.\vec{D}}{\varepsilon_0} = 0 = \vec{E}\left(\vec{\nabla}\varepsilon\right) + \varepsilon\left(\vec{\nabla}.\vec{E}\right)$$

$$\Rightarrow \vec{\nabla}.\vec{E} = -\frac{1}{\varepsilon}\vec{E}\left(\vec{\nabla}\varepsilon\right)$$

Substituting in Eq. 2.26

$$\vec{\nabla}\left(\vec{\nabla}.\vec{E}\right) - \vec{\nabla}^2\vec{E} = -\mu_0\varepsilon_0\varepsilon\frac{\partial^2\vec{E}}{\partial t^2}$$

$$\vec{\nabla}\left(-\frac{1}{\varepsilon}\vec{E}\left(\vec{\nabla}\varepsilon\right)\right) - \vec{\nabla}^2\vec{E} = -\mu_0\varepsilon_0\varepsilon\frac{\partial^2\vec{E}}{\partial t^2} \tag{2.24}$$

For a dielectric profile that changes very little over distance in the order of one optical wavelength, which means $\vec{\nabla}.\varepsilon = 0$, Eq. 2.24 further reduced to

$$\vec{\nabla}^2\vec{E} = \mu_0\varepsilon_0\varepsilon\frac{\partial^2\vec{E}}{\partial t^2} \tag{2.25}$$

$$\varepsilon_0\mu_0 = \frac{1}{c^2} \tag{2.26}$$

$$\vec{\nabla}^2\vec{E} - \frac{\varepsilon}{c^2}\frac{\partial^2\vec{E}}{\partial t^2} = 0 \tag{2.27}$$

Equation 2.27 is Electromagnetic wave equation. This equation must be solved using regions of constant ε, and the solution should match using the appropriate boundary conditions. There are two ways to understand the property of the propagating wave using Eq. 2.27 first, assume a harmonic time dependence of electric field, and second, through propagation geometry.

Assuming electric field is $\vec{E}(\hat{r},t) = \vec{E}(\hat{r})e^{i\omega t}$, Eq. 2.27 gives,

$$\vec{\nabla}^2\vec{E}(\hat{r})e^{i\omega t} - \frac{\varepsilon}{c^2}\frac{\partial^2\vec{E}(\hat{r})e^{i\omega t}}{\partial t^2} = 0$$

$$\vec{\nabla}^2\vec{E}(\hat{r})e^{i\omega t} - \frac{\varepsilon}{c^2}(i\omega)^2\frac{\partial^2\vec{E}(\hat{r})e^{i\omega t}}{\partial t^2} = 0$$

$$\vec{\nabla}^2\vec{E} + k_0^2\varepsilon\frac{\partial^2\vec{E}}{\partial t^2} = 0 \tag{2.28}$$

Here, $k_0 = \frac{\omega}{c}$ is the electromagnetic wave's propagation wave vector in vacuum. The wave equation in Eq. 2.28 is usually known as the Helmholtz equation.

Maxwell`s curl equation such as $\vec{\nabla} \times \vec{E}$ and $\vec{\nabla} \times \vec{H}$ in vacuum can be used to find the explicit for field component of electric field and axillary field to investigate the dispersion of propagating wave in above.

With $\frac{\partial}{\partial x} = i\beta$ for wave propagate in *x*-direction, $\frac{\partial}{\partial t} = -i\omega$ due to harmonic time dependence, and $\frac{\partial}{\partial y} = 0$ because homogeneity in y-direction. For wave, propagation in *x*-direction, the harmonic time dependence, and homogeneity in y-direction, Maxwell equations of curls in vacuum gives:

$$\frac{\partial E_y}{\partial z} = -i\omega\mu_0 H_x \tag{2.29}$$

$$\frac{\partial E_x}{\partial z} - i\beta E_z = -i\omega\mu_0 H_y \tag{2.30}$$

$$i\beta E_y = i\omega\mu_0 H_z \tag{2.31}$$

$$\frac{\partial H_y}{\partial z} = i\omega\varepsilon_0 \varepsilon E_x \tag{2.32}$$

$$\frac{\partial H_x}{\partial z} - i\beta H_z = -i\omega\varepsilon_0 \varepsilon E_y \tag{2.33}$$

$$i\beta H_y = -i\omega\varepsilon_0 \varepsilon E_z \tag{2.34}$$

For waves propagating, these equations produce two distinct sets of self-sustaining solutions with varying polarization properties. First, propagating wave with polarization caused by a magnetic field perpendicular to the incidence plane, commonly referred to as the Transverse Magnetic (TM) or p-mode, with the field components E_x, E_z and H_y are nonzero. Second, polarization of propagating wave with electric field perpendicular to the plane of incidence, referred to as the Transfer Electric (TE) or s-mode, with the field component H_x , H_z and E_y are nonzero.

For TM mode (p- polarized) wave:

$$E_y = H_x = H_z = 0$$

Therefore, Eq. 2.32 yields,

$$\frac{\partial H_y}{\partial z} = i\omega\varepsilon_0\varepsilon E_x$$

$$\Rightarrow E_x = -\frac{1}{\omega\varepsilon_0\varepsilon}\frac{\partial H_y}{\partial z} \tag{2.35}$$

From Eq. 2.34**,**

$$E_z = -\frac{\beta}{\omega\varepsilon_0\varepsilon}H_y \tag{2.36}$$

Wave equation for TM mode as:

$$\frac{\partial H_y}{\partial z} = i\omega\varepsilon_0\varepsilon E_x$$

Taking partial derivative of above equation with respect to z

$$\frac{\partial^2 H_y}{\partial z^2} = i\omega\varepsilon_0\varepsilon\frac{\partial E_x}{\partial z}$$

From Eqs. 2.35 and 2.36,

$$\frac{\partial E_x}{\partial z} = i\beta E_z + i\omega\mu_0 H_y$$

$$E_z = -\frac{\beta}{\omega\varepsilon_0\varepsilon}H_y$$

$k_0 = \frac{\omega}{c}$,

$$\therefore \frac{\partial^2 H_y}{\partial z^2} = i\omega\varepsilon_0\varepsilon\left(-\frac{i\beta^2}{\omega\varepsilon_0\varepsilon}H_y + i\omega\mu_0 H_y\right)$$

as $k_0^2 = \varepsilon_0\mu_0\omega,^2 \rightarrow \frac{\partial^2 H_y}{\partial z^2} + \left(k_0^2\varepsilon - \beta^2\right)H_y = 0$ (2.37)

For TE mode (s- polarized) wave

$$H_y = E_x = E_z = 0$$

Therefore Eq. 2.29 yields,

$$H_x = i\frac{1}{\omega\mu_0}\frac{\partial E_y}{\partial z} \tag{2.38}$$

From Eq. 2.31,

$$H_z = \frac{\beta}{\omega\mu_0}E_y \tag{2.39}$$

Wave equation for TE mode as:

$$\frac{\partial^2 E_y}{\partial z^2} + (k_0^2\varepsilon - \beta^2)E_y = 0 \tag{2.40}$$

2.3.2 Metal-Dielectric Interface

Let's understand the simplest geometry with one interface between non-absorbing dielectric $(+\varepsilon_2)$ and metallic layer $(\varepsilon_1(\omega))$, as shown in Fig. 2.2. For surface waves to exist at this metal-dielectric interface, the real part of $\varepsilon_1(\omega)$ must be negative $(\varepsilon_1(\omega)_{real} < 0)$ and its magnitude must be $(\varepsilon_1(\omega)_{real} < \varepsilon_2)$. These conditions ensure that the surface waves can propagate along the interface, with their electromagnetic fields decaying exponentially away from the surface.

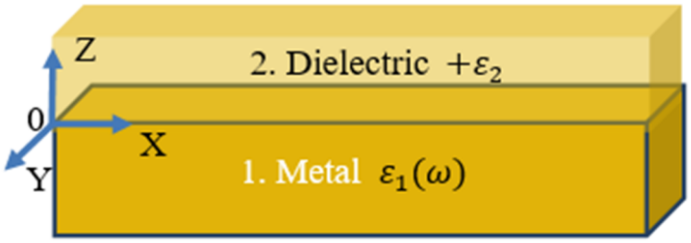

Fig. 2.2 Schematic of Metal-Dielectric Interface

Consider a wave propagating in the x-direction whose solution is confined to the Metal-dielectric interface.

a) Begin with the TM wave solution of the wave equation from Eq. 2.37. As per geometry, there are two regions; one with $z > 0$ and other is $z < 0$.

1. For $z > 0$,

Let $$H_{2y}(z) = A_2 e^{i\beta x} e^{-k_2 z} \tag{2.41}$$

From Eq. 2.35,

$$E_{2x}(z) = \frac{1}{i\omega\varepsilon_0\varepsilon_2}\frac{\partial}{\partial z} A_2 e^{i\beta x} e^{-k_2 z}$$

$$\therefore E_{2x}(z) = \frac{ik_2}{\omega\varepsilon_0\varepsilon_2} A_2 e^{i\beta x} e^{-k_2 z} \tag{2.42}$$

From Eq. 2.36,

$$E_{2z}(z) = -\frac{\beta}{\omega\varepsilon_0\varepsilon_2} A_2 e^{i\beta x} e^{-k_2 z}$$

2. For $z < 0$,

Let $$H_{1y}(z) = A_1 e^{i\beta x} e^{-k_1 z} \tag{2.43}$$

From Eq. 2.35,

$$E_{1x}(z) = -\frac{1}{i\omega\varepsilon_0\varepsilon_1}\frac{\partial}{\partial z} A_1 e^{i\beta x} e^{-k_1 z} \tag{2.44}$$

$$\therefore E_{1x}(z) = -\frac{ik_1}{\omega\varepsilon_0\varepsilon_1} A_1 e^{i\beta x} e^{-k_1 z}$$

From Eq. 2.36,

$$E_{1y}(z) = -\frac{\beta}{\omega\varepsilon_0\varepsilon_1} A_1 e^{i\beta x} e^{-k_1 z} \tag{2.45}$$

With the constraint that evanescent electric field (EF) decays in z-direction perpendicular to the propagation direction.

$$k_1 = k_2 = k_z = \text{Wave vector} \tag{2.46}$$

$$\hat{k} = \frac{1}{|k_z|} = \text{EF decay length} \tag{2.47}$$

At the interface, boundary condition requires the electric field to be continuous, and the magnetic field to be parallel to the interface. Therefore,

$$H_{1y} = H_{2y}; E_{1z} = E_{2z} \text{ and } \varepsilon_1 E_{1z} = \varepsilon_2 E_{2z} \tag{2.48}$$

To satisfy above boundary conditions, constrains require are $A_1 = A_2$, and $\frac{k_2}{k_1} = -\frac{\varepsilon_2}{\varepsilon_1}$. At the interface, for the surface wave to be excited, the surface demands the following conditions.

1. ε_{1real} of metal must be –ve
2. $|\varepsilon_{1real}| > |\varepsilon_{2real}|$

Further, the solution of H_{1y} and H_{2y} must satisfy the wave Eq. of 2.37,

$$\therefore \frac{\partial^2 H_{1y}}{\partial z^2} + (k_0^2 \varepsilon_1 - \beta^2) H_{1y} = 0$$

using Eq. 2.43,

$$\frac{\partial^2 A_1 e^{i\beta x} e^{-k_1 z}}{\partial z^2} + (k_0^2 \varepsilon_1 - \beta^2) A_1 e^{i\beta x} e^{-k_1 z} = 0$$

$$k_1^2 A_1 e^{i\beta x} e^{-k_1 z} = -(k_0^2 \varepsilon_1 - \beta^2) A_1 e^{i\beta x} e^{-k_1 z}$$

$$\Rightarrow k_1^2 = \beta^2 - k_0^2 \varepsilon_1 \tag{2.49}$$

similarly,

$$\frac{\partial^2 H_{2y}}{\partial z^2} + (k_0^2 \varepsilon_2 - \beta^2) H_{2y} = 0$$

using Eq. 2.43,

$$\frac{\partial^2 A_2 e^{i\beta x} e^{-k_2 z}}{\partial z^2} + (k_0^2 \varepsilon_2 - \beta^2) A_2 e^{i\beta x} e^{-k_2 z} = 0$$

$$\Rightarrow k_2^2 = \beta^2 - k_0^2 \varepsilon_2 \tag{2.50}$$

From boundary conditions, we know that

$$k_1 = -\frac{\varepsilon_1}{\varepsilon_2} k_2 \Rightarrow k_1^2 = \frac{\varepsilon_1^{\,2}}{\varepsilon_2^{\,2}} k_2^2$$

using Eqs. 2.49 and 2.50,

$$\beta^2 - k_0^2 \varepsilon_1 = \frac{\varepsilon_1^{\,2}}{\varepsilon_2^{\,2}} \left(\beta^2 - k_0^2 \varepsilon_2\right)$$

$$\beta^2 \left(\frac{\varepsilon_1^{\,2}}{\varepsilon_2^{\,2}} + 1\right) = k_0^2 \varepsilon_1 \left(\frac{\varepsilon_1}{\varepsilon_2} - 1\right)$$

$$\beta^2 \left(\frac{\varepsilon_1}{\varepsilon_2} + 1\right)\left(\frac{\varepsilon_1}{\varepsilon_2} - 1\right) = k_0^2 \varepsilon_1 \left(\frac{\varepsilon_1}{\varepsilon_2} - 1\right)$$

$$\beta^2 \left(\frac{\varepsilon_1}{\varepsilon_2} + 1\right) = k_0^2 \varepsilon_1$$

$$\beta = k_0 \sqrt{\frac{\varepsilon_1 \varepsilon_2}{\varepsilon_1 + \varepsilon_2}} \tag{2.51}$$

At resonance, as $k_0 = \frac{\omega}{c}$,

$$\beta = k_{spp} = \frac{\omega}{c} \sqrt{\frac{\varepsilon_1 \varepsilon_2}{\varepsilon_1 + \varepsilon_2}} \tag{2.52}$$

b) TE wave solution of the wave equation from Eq. 2.40. As per geometry, there are two regions; one with $z > 0$ and other is $z < 0$

1. For $z > 0$,

   Let $$E_{2y}(z) = A_2 e^{i\beta x} e^{-k_2 z} \tag{2.53}$$

   using Eqs. 2.38 and 2.39,

   $$H_{2x}(z) = \frac{-iA_2 k_2}{\omega \mu_0} A_2 e^{i\beta x} e^{-k_2 z} \tag{2.54}$$

   $$H_{2z}(z) = \frac{\beta}{\omega \mu_0} A_2 e^{i\beta x} e^{-k_2 z} \tag{2.55}$$

2. For $z < 0$

   Let $$E_{1y}(z) = A_1 e^{i\beta x} e^{k_1 z} \tag{2.56}$$

using Eqs. 2.38 and 2.39,

$$H_{1x}(z) = \frac{ik_1}{\omega\mu_0} A_1 e^{i\beta x} e^{k_1 z} \tag{2.57}$$

$$H_{1z}(z) = \frac{\beta}{\omega\mu_0} A_1 e^{i\beta x} e^{k_1 z} \tag{2.58}$$

As per the boundary conditions, maintaining continuity at the interface for both the electric and magnetic fields results in the following:

$$E_{1y}(z) = E_{2y}(z)$$

$$A_1 e^{i\beta x} e^{k_1 z} = A_2 e^{i\beta x} e^{-k_2 z}$$

$$\Rightarrow A_1 = A_2 \tag{2.59}$$

and

$$H_{1x}(z) = H_{2x}(z)$$

$$\frac{iA_1 k_1}{\omega\mu_0} e^{i\beta x} e^{k_1 z} = \frac{-iA_2 k_2}{\omega\mu_0} e^{i\beta x} e^{-k_2 z}$$

$$\therefore A_1 k_1 = -A_2 k_2$$

using Eq. 2.59,

$$A_1 k_1 = -A_1 k_2$$

$$\Rightarrow A_1 (k_1 + k_2) = 0$$

$$(k_1 + k_2) = 0 \quad \text{or} \quad A_1 = 0$$

The surface requires $k_1 > 0$ and $k_2 > 0$. We can only draw one remark from this.

$$A_1 = A_2 = 0 \tag{2.60}$$

This reveals that the amplitude of the electric field is zero. This leads us to believe that no surface wave at the interface exists for TE polarization.

The investigation of electromagnetic wave propagation for both TE and TM modes reveals that, for the TE mode, surface waves do not exist at the interface. The

propagation constant of the surface wave for the TM wave mode is derived in equation (2.52).

$$\beta = k_{spp} = \frac{\omega}{c}\sqrt{\frac{\varepsilon_1 \varepsilon_2}{\varepsilon_1 + \varepsilon_2}}$$

Equation (2.52) represents the propagation of surface waves, subject to two important conditions.

1. The metal and dielectric permittivities should have opposite signs.
2. Magnitude metal permittivity should be less than magnitude dielectric permittivity.

This equation highlights the dependence of the SPP wave vector on the dielectric properties of the materials at the interface. At resonance, the SPP wave vector exhibits a strong coupling between the electromagnetic field and the collective oscillations of free electrons in the metal, leading to a plasmonic resonance. In the visible and near-infrared spectral range, metals like Au, Ag, and aluminum (Al) exhibit a real part of permittivity that is negatively valued. Incorporating a non-zero imaginary component into the metal's permittivity makes it more likely that the above mode will exist at the metal-dielectric interface. This mode is referred to as evanescent modes and is also known as surface plasmons (SP).

2.3.3 Dispersion relation

Light wave and SPW dispersion curves must be studied to figure out the pivotal points to excite SPP [23].The light wave obeys the dispersion relation $\omega = ck$, as shown in Fig. 2.3 by the straight-line (b). When the frequencies exceed plasmonic frequency ω_{pb}, radiative plasmonic mode is shown by the curve of (a) in Fig. 2.3. While the curve (d) depicted the nature of SPP. As observed at frequency ω_0, light's wave vector is smaller in a dielectric medium than that required to excite SPP. Therefore, it is not possible to stimulate SPP by merely pointing a light wave at a metal-dielectric contact. This means that the incident light wave vector needs to increase in order to meet the required SPP's wave vector. This can be achieved through coupling techniques.

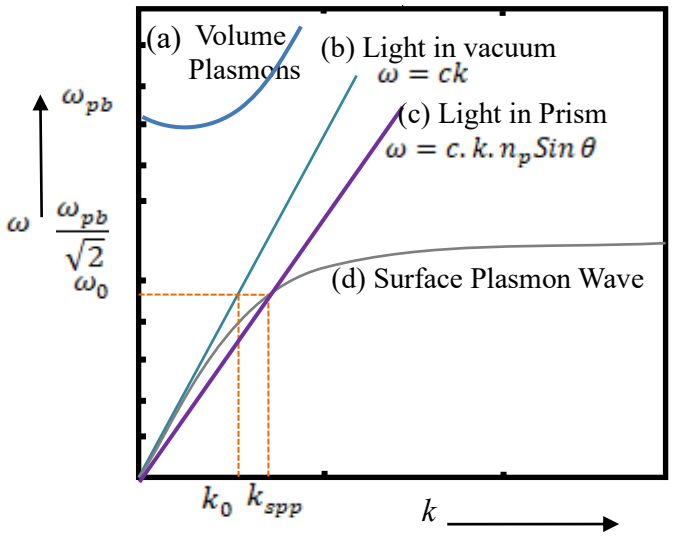

Fig. 2.3 Dispersion Curves for (a)Volume plasmons(blue colour), (b)Light in Vacuum (sky blue colour), (c) Light in Prism (purple colour), and (d) SPW(gray colour)

2.3.4 Excitation of SPP

There are different coupling techniques available like prism coupling, grating coupling etc. Let us look at one of the most effective techniques, prism coupling [24]. As previously stated, incident light cannot be excited SPP on a metal-dielectric interface due to the mismatch in wave vectors with the incoming light. The incident wave follows the relation $k = \frac{\omega}{c}$, can be increased through the projection along the metal-dielectric interface, as shown in Fig. 2.4. This phenomenon, known as phase matching [25,26].

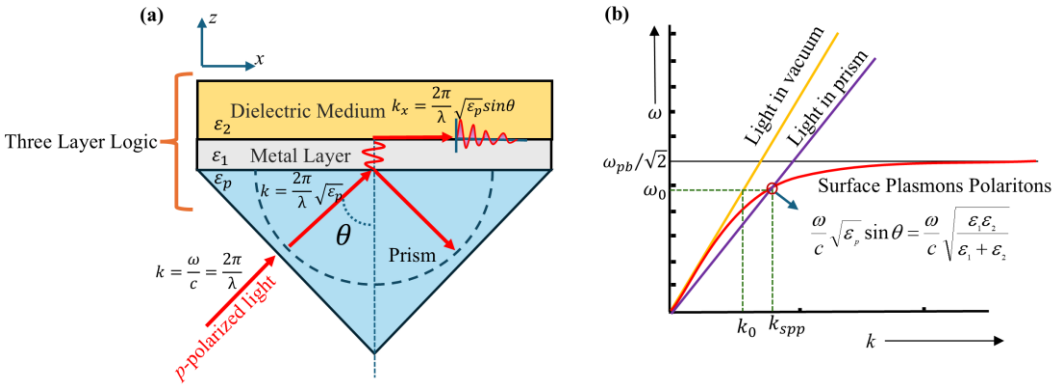

Fig. 2.4 (a) Basic SPR configuration with wave vectors in each medium (b) Dispersion graphs for bulk plasmon (blue colour), light in free space (yellow colour), light in glass prism medium (violet colour) and surface plasmon (orange colour).

However, it's important to note that k_x is still smaller than the propagation constant of SPP k_{SPP}. The use of a prism can increase the wave vector of incident wave further by $n_p = \sqrt{\varepsilon_p}$. This increases the possibility of SPP excitation at metal-dielectric interface with help of third medium prism at critical incident angle.

$$\therefore \frac{\omega}{c} n_p \sin\theta = \frac{2\pi}{\lambda}\sqrt{\varepsilon_p}\sin\theta = k_x \tag{2.61}$$

Where θ is angle of incident photon to the surface normal, and λ is wavelength of the incident light. At critical incident angle, tuning the wave vector of the incident light k_x to meet the requirements for exciting SPs establishes a Resonance condition.

$$\frac{2\pi}{\lambda}\sqrt{\varepsilon_p}\sin\theta = \frac{\omega}{c}\sqrt{\frac{\varepsilon_1\varepsilon_2}{\varepsilon_1+\varepsilon_2}} \tag{2.62}$$

This critical angle is commonly referred to as an SPR angle. There are two possible prism coupling geometries for SPR device structure: one involves a dielectric layer sandwiched between the prism and metal, while the other features a metal layer sandwiched between the prism and dielectric. This leads to two configurations in SPR, namely the Otto configuration and the Kretschmann and Raether configuration. In Otto's configuration, light passes through a high RI prism toward the dielectric-metal interface with a thin dielectric layer and a semi-infinite metal layer, as shown in Fig. 2.5(a) [27]. When incident light enters the prism and undergoes total internal reflection at the prism-dielectric interface, it results in the phenomenon of attenuated total reflection (ATR). ATR is a key mechanism that can be utilized for coupling of SP on the metal layer. However, despite its theoretical advantages, the Otto configuration faces practical limitations due to the challenges of maintaining the precise thickness of the dielectric layer required for effective SP excitation. As a practical aspect, this configuration is not a viable method for SP excitation due to the issue of maintaining proper and careful thickness of the dielectric layer between the prism and metal. These challenges emphasize the need for alternative geometries, such as the Kretschmann and Raether configuration, which overcome these limitations and are more commonly employed in SPR applications.

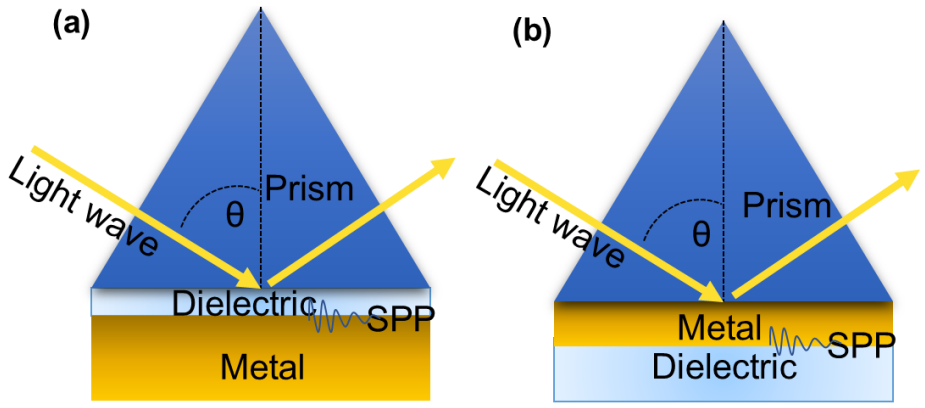

Fig. 2.5 (a) Otto's configuration; (b) Kretschmann and Raether configuration

In the Kretschmann and Raether configuration, the prism base is coated with a thin metal layer before interfacing with the semi-infinite dielectric layer, as shown in Fig. 2.5(b) [28]. When an incident light wave traverses the prism and encounters the metal layer, a portion of the incident light is reflected back into the prism, while the remaining portion enters the metal as an inhomogeneous EM. In total internal reflection, almost all light waves reflect at a critical incident angle. But in this condition if relative amount of incident photons escape and extend to a few micrometers beyond the surface of metal in the form of a wave, known as evanescent wave (EW). ATR uses the phenomenon of total internal reflection to generate EF [29]. Due to photons absorption, intensity of reflect wave decreases and reaches minimum at critical angle of incident, as shown in Fig. 2.6.

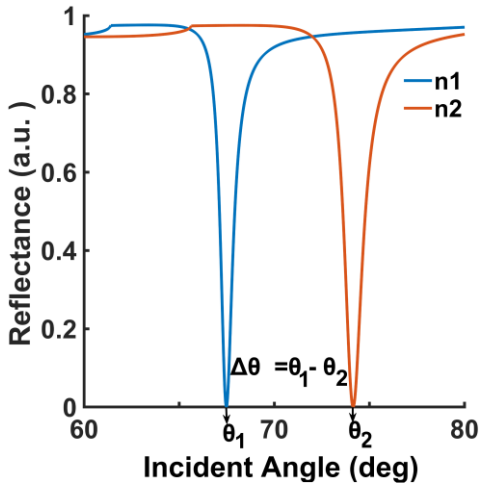

Fig 2.6 Reflectance Curve of SPR before interaction (in blue colour) and after interaction (in orange colour) at the interface

All absorbed energy is used to generate EWs. Prior to the interaction, the SPR produced at angle θ_1, due to the sensing medium having refractive index n_1. However, upon interaction taking place within sensing medium, refractive index of sensing medium changes to new value, denoted as n_2, leading to the production of SPR at a new critical angle, θ_2. The measurable quantity, $\Delta\theta=\theta_1-\theta_2$, represents the angular shift and is employed as a key parameter for utilizing SPR as a biosensor.

2.4 Literature Review

The literature review offers an in-depth overview of the attributes and scientific background of the material under study. Studying new materials in SPR is crucial to make prism based SPR sensors work better. As per the reviews work presented by Homola et al. 2008, Yesudasu et al.2021, and Divya et al. 2022 the choice of materials significantly influences the interaction between the sensing surface and target analytes, influencing the detection limits and accuracy of the biosensor [30–32]. The SPR phenomenon occurs when the incoming light wavelength matches the natural frequency of surface plasmons. Therefore, the choice of wavelength is intimately related to the material utilized in construction of SPR sensors. Notably, the simplicity and accessibility of He-Ne lasers of wavelength 632.8 nm make it a feasible choice for many SPR studies. Furthermore, the examination of material can modify the SPR characteristics to specific applications by exploring and incorporating innovative materials.

2.4.1 Different prism

According to section 2.3.2, the wave vector required to excite SPPs at the metal-dielectric interface is greater than the incident light wave vector. The incorporation of high refractive index materials, such as glass, facilitates the necessary phase matching for SPPs. It realized that the glass prism`s refractive index has a significant impact on the performance of SPR sensors. Higher refractive index glasses yield increased resolution but lower sensitivity, while lower refractive index materials offer higher sensitivity at the expense of resolution [33]. Notably, various prisms, including BK7, SF5, SF10, SF11, and Sapphire, exhibit specific refractive

indices at a wavelength of 632.8nm 1.5151 + 0i, 1.6685 + 0i, 1.7231 + 0i, 1.7786 + 0i, and 1.7659 + 0i with unit of refractive index (RIU) respectively for each [34].

2.4.2 Different Metal

In SPR, the metal layer plays an important role, certain noble metals like gold (Au), silver (Ag), and copper (Cu) possessing unique optical properties that allow them to absorb incident photon energy [35]. The real part of the relative permittivity in metals signifies polarization strength under an external electric field, while the imaginary part explains absorption and scattering losses during material interaction with EMs. To successfully excite SPP, the relative permittivity of the metal must be real and negative, opposite to the real and positive relative permittivity of the dielectric. Notably, Ag, Au, and Cu exhibit relative permittivities of -18.281+0.48108i, -11.740+1.2611i, and -11.542+1.8405i, respectively, at wavelength 632.8nm, with dimensionless units. De Bruijn et. al. work shows a good review on the choice of metallic layer and wavelength for construction of SPR sensor, offering insights into the sensitivity of SPR sensors with different metals [36]. Among the listed combinations, Ag with a wavelength of nearly 800 nm emerges as the optimal choice, although it presents challenges such as oxidation. SPR sensors with Au offer greater sensitivity but less accuracy and low biomolecule adsorption [37]. This led to the investigation of Ag-Au bimetallic layers, which benefited from Ag's strong plasmonic properties in the visible spectrum as well as Au's plasmonic properties in the visible and near-infrared ranges. Noteworthy, the refractive indices of Ag, Au, and Cu at a wavelength of 632.8nm are as 0.056253 + 4.2760i (RIU), 0.18377 + 3.4313i (RIU) and 0.26965 + 3.4106i (RIU), respectively [38].

Considering prior findings [39], the inclusion of a high RI values of dielectric layer between the analyte and metal layers has been shown to enhance sensor sensitivity and stability. The dielectric layer, when coated over the metallic based prism before interacting with the sensing medium, significantly influences the functionality of SPR sensors. Performance parameters such as minimum reflection intensity (Rmin), change in resonance angle ($\Delta\theta$), and half width at half maximum (HWHM) are dependent on the refractive index (RI) of the dielectric material [40].For mid-IR applications, conventional semiconductors and 2D materials like graphene are

suitable, while metal-nitrides and Transparent Conductive Oxides (TCOs) enhance sensitivity in NIR and visible SPR devices [41].

2.4.3 Two Dimensional (2D) Materials

2D materials, such as graphene and Transition Metal Dichalcogenides (TMDCs), exhibit unique properties due to their atomically thin structure. These materials have shown enormous potential for use in various applications, including electronics, optoelectronics, and energy storage. Their high surface-to-volume ratio and exceptional mechanical, thermal, and electronic properties make them ideal candidates for next-generation technologies.

Graphene: Graphene is a two-dimensional carbon material with impressive electronic, mechanical, and thermal properties with a single atom thickness [42]. Absorption is a crucial parameter in optical sensors when light interacts with a material, and experimental findings note graphene's substantial absorption in the visible spectral range [43]. Recognized as a wonder substance of the 21st century, graphene's 2D properties offer a tunable plasma frequency in infrared and terahertz frequencies, along with easy interaction with bimolecular materials [44]. Its excellent carrier mobility and quantum Hall effect further expand its utility in advanced optoelectronic systems. Additionally, graphene's flexibility and robustness make it a promising candidate for wearable and stretchable sensor devices. In monolayer graphene, every carbon atom has direct interaction capabilities with the analyte, enabling the highest possible sensitivity in applications such as ultra capacitors, nanoelectronics, biomedical research, and industrial applications [45]. SPR with graphene can be used in biosensors because variations in graphene's chemical potential affect the concentration of charge carriers, which has a significant impact on its extinction coefficient and RI [46].

Transition-metal Dichalcogenide (TMDC): Transition-metal dichalcogenide (TMDC) are composed of transition metal elements and chalcogen elements. These materials have received substantial attention in biosensor research due to their unusual electrical and optical properties. Notable elements within the TMDC family include Tungsten disulfide (WS_2), Molybdenum disulfide (MoS_2), Molybdenum diselenide

($MoSe_2$), and Tungsten diselenide (WSe_2) [47]. One of the key aspects of interest in TMDCs is their ability to enhance the interaction between light and materials when used as a coating in various TMDCs improves sensitivity of SPR sensor [48].

To improve sensitivity, TMDCs are used often in SPR biosensors, and in some cases, in combination with silicon. The highest sensitivity achieved in these setups can reach 155.68°/RIU [49]. Additionally, literature shows that to increase the angular sensitivity and phase sensitivity, SPR biosensors used TMDCs/metal/TMDCs/graphene heterostructures layers [48]. Studying the bandgap of a material is essential for optical sensor applications as it determines the material's ability to absorb and emit light, influencing the sensor's sensitivity and operational range. In terms of bandgap, Graphene stands out with a unique property of zero, suggesting its semi metallic nature. On the other hand, WS_2 exhibits the highest bandgap at 1.98eV, followed by MoS_2 (1.82 eV), $MoSe_2$ (1.51 eV), and WSe_2 (1.62 eV) [50]. Regarding refractive indices, each material highlights distinct values. Graphene has a refractive index of 3 + 1.149i (RIU) [51], MoS_2 displays 4.9168 + 1.0554i (RIU), WS_2 exhibits 5.0646 + 0.23623i (RIU), $MoSe_2$ shows 5.2069 + 0.92551i (RIU), and WSe_2 features 5.2302 + 0.50229i (RIU) [52]. These variations highlight the materials' diverse optical properties, making them suitable for different applications in the realm of two-dimensional materials.

Comparing the 2D structure of TMDCs to graphene, several advantages become evident. Firstly, the 2D structure of TMDCs is more diverse than graphene, making them more adaptable for various biosensing and bioimaging applications through different mechanisms. For example, the tunable band gap of TMDCs allows for precise control over the absorption and emission wavelengths, enabling more accurate detection of specific biomolecules. Additionally, the presence of transition metal atoms in TMDCs provides additional functionalization sites for attaching biomolecules, enhancing their sensitivity and selectivity in biosensing applications. Moreover, TMDCs offer a larger and adjustable bandgap compared to graphene, which aids in preventing current leakage and provides greater sensitivity and reading accuracy. Another significant advantage is the structural stability of 2D TMDCs,

making them easy to prepare, process, and apply. Additionally, 2D TMDCs are cost-effective and offer a wider variety [53].

2.4.4 Semiconductors

Semiconductor role in SPR devices dates back to 2011. A prior study found that layering high refractive index silicon (Si) over gold can improve the sensitivity of the SPR sensor [4,54]. III-V nitrides or group wurtzite nitride nitrides have beneficial properties to implement as transducing components in biosensors. The Wurtzite nitride semiconductors family had members such as Gallium nitride (GaN), Aluminum nitride (AlN), and Indium nitride (InN). Three unique crystal structures are seen in III-V nitrides: zincblende, rock salt, and wurtzite. Wurtzite stands out among them due to its hexagonal unit cells, a non-centrosymmetric structure (with no center of inversion symmetry) that provides polarity to III-V nitrides. This polarity, which is a bulk feature, differs with the surface terminations feature that anions and cations can achieve. The interaction between polarity and surface termination has a significant impact on the biosensing-related features of wurtzite nitride nanomaterials. Due to its hexagonal unit cell structure, this material provides remarkable stability, and the unique capability to facilitate the direct growth of 2D materials on its surface [55].

The incorporation of such compound semiconductors in sensors may provide the opportunity to set the parameters in accordance with the sensing requirements. Their ability to engineer surface states offers fine-tuned sensor responsiveness and enhanced signal-to-noise ratios in detection processes. In addition, the compatibility of wurtzite nitrides with optical fibers and integrated photonic circuits paves the way for hybrid SPR sensor platforms. In terms of bandgap, Si has a bandgap of 1.12eV. AlN has the largest bandgap at 6.22 eV, followed by GaN (3.42 eV) and InN (0.64 eV) [56]. At 632.8 nm wavelength, Si has refractive index of 3.8827 + 0.019626i, while GaN's is 2.3848 + 0i; AlN and InN, on the other hand, show refractive indices of 2.1496 + 0i and 2.9 + 0i, having RIU as unit, respectively [57–60]. Recent advancements in fabrication techniques further enable precise layering and patterning of these semiconductors, which is critical for optimizing sensor performance. The impacts of varying configurations on SPR are explained in Table 2.1, providing

comprehensive insights into the optimized design parameters and corresponding performance details.

Table 2.1 Comparative Literature Survey of Device Structures

Year	wavelength (nm)	RI Detection Range (RIU)	Device structure	Sensitivity (°/RIU)	FOM (RIU^{-1})
2011 [61]	632.8	1.33-1.34	BAK3/Ag/Au	54.84	NG
2013 [62]	633	1.330-1.37	BK7/Ag/Graphene/Analyte	97.76	NG
2015 [63]	633	1.33-1.4	SF10/Chromium/Ag/Graphene/Affinity(RI=1.5265)	68.03	9.691
2016 [64]	633	1.33–1.335	BK7/Au/MoS_2/Au	182	NG
2016 [49]	600	1.33-1.335	SF10/Au/Si/WS_2	155.68	NG
	633	1.33-1.335	SF10/Au/Si/MoS_2	131.7	NG
	633	1.33-1.335	SF10/Au/Si/WSe_2	141.4	NG
	633	1.33-1.335	SF10/Au/Si/$MoSe_2$	131.68	NG
2017 [65]	632	1.33–1.36	MgF2/Rhodium/graphene	259	69.93
2017 [66]	633	1.334-1.40	SF10/Au/MoS_2/Graphene	87.8	17.56
2018 [67]	632.8	1.33-1.3317	SF11/Ag/Graphene/MoS_2	73.5	4.17
2018 [68]	662	1.32–1.36	CaF2/Ag/BlueP/MoS_2	196.798	NG
2018 [69]	633	1.332-1.335	BK7/Ag/WS_2	125.33	67.745
	633	1.332-1.335	BK7/Ag/graphene	118.33	73.956
	633	1.332-1.335	BK7/Au/WS_2	138.33	38.7
	633	1.332-1.335	BK7/Au/graphene	140	33.92
	633	1.332-1.335	BK7/Ag/Au/WS_2	132	49.07
	633	1.332-1.335	BK7/Ag/Au/graphene	125	55.55
	633	1.332-1.335	BK7/Ag/WS_2/graphene	126.33	48.95
	633	1.332-1.335	BK7/Au/WS_2/graphene	153.33	24.53
	633	1.332-1.335	BK7/Ag/Au/WS_2/graphene	135	39.91
2019 [70]	633	1.330-1.335	BK7/Au/MXene/WS_2/ BP	190.22	15.51

2019 [71]	633	1.33-1.335	BK7/Au/MoS_2/Ni/graphene	229	NG
2020 [72]	633	1.33-1.335	BK7/Ag/$PtSe_2$	162	14.93
	633	1.33-1.335	BK7/Au/$PtSe_2$	165	14.12
2020 [73]	632.8	1.30-1.38	BK7/Au/graphene	165.6	33.12
	632.8	1.30-1.38	BK7/Au/GO	151.87	33.14
	632.8	1.30-1.38	BK7/Au/MoS_2	174.15	29.42
	632.8	1.30-1.38	BK7/Au/WSe_2	179.32	30.48
2021 [74]	633	1.33-1.39	SF10/Au/α-SnSe2/phosphorene	96.43	12.36
	633	1.33-1.39	SF10/Ag/α-SnSe2/phosphorene	81.43	46.53
	633	1.33-1.39	SF10/Cu/α-SnSe2/phosphorene	74.29	14.34
2021 [75]	632.8	1.33-1.335	BK7/Au/Ag/Silicon/MXene	274	36.88
	632.8	1.33-1.335	BK7/Au/Ag/Silicon/MoS_2	246	34.1
	632.8	1.33-1.335	BK7/Au/Ag/Silicon/Graphene	297	39.75
2021 [76]	632.8	1.33-1.335	BK7/Ag/Si/MXene	231	39.83
2022 [77]	633	1.375-1.4	BK7/Ag/$TiSi_2$/BP	218	45.26
2022 [78]	633	1.33-1.36	BK7/Au/TaS_2	201	NG
2023 [79]	632.5	1.33-1.45	SF10/ZnO/Ag/Au/$BaTiO_3$/Graphene	116.67	37.87
2024 [80]	633	1.371-1.402	SF10/Cu/$PbMoO_4$/BlueP/TMDC	366.0804	NG

2.5 Evolution and Application of SPR

The evolution of SPR has witnessed a significant transition, expanding its applications from fundamental research to pivotal roles in environmental monitoring [81], food safety [82], biosensors [64], and pharmacology [49].

Heavy metal ions, pesticides, and phenol are environmental pollutants, and can all be detected using SPR sensors. Even in trace amounts, heavy metal ions can cause short- and long-term diseases in people because they are extremely harmful to biological systems. Many industries, including the chemical, plating, and machine industries, make use of heavy metal ions. As the active layer for an SPR optical sensor for the detection of Co^{2+}, a monosodium salt with chitosan and graphene oxide

composite is deposited over a gold thin film [83]. Among the most dangerous heavy metals is cadmium (Cd), which is frequently used in agriculture, industry, and batteries as well as metal alloys and phosphate fertilizers. For detection of Cd^{2+} in water, optical fiber SPR sensor with gold coating is manufactured [84]. Creating thymine(T)-modified gold nanoparticles (AuNPs/T) will enable the development of a fiber-optic SPR to detect Hg^{2+} ion to maintain quality of drinking water [85]. Gold with nanosheets of GeSe enabled us to create a SPR sensor with significantly increased sensitivity towards Pb^{2+} heavy metal ions [86] .

When food is produced from raw materials, is harvested, processed, transported, and stored, it may become contaminated with microorganisms, toxins, or other chemicals that are harmful to humans. Food safety can still be ensured by identifying potential hazards in food. Necrotrophic DNA biomarker helps SPR in detection of pathogenic fungus Colletotrichum Gloeosporioides [87]. The nano MIPs were functionalized over SPR gold chip via an amine-coupling to detect β-lactoglobulin (BLG) [88]. In industrialized nations, allergens in seafood are growing concerns, especially about tropomyosin. Tropomyosin in shellfish can be detected with SPR sensors with gold-patterned biochips. For detection of tropomyosin, the gold- based SPR sensor chips were initially chemically treated with a cysteine solution. Subsequently, these modified chips were employed as a substrate for immobilizing TM-mAb [89]. Leafy vegetables have a history of being linked to infamous outbreaks that result in serious illnesses. To ensure food safety, potential contamination must be identified quickly and accurately. A gold metal based SPR assay has been developed to detect Salmonella Typhimurium in leafy vegetables [90]. With suitable environmental conditions, toxigenic fungi produce mycotoxins, which are harmful secondary metabolites. Several foods, including wheat, corn, beans, peas, peanuts, and other beans, contain mycotoxins. Using an SPR sensor chip with a self-assembled monolayer (SAM) helps for rapid mycotoxin detection in corn and wheat samples [91]. SAM immobilized the antigen on the surface of the sensor chip . The bacteria Escherichia coli (E. coli) causes food poisoning can be detected with the gold based SPR sensor in spinach [92].

More than 400 diseases can now be detected by DNA molecular diagnostics through advancements in biosensor technology, and this number is always rising. SPR is an effective option for biosensing due to the minimal pre-processing and real-time measurement capabilities. In the context of DNA detection, the SPR sensor based on tungsten disulfide provides superior resolution compared to the SPR sensor based on graphene [93]. For protein detection, a numerical analysis of semiconductor germanium (Ge) with graphene on copper based SPR sensor was designed [94]. To identify the nucleoprotein (NP) of H1N1 influenza virus, SPR sensor chip functionalized with protein G solution [95]. After the gold SPR chip was treated with 4-mercaptobenzoic acid (4-MBA), it enabled real-time monitoring for the presence of different Ebola virus monoclonal antibodies (mAb1, mAb2, and mAb3) [96]. A novel approach for diagnosing HAV infection involves the detection of HAV antibodies in human serum samples through the application of the SPR-HAVP1 assay, which combines Surface Plasmon Resonance (SPR) with the major capsid protein VP1 [97]. SPR is being used to diagnose dengue infections [98]. A SPR featuring a composite of platinum diselenide and graphene coating was engineered and simulated to ascertain hemoglobin levels in blood samples and glucose concentrations in urine samples [99]. Furthermore, Table 2.2 contains details of various applications utilizing the SPR sensor.

Table 2.2 SPR Sensor Applications

Application	**wavelength (nm)**	**RI Detection Range**	**Year**
Environmental monitoring			
Mercury Detection	360-1700	NG	2016 [100]
Environmental Sensing in Aqueous Samples	650	1.33-1.35	2016 [101]
Pharmacological Application	600-1024	1.33-1.335	2016 [49]
Mercury Detection	350-700	NG	2017 [102]
Detection of Pesticides	NG	NG	2017 [103]
Metal Ion Detection	670-830	NG	2018 [83]
Pesticide Analysis: Comparative Study for Environmental Water Samples	365	NG	2019 [104]
Mercury Detection	360-700	NG	2020 [105]
Pb2+ Heavy Metal Ions	300-1000	1.333-1.3605	2020 [86]
Mercury Ion Detection	200-1200	NG	2021 [85]

Cadmium Ions' Trace-Level Detection	400-1000	1.333-1.334	2022 [84]
Detection of Hg2+	633	1.33-1.36	2022 [78]
Fuel			
Gas	662	1.32–1.36	2018 [68]
Adulteration in Diesel and Petrol by kerosene	300-900	1.428-1.448	2018 [106]
Detection of Phenol	632.8	NG	2020 [107]
Measurement of dissolved organic matter (DOM) in water	200-450	1.33-1.355	2022 [108]
Adulteration in Fuel	1500-5000	1.4463-1.464	2023 [109]
Biosensor			
Dengue Virus Rapid Diagnostic Test for Igm Antibody Detection	633	1.33-1.34	2015 [110]
Detection of DNA Hybridization	633	1.334-1.40	2017 [66]
Protein Detection	633	1.43-1.435	2018 [94]
Detection of DNA Hybridization	633	1.33-1.4	2018 [93]
Bacteria	633	1.33–1.4	2018 [111]
Molecular Biosensing	527-539	1.33-1.46	2018 [112]
Candida albicans antigen identification	350-800	1.33-1.46	2018 [113]
Biosensing	633	1.33–1.335	2019 [71]
DNA	633	1.33–1.39	2020 [114]
Detection of H1N1 Influenza Virus	300-700	NA	2020 [95]
Sensing of Ebola Virus	670	NG	2020 [96]
cortisol detection	830	NG	2020 [115]
Detection of Hemoglobin in Blood and Urine Glucose Level Samples	632.8	1.32919-1.34995	2021 [99]
Detection of SARS-CoV-2 Nucleocapsid Protein	650		2022 [116]
Dengue Diagnosis	550-650	1.33	2022 [117]
Dengue Virus Detection	633	1.33-1.4	2023 [118]
Detection of Infectious Pathogens	590-605	NG	2023 [119]
Diagnosis of Breast Cancer	250-2000	NG	2023 [120]
Monitoring Cell Evolutions	632.8, 690	1.3385-1.43	2023 [121]
Determination of Hemoglobin Content in Human Blood	633	1.34-1.37	2024 [122]
Plasmonic pregnancy detector	633	1.335-1.343	2024 [123]
Brain Tumor Diagnosis	633	1.3333-1.4412	2024 [124]
Detection of different Cancerous Cell	633	1.360-1.401	2024 [125]

Food Industries			
Detection of Aflatoxin B1, Ochratoxin A, Zearalenone and Deoxynivalenol in Corn and Wheat	NG	NG	2019 [91]
Detection of Donkey Meat Adulteration	785	NG	2020 [126]
Shellfish Major Allergen Tropomyosin	650	NG	2020 [89]
Endotoxin Detection	200-700	NA	2021 [127]
Detection of Hydrogen Peroxide	450-900	1.335-1.36	2021 [128]
Detection of necrotrophic DNA marker of anthracnose causing Colletotrichum Gloeosporioides fungi in harvested produce	400-1000	NG	2021 [87]
Milk Adulteration/Contamination Detection in Camel, Buffalo, and Cow Milk	632	1.3450-1.3472	2023 [129]
Detection of fat concentration milk	NG	1.3452–1.3657	2024 [130]
Detecting honey adulteration	632.8	1.3766-1.39	2024 [131]

2.6 Summary

The chapter summarizes the basic concept of plasmon extending to surface plasmon. The Lorentz-Durde model provides insight into electron behaviour in metals. This model has been very effective in describing a wide range of experimental facts about the behaviour of electrons in metallic systems, particularly when considering their responses to both electrical and optical stimuli. The electromagnetic theory of SPR centers on the coupling of incoming light and a metal-dielectric interface. At a particular angle of incidence, when the light contacts the metal-dielectric interface, it induces collective oscillations of free electrons on the metal's surface, excites the SPP`s. This resulted in maximum absorption of the incident photons. This excitation leads to a sharp dip in the reflected light intensity, confirming the excitation of SP. SPR is a powerful tool for real-time, label-free detection and analysis of molecular interactions. SPR's versatility is demonstrated in detecting pollutants such as heavy metals, pesticides, and phenol, addressing food safety by identifying contaminants, and excelling in DNA diagnostics, detecting over 400 diseases with superior resolution in DNA and protein detection. Its broad applications emphasize SPR's pivotal role in advancing biosensor technology.

CHAPTER 3

COMPUTATIONAL METHODOLOGY

The chapter commences by investigating different strategies to enhance SPR technology through numerical models. Different Numerical models are studied to understand sensor behavior. The performance parameters of SPR sensor are thoroughly studied. Simulation process for MATLAB and COMSOL Multiphysics are studied for designing proposed numerical model.

Chapter 3

3.1 Introduction

To understand the reflectance and transmission coefficient, it is important to study the behavior of light when it encounters an interface between two different media, typically a rarer and denser medium. These coefficients can be used to calculate the amount of light that is reflected or transmitted at the interface, enabling to optimize the efficiency and performance of SPR sensors. There are different models available to determine these coefficients for specific interfaces of materials. The most commonly used models, including the Fresnel equations, and the Transfer Matrix Method (TMM), are also covered in this chapter. Building on the comparison, it examines why the TMM is deemed more effective than the Fresnel model with an increasing number of layers, while also investigating the potential limitations or challenges of the Fresnel based model.

Lastly, the chapter expands the subject to encompass the several simulation software choices that may be employed to analyze this complex structure, either using numerical or graphical techniques. To design the multi layered numerical model, the required steps for simulations are studied for MATLAB programming and the COMSOL Multiphysics environment. The chapter assesses the effectiveness of these software tools in simulating the model based on TMM. Overall, the chapter provides a comprehensive understanding of SPR curves and the parameters that influence its performance. Exploring numerical models and simulation software provides readers with insights on analyzing and enhancing the performance of sensor systems.

3.2 Numerical Model

To analyses the optical characteristics of multi-layer systems, the Fresnel equation system is the best tool. F. Abelés first introduced it roughly 50 years ago [132]. The study of different numerical models contributes useful information for the optimization and designing of SPR sensors with diverse layer configurations, advancing our understanding of their reflective properties.

3.2.1 Fresnel Equations

As previously stated in section 2.3.2 with help of Eq. 2.60, there is no possibility of the surface wave at the metal dielectric interface for TE polarization (s- polarization). Therefore, the Fresnel equations for the p-polarized wave (TM polarization) are as follows. The electric fields of incident and reflected light waves oscillate within the same plane in p-polarization [133]. This plane is known as the plane of incidence. Consider the interface of two mediums. Reflection and transmission of p-polarized light wave are shown in the Fig. 3.1.

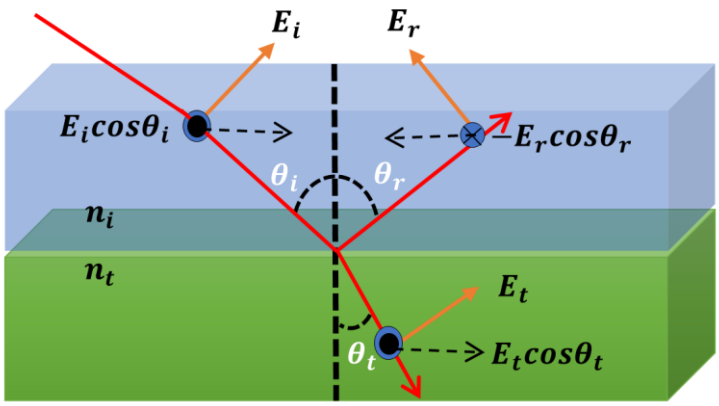

Fig. 3.1 Reflection and Transmission of P-Polarized Light Wave

Where the subscripts i, r, and t represent p-polarized light incidence, reflection, and transmission, respectively. According to boundary conditions,

$$E_i \cos\theta_i - E_r \cos\theta_r = E_t \cos\theta_t \tag{3.1}$$

$$B_i + B_r = B_t \tag{3.2}$$

as known,

$$\therefore B = \frac{E}{v_g}$$

and

$$v_g = \frac{c}{n}$$

$$\therefore B = n\,\frac{E}{c}$$

$$\Rightarrow n_t \frac{E_t}{c} = n_i\left(\frac{E_i}{c} + \frac{E_r}{c}\right)$$

$$E_t = \frac{n_i}{n_t}(E_i + E_r)$$

$$E_i \cos\theta_i - E_r \cos\theta_r = \frac{n_t}{n_t}(E_i + E_r)\cos\theta_t$$

$$\because \theta_i = \theta_r$$

$$r_p = \frac{E_r}{E_i} = \frac{n_t \cos\theta_i - n_i \cos\theta_t}{n_t \cos\theta_i + n_i \cos\theta_t} \tag{3.3}$$

$$t_p = \frac{E_t}{E_i} = \frac{2n_t \cos\theta_i}{n_t \cos\theta_i + n_i \cos\theta_t} \tag{3.4}$$

For p-polarized light, Eqs. 3.3 and 3.4 are amplitude of reflection and transmission coefficients. Reflectance can be explained as an amount of reflected power to incident power. It can be calculated as [133]

$$R = \frac{I_r A_r}{I_i A_i} \tag{3.5}$$

Where A_i *and* A_r are areas of reflection and incident, such as $A_i = A_r$.

$$R = \frac{I_r}{I_i} = \left|\frac{E_r}{E_i}\right|^2 = |r_p|^2 \tag{3.6}$$

The examination of multilayer systems, particularly the 3-layer and 4-layer structures involving prism, metal, and dielectric layers, has provided valuable insights into the reflective characteristics of SPR sensors. The analysis reveals that alterations in

thickness and composition of these layers significantly impact the reflectance of the SPR structure. For instance, the 3-layer system, consisting of prism, metal, and dielectric layers, demonstrates a simple yet effective configuration. On the other hand, the more complex 4-layer system, including two dielectric layers, presents additional considerations for optimizing SPR performance. As the number of layers increases in an N-layer system, calculating reflectance becomes more complex, emphasizing the need for efficient methods such as the transfer-matrix method to manage the growing complexities in sensor such as SPR.

3.2.2 Transfer Matrix Method N-layer system

In 2012, the transfer matrix method (TMM) is a method used in nanophotonic to analyze the propagation of EMs through a stratified medium comprising of several homogeneous layers [134]. This method demonstrated remarkable versatility, enabling precise modeling of wave behavior in complex multilayer systems. In 2019, it has been noticed that TMM can compute a multilayer structure's radiative characteristics more elegantly, such as transmittance and reflectance [135]. In a multilayer structure, the 2x2 matrix describing each layer depends solely on the thickness and complex refractive index of the layer. The system matrix, derived by multiplying all of the layer matrices, describes the entire stratified structure.

To analyze and compute the performance parameter of multilayer SPR configurations, the reflection and transmission coefficients have been computed by using this matrix method. Let us assume a generalized N-layer model, where the different layers are stacked along the z-direction (layer 1: glass prism, layer N: analyte) as illustrated in Fig. 3.2 to compute reflection and transmission coefficients. By sequentially multiplying these individual layer matrices, a system matrix is obtained, which encapsulates the optical behavior of the entire stratified structure.

All the layers are isotropic, non-magnetic, and homogeneous in Fig 3.2. The arbitrary medium layer is defined by thickness d_k, dielectric constant ε_k, permeability μ_k, and refractive index n_k, where k = 2, 3, 4,….(N-1).

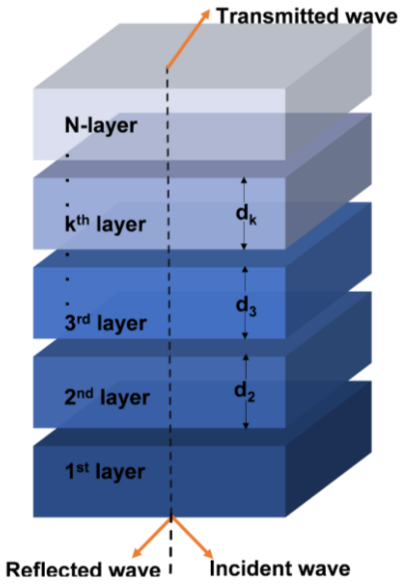

Fig. 3.2 N-layer schematic diagram

The expression for tangential components of electric and magnetic fields at the first boundary (E_1, H_1) and in at the last boundary (E_{N-1}, H_{N-1}) as follows

$$\begin{bmatrix} E_1 \\ B_1 \end{bmatrix} = M \begin{bmatrix} E_{N-1} \\ B_{N-1} \end{bmatrix} \tag{3.7}$$

For the **Transverse magnetic wave** (TM mode), Transfer Matrix M can be written as

$$M_{ij} = \left(\prod_{k=2}^{N-1} M_k \right); i, j = 1, 2 \tag{3.8}$$

where, $$M_k = \begin{pmatrix} \cos\beta_k & -(i\sin\beta_k)/q_k \\ -iq_k \sin\beta_k & \cos\beta_k \end{pmatrix};$$

and $$q_k = \frac{\sqrt{(\varepsilon_k - n_1^2 \sin^2\theta)}}{\varepsilon_k};$$ also $$\beta_k = d_k \left(\frac{2\pi}{\lambda} \right) \sqrt{(\varepsilon_k - n_1^2 \sin^2\theta)}$$

n_1 is RI value of the prism, θ is the angle at which light incidence at the normal to the interface, ε_k is the dielectric constant of kth layer, d_k is the thickness of kth layer. For

p-polarized light, the total matrix M of the whole system's complex reflection and transmission coefficients, R and T, in terms of the matrix elements $M_{(i,j)}$ are given as [134,135]:

$$R = \left| \frac{(M_{11} + M_{12} q_N) q_1 - (M_{21} + M_{22} q_N)}{(M_{11} + M_{12} q_N) q_1 + (M_{21} + M_{22} q_N)} \right|^2 \tag{3.9}$$

$$T = \left| \frac{2 q_1}{(M_{11} + M_{12} q_N) q_1 + (M_{21} + M_{22} q_N)} \right|^2 \tag{3.10}$$

3.3 Performance Parameters

The SPR phenomenon gives rise to an EF that undergoes exponential decay into both the metal and dielectric regions. When the plasmon is stimulated, it generates a propagating wave along metal-dielectric interface, but this wave is absorbed after traveling a certain distance.

3.3.1 Sensitivity

Various definitions of sensitivity have been explored in literature [35,136]. When the wavelength is held constant, sensitivity is described as the ratio between the shift in resonance angle and the change in refractive index of the sensing medium (refer to Fig. 2.6). The mathematical expression for sensitivity is formulated as follows [137]:

$$S = \frac{\Delta\theta}{\Delta n} \tag{3.11}$$

Where $\Delta\theta$ is change in resonance angle and Δn is variation in the sensing layer refractive index after biomolecular interaction. It has unit degree/RIU.

3.3.2 Detection Accuracy (DA)

Detection Accuracy can be computed with the ratio of the change in resonance angle to SPR curve`s full width at half maximum (FWHM). It has dimensionless unit [138].

$$D.A = \frac{\Delta\theta}{FWHM} \tag{3.12}$$

Where FWHM is a parameter used to characterize the resolution of peaks in an SPR curve, directly influencing D.A. It represents the width of the curve at half of its maximum amplitude. Specifically, FWHM is calculated as the difference between the two x-values where the curve's height equals half of the maximum value. For instance, if R_{max} is the maximum value of the SPR curve, determine the half of R_{max}, illustrated in Fig. 3.3 below:

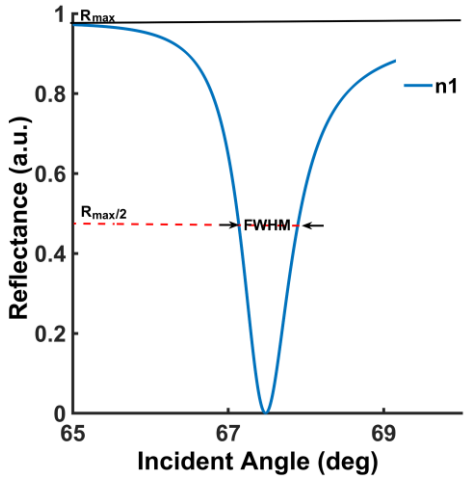

Fig. 3.3 Analysis of SPR curve highlighting FWHM determination.

3.3.3 Figure of Merit (FOM)

The Figure of Merit (FOM) is a crucial parameter for evaluating the overall performance of SPR sensors. It combines two essential aspects of sensor functionality, namely sensitivity and resolution into a single metric, offering a comprehensive assessment of the sensor's capability. FOM provides a standardized way to compare different SPR sensor designs and configurations. While high sensitivity is desirable for detecting small refractive index changes, a broad resonance curve (high FWHM) can reduce the precision of measurements. FOM helps balance these two factors, ensuring that sensors are not only sensitive but also capable of precise measurements. FOM can be

calculated by dividing the sensitivity of a sensor by the FWHM of its SPR curve. It has dimension of RIU^{-1} [139]

$$FOM = \frac{S}{FWHM} \tag{3.13}$$

FOM serves as a guide for optimizing sensor parameters, such as the choice of materials, layer thickness, and coupling techniques. By maximizing the FOM, designers can achieve better performance tailored to specific applications.

3.3.4 Electric Field intensity ($E_{||}$)

The evanescent field intensity E_{Π} is directly proportional to the ability of the SPR sensor to detect minute changes in the refractive index near the sensor surface. A stronger E_{Π} leads to a more pronounced interaction with the analyte, enhancing detection sensitivity. A higher electric field intensity E_{Π} results in a stronger resonance dip in the reflected light intensity, improving the sensor's signal-to-noise ratio. The Electric Field intensity at the sensor interface can be calculated with the help of magnetic field ($H_{\perp}$) as follows [140]

$$H_{\perp} = \frac{2q_1}{(M_{11} + M_{12}q_N)q_1 + (M_{21} + M_{22}q_N)} \tag{3.14}$$

$$E_{\Pi} = \left(\frac{\mu_N n_1}{\mu_1 n_N}\right) H_{\perp} \tag{3.15}$$

This relationship facilitates accurate modeling and simulation of SPR phenomena, which is vital for sensor calibration and design.

3.4 MATLAB

For data analysis, algorithm development, and model creation, millions of engineers and scientists utilize the programming and numeric computing platform MATLAB. MATLAB supports matrix manipulation, algorithm development and implementation, data and function visualization, and interfacing with programs written in

other languages with valuable user interface building platforms. The procedural workflow for this simulation begins with the establishment of global constants and variables, serving as foundational elements for subsequent computations. Initialization in MATLAB involves clearing previous simulations and data, ensuring a clean slate for the upcoming analysis. In the realm of MATLAB programming, the distinction between local variables and those declared as global is paramount. When a variable is defined as global, its value becomes accessible across multiple functions, facilitating collaborative data sharing.

Moving forward, the simulation delves into the calculation of permittivity, a pivotal step necessitating the utilization of variables representing the real and imaginary parts of the refractive index. This computation yields the permittivity values for each material under consideration. The optimization of layer thickness takes center stage in the subsequent phase, with a focus on achieving Rmin value. A dedicated function generates the TMM matrix for various thickness values, thereby facilitating the optimization process. The variable responsible for thickness adjustment is passed from the main program to this function, ensuring seamless integration. Such a modular approach not only enhances computational efficiency but also ensures adaptability to various material configurations. Critical to the study is the determination of the incident angle for the sensing medium before and after binding interaction. This involves plotting SPR curves, showcasing the incident angle's evolution from 30 to 90 degrees. These plots serve as visual representations of the interaction dynamics, capturing subtle shifts in the SPR response due to binding effects. This dynamic range captures the nuances of the material interaction, shedding light on the binding effects. The final step involves the calculation of performance parameters, leveraging the information embedded in the SPR curves. These parameters serve as quantitative metrics, offering insights into the overall performance of the system. The interplay of global constants, variable definitions, permittivity calculations, thickness optimization, incident angle variations, and performance parameter assessments collectively shapes a comprehensive and insightful simulation, as depicted in Fig. 3.4.

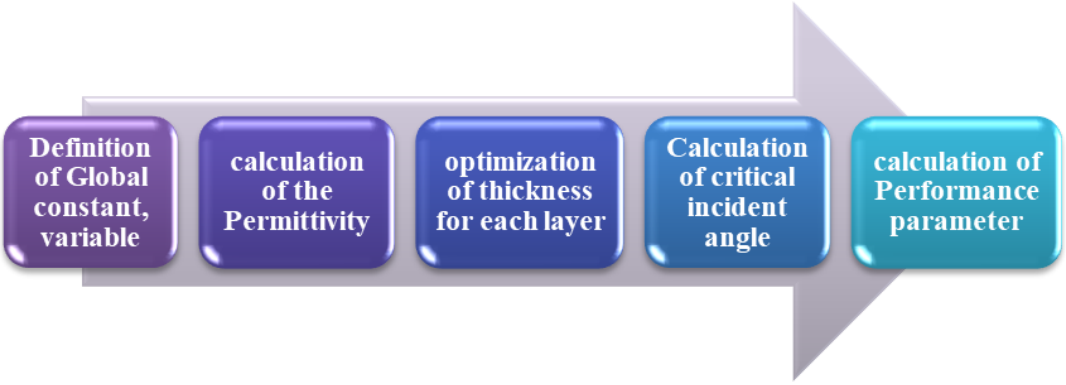

Fig. 3.4 Procedure

3.5 COMSOL

COMSOL Multiphysics environment is a simulation platform that applies any physical effect to model. Being a flexible platform, it enables users to simulate the necessary physical components of their designs.

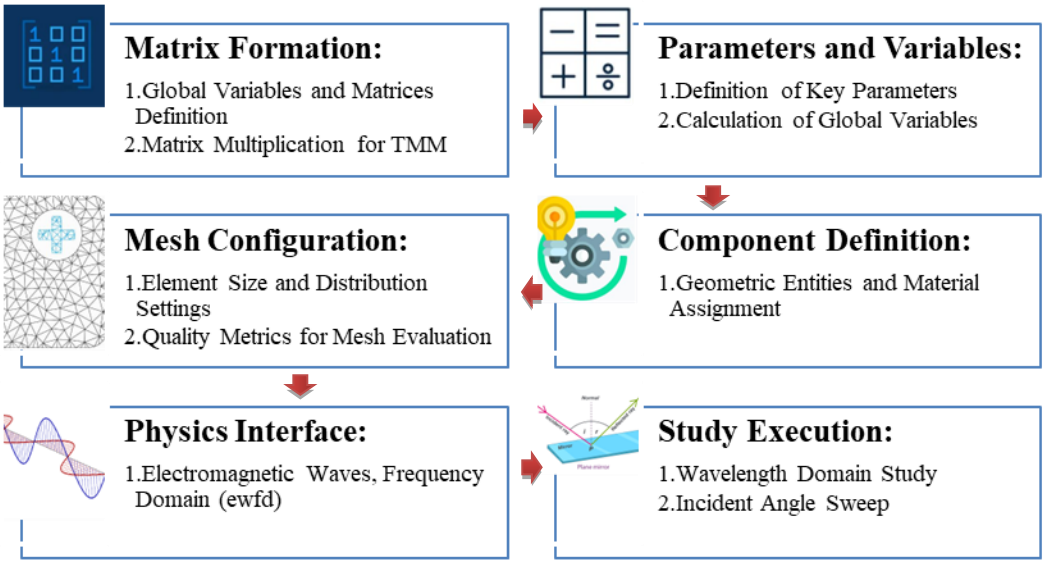

Fig. 3.5 Work flow of the COMSOL

Additionally, COMSOL Multiphysics offers lots of advantages for tackling issues. The use of COMSOL Multiphysics aids in problem comprehension while beginning a new project. The presented COMSOL Multiphysics workflow in Fig. 3.5 encapsulates a

meticulous process of configuration. Figure 3.5 describes a simulation environment that is used to analyse the optical characteristics of a structure with several layers. Here is a detailed description of each section:

- *Matrix Formation*: This section establishes the foundation for simulation by defining global variables and matrices crucial for subsequent computations. Matrices for different layers, such as Metal, Semiconductor, and 2D material, are formulated. The final TMM matrix is derived through matrix multiplication, encapsulating the intricate interactions within the proposed structure.
- *Parameters and Variables:* Critical parameters essential for the modeling process are defined in this section. These include refractive indices, wavelength, frequency, incident angle, and thicknesses of various layers. These parameters serve as the building blocks for the subsequent simulation steps. Global variables are introduced at the geometric entity level, incorporating expressions that calculate complex relative permittivity and matrix variables for each layer. These variables form the basis for subsequent computations, providing a dynamic foundation for the simulation.
- *Component Definition:* This section delves into the geometry of the study, defining domains and boundaries. Different materials are assigned to each domain, reflecting the physical structure under investigation. The properties of each material are meticulously detailed, laying the groundwork for accurate and comprehensive simulations.
- *Mesh Configuration:* Mesh Configuration is configured to achieve an optimal balance between accuracy and computational efficiency. Various mesh elements are described, and their statistics are provided to gauge the quality of the mesh. The meshing process is crucial for obtaining reliable simulation results.
- *Physics Interface:* The physics interface is selected for the study, with a focus on wave optics. Physics-controlled mesh settings are defined, ensuring the accuracy of the simulation. Input and output ports are established for incident and

transmitted waves, providing a means to analyze the behavior of electromagnetic waves within the defined geometry.

- *Study Execution:* This section provides essential computation information, including the time taken, CPU details, and the operating system. The study is executed in the wavelength domain, and an auxiliary sweep is performed over a range of incident angles. This step ensures a comprehensive exploration of the parameter space.

In essence, this workflow in COMSOL Multiphysics is a systematic and comprehensive approach, integrating variable definitions, matrix formulations, geometry establishment, and physics selection. It provides a robust foundation for simulating and understanding the optical properties of complex structures, offering insights into their behavior under various conditions. For more detailed information on the boundary conditions applied in these simulations, refer to the appendix.

3.6 Summary

Numerical models, namely Fresnel equations and TMM, are essential tools for understanding the behavior of SPR sensors with varying layer configurations. The Fresnel equations, particularly for p-polarized waves, provide insights into reflection and transmission coefficients, enabling the calculation of reflectance. TMM method allows for the calculation of reflectance and transmittance in a multilayer structure, presenting a more refined way to assess SPR sensor performance. The examination of N-layer systems, where each layer is characterized by its thickness and complex refractive index, emphasizes the need for efficient methods in dealing with growing complexities in sensor design.

Sensitivity (S), detection accuracy (D.A), and figure of merit (FOM), of SPR performance parameters are discussed. The simulation of these concepts is facilitated through MATLAB and COMSOL Multiphysics environments. MATLAB, a powerful numeric computing platform, is utilized for algorithm development, data analysis, and

model creation. It offers a procedural workflow that involves the calculation of permittivity, optimization of layer thickness, incident angle variations, and the determination of performance parameters.

COMSOL Multiphysics, a versatile simulation platform, is employed for its ability to apply physical effects to complex model structures. The COMSOL Multiphysics workflow involves matrix formation, parameter and variable definition, component and mesh configuration, physics interface selection, and study execution. This systematic approach ensures a comprehensive analysis of the optical properties of multi-layered structures, providing valuable insights into their behavior under various conditions.

CHAPTER 4

OPTIMIZATION OF SPR CONFIGURATIONS: EXPLORING THE INFLUENCE OF NOBLE METALS AND PRISM MATERIALS

This theoretical study explores the sensitivity of SPR sensors when exposed to an alcoholic sensing medium. The sensing medium is alcohol, with concentrations varying at 0%, 20%, 50%, 80%, and 100%. The sensitivity assessed across different SPR configurations, considering five prism materials and three noble metals. The performance of each configuration comparatively evaluated in terms of sensitivity.

Chapter Built Upon

- **T. M. S. Ashrafi** and G. Mohanty, "Sensitivity calculation for different prism material based surface plasmon resonance sensor: a comparative study," in J. Phys. Conf. Ser. **2267(**1), p. 012089, IOP Publishing, May 2022.

Chapter 4

4.1 Introduction

In the previous chapters, the fundamentals of SPR sensor and its various applications are discussed. One key observation drawn from the previous chapters is that SP cannot be produced by direct light illumination over a metal-dielectric medium. To excite SP, a third medium, for example, a glass prism is required. Following the theoretical foundations of SPR, Otto and subsequently Kretschmann devised a three-layer conventional configuration for SPR sensor [27,28]. A 2013 study found that when the refractive index of the glass prism material increases, the FWHM decreases. In other words, the resonance peak becomes narrower. This indicates that the sensor's sensitivity to environmental changes increases, allowing for more exact measurements [137]. This suggests that the choice of prism material plays a significant role in the performance of SPR sensors and should be carefully considered in sensor design. Therefore, it is necessary to study the impact of different prism materials on the performance of SPR.

In SPR, understanding the behaviour of metals is important, especially in their interaction with light. This interaction is key to the functionality of SPR sensors, as the free electrons on the metal's surface can resonate with incident light at specific wavelengths, a phenomenon central to SPR-based detection. This is due to the ability of electrons on the metal's surface to absorb and re-emit light at specific wavelengths. Furthermore, a significant finding from the preceding chapter's is that active noble metals such as gold (Au), silver (Ag), copper (Cu), and aluminum (Al) are seen to have a noteworthy impact on the SPR response [72,74,141]. The study is also required to understand the effect of these metals on the performance of SPR sensor. In this chapter, the conventional SPR structure is investigated by optimizing it with various noble metals and different prism materials. The crucial performance parameter i.e., sensitivity, has been examined for all proposed SPR configurations. Additionally, the sensitivity is investigated by varying the sensing medium's concentration, such as alcohol in water. Finally, a comparison study has been made between the outcomes.

4.2 Computational methodology

The Kretschmann configuration, known for its popularity and reliability, is widely used for the excitation of SPs [28]. When the wave vector of the incoming light aligns with that of the SP, an SPW is produced at the interface. This represents the fundamental condition and can be expressed mathematically as [21,142], $k_x = k_{spp}$

$$\frac{2\pi}{\lambda} n_p \sin\theta_R = \frac{\omega}{c}\sqrt{\frac{n_m^2 n_s^2}{n_m^2 + n_s^2}} \tag{4.1}$$

Where n_p is the refractive index of the prism at the vicinity of the interface, λ is the wavelength of incident light and c is the velocity of n_m and n_s is the refractive index of metal and sensing medium. The schematic diagram of the SPR sensor is shown in Fig. 4.1.

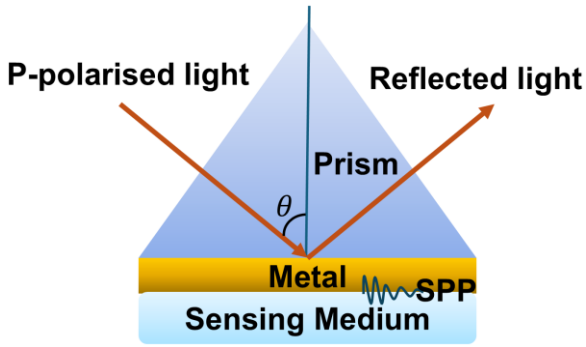

Fig. 4.1 Schematic diagram for SPR sensor

This sensor comprises three distinct layers: a prism, a noble metal, and a sensing medium. Five prism materials, such as BK7, SF5, SF10, SF11, and Sapphire (Al2O3) are considered in this study, which were also mentioned in our prior work [143]. The noble metals used are copper (Cu), silver (Ag), and gold (Au). The sensing medium is a water-alcohol combination with varying alcohol concentrations. The study involves five alcohol concentrations in water, each associated with specific refractive indices: 1.3317 (RIU), 1.3450 (RIU), 1.3578 (RIU), 1.3611 (RIU), and 1.3573 (RIU), representing 0%, 20%, 50%, 80%, and 100% alcohol content, respectively [144]. The refractive index of Au, Cu,

and Ag are 0.18344 + j3.4332, 0.26965 + j3.4106, and 0.056206 + j4.2776 respectively, having unit RIU for each, taken at wavelength 633 nm [38]. RI values of BK7, Sapphire, SF5, SF10, and SF11 are 1.5151(RIU), 1.7659(RIU), 1.6685(RIU), 1.7231(RIU), and 1.7786 (RIU) respectively [34]. In this study TMM is implemented for the calculation of minimum reflectance, resonance angle, and hence sensitivity.

In this study TMM is implemented for the calculation of minimum reflectance, resonance angle, and hence sensitivity as discussed in chapter 3. For TM-polarised light, the total reflectance for a multilayer (N) structure can be written as

$$R = \left| \frac{(M_{11} + M_{12} q_N) q_1 - (M_{21} + M_{22} q_N)}{(M_{11} + M_{12} q_N) q_1 + (M_{21} + M_{22} q_N)} \right|^2 \tag{4.2}$$

In the Eqs. 4.2, M_{ij} is called as characteristic matrix of the system, and its value can be calculated by using Eqs. 3.8 and 3.9 of chapter 3. R is a dimensionless quantity.

4.3 Result and Discussion:

The analysis involves various SPR configurations, specifically focusing on the sensitivity of these configurations for three active noble metals: gold (Au), silver (Ag), and copper (Cu). These metals are applied to the surface prism, with five distinct prism materials considered: BK7, Sapphire, SF10, SF11, and SF5 optical glasses.

4.3.1 Silver

For the simulation, the TMM is employed to investigate the configuration BK7 glass | Silver | Sensing Medium (alcohol in water) and determine the resonance angle (θ_R). The SPR intensity curve for the said configuration of 0% alcohol in water is visualized in Fig. 4.2.

The aforementioned is followed by the measurement of θ_R, which is also called the SPR angle. Following this, as the concentrations of alcohol in water are incrementally raised (i.e., 20%, 50%, 80%, and 100%), the corresponding resonance angles are computed. The resonance angles corresponding to 0%, 20%, 50%, 80%, and 100%

alcohol concentrations in water are represented by θ_{R0}, θ_{R20}, θ_{R50}, θ_{R80}, θ_{R100}, respectively. The variation in resonance angle is computed for each increased concentration. Subsequently, the sensitivity is determined using the formula $S = \Delta\theta/\Delta n$, where $\Delta\theta$ and Δn are difference in resonance angle and change in RI of the sensing medium. In this BK7 glass| Silver | Sensing Medium (0% alcohol in water) configuration the values of R_{min0}., θ_{R0}, and optimized silver thickness are 2.1490E-04 (dimensionless), 67.67^0, and 55 nm respectively (shown in Fig. 4.2) [143].

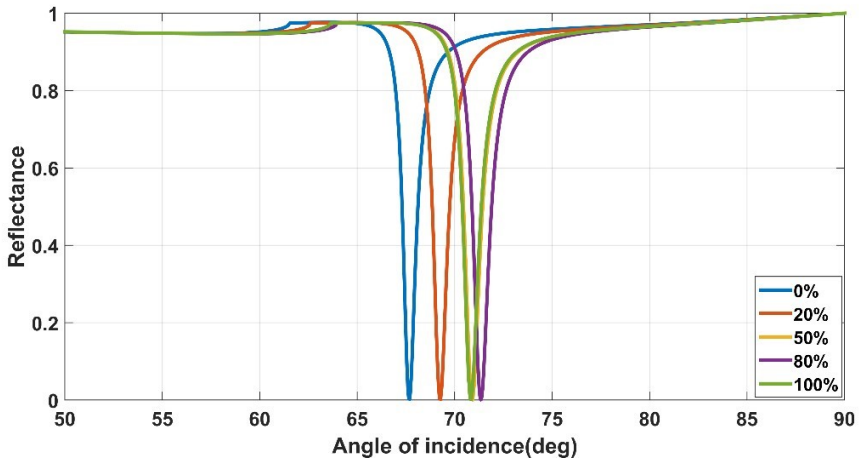

Fig. 4.2 SPR intensity curve for BK7| Ag| Sensing medium at different concentrations.

Figure 4.2 illustrates the resonance angles corresponding to all specified concentrations. Table 4.1 shows the variations in resonance angle for each specified concentration. For 0%, 20%, 50%, 80%, and 100% alcohol concentrations in water, the resonance angles are 67.67^0, 69.254^0, 70.898^0, 71.345^0, and 70.831^0, respectively [143]. For example, when concentration changes from 0 to 20 percent, $\Delta\theta$ and Δn values are found as 1.584^0 and 0.0133 (RIU), respectively. Then the sensitivity of the SPR structure is calculated using the above formula and found that 119.098 ^{0}/RIU when concentration changes from 0 to 20 percent. Similarly, all the sensitivity values are computed for other concentrations and the values are shown in Table 4.1. In the same process, the sensitivities for the rest prism materials (i.e., Sapphire, SF10, SF11, and SF5) are computed and the sensitivity values are shown in Table 4.1 [143].

Table 4.1 Values of resonance angle and sensitivity for silver on different prism materials at different alcohol concentrations.

Prism	0% alcohol	20% alcohol			50% alcohol			80% alcohol			100% alcohol		
	θ_{R0} (deg)	θ_{R20} (deg)	$\Delta\theta$ (deg)	S (^{0}/RIU)	θ_{R50} (deg)	$\Delta\theta$ (deg)	S (^{0}/RIU)	θ_{R80} (deg)	$\Delta\theta$ (deg)	S (^{0}/RIU)	θ_{R100} (deg)	$\Delta\theta$ (deg)	S (^{0}/RIU)
BK7	67.67	69.254	1.584	119.10	70.898	3.228	123.68	71.345	3.675	125.0	70.831	3.161	123.5
SF5	57.169	58.163	0.994	74.74	59.15	1.981	75.90	59.409	2.24	76.19	59.11	1.941	75.82
SF10	54.458	55.354	0.896	67.37	56.239	1.781	68.24	56.471	2.013	68.47	56.204	1.746	68.20
Al_2O_3	52.56	53.395	0.835	62.78	54.217	1.657	63.49	54.432	1.872	63.67	54.185	1.625	63.48
SF11	52.029	52.848	0.819	61.58	53.654	1.625	62.26	53.865	1.836	62.45	53.622	1.593	62.23

4.3.2 Gold

For BK7 glass| Gold | Sensing Medium (0% alcohol in water) configuration, the values of R_{min0}., θ_{R0}, and optimized gold thickness are found 4.8781E-04 (dimensionless), 71.998^0, and 48 nm respectively (shown in Fig. 4.3) [143]. These parameters play a crucial role in defining the performance characteristics of the SPR sensor, ensuring optimal interaction between the metal layer and the sensing medium. The values of sensitivity for active metal gold on various prism materials for 0%, 20%, 50%, 80%, and 100% concentrations of alcohol are presented in Table 4.2 [143].

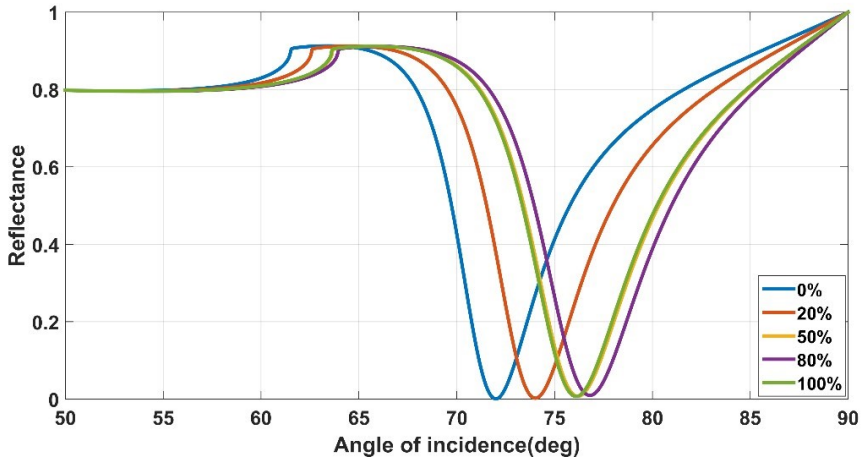

Fig. 4.3 SPR intensity curve for BK7| Au| Sensing medium at different concentrations.

Table 4.2 Values of resonance angle and sensitivity for gold on different prism materials at different alcohol concentrations.

Prism	0% alcohol	20% alcohol			50% alcohol			80% alcohol			100% alcohol		
	θ_{R0} (deg)	θ_{R20} (deg)	$\Delta\theta$ (deg)	S (^{0}/RIU)	θ_{R50} (deg)	$\Delta\theta$ (deg)	S (^{0}/RIU)	θ_{R80} (deg)	$\Delta\theta$ (deg)	S (^{0}/RIU)	θ_{R100} (deg)	$\Delta\theta$ (deg)	S (^{0}/RIU)
BK7	71.998	74.01	2.02	151.59	76.19	4.19	160.65	76.80	4.80	163.40	76.10	4.10	160.3
SF5	60.061	61.22	1.16	86.99	62.37	2.31	88.62	62.68	2.62	89.09	62.33	2.26	88.56
SF10	57.089	58.122	1.033	77.67	59.147	2.058	78.85	59.417	2.328	79.18	59.107	2.018	78.83
Al_2O_3	55.024	55.981	0.957	71.96	56.928	1.904	72.95	57.177	2.153	73.23	56.891	1.867	72.93
SF11	54.448	55.386	0.938	70.53	56.313	1.865	71.46	56.556	2.108	71.70	56.276	1.828	71.41

4.3.3 Copper

The values of R_{min0}., θ_{R0}, and optimized gold thickness for BK7 glass| Copper | Sensing Medium (0% alcohol in water) configuration are found 2.1135E-05 (dimensionless), 72.027^0, and 43 nm, respectively (shown in Fig. 4.4) [143]. Table 4.3 shows the values of sensitivity for active metal copper on different prism materials at different alcohol concentrations.

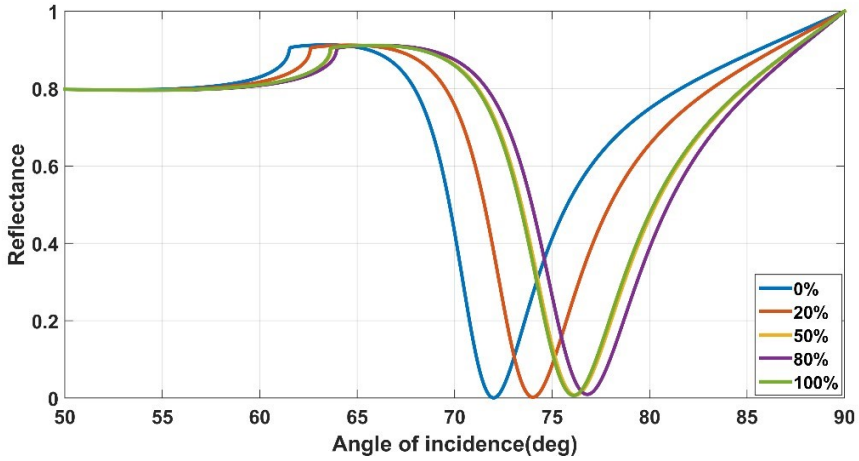

Fig. 4.4 SPR intensity curve for BK7| Cu| Sensing medium at different concentrations.

Table 4.3 Values of resonance angle and sensitivity for copper on different prism materials at different alcohol concentrations.

Prism	0% alcohol	20% alcohol			50% alcohol			80% alcohol			100% alcohol		
	θ_{R0} (deg)	θ_{R20} (deg)	$\Delta\theta$ (deg)	S (^{0}/RIU)	θ_{R50} (deg)	$\Delta\theta$ (deg)	S (^{0}/RIU)	θ_{R80} (deg)	$\Delta\theta$ (deg)	S (^{0}/RIU)	θ_{R100} (deg)	$\Delta\theta$ (deg)	S (^{0}/RIU)
BK7	72.027	73.962	1.935	145.49	76.024	3.997	153.14	76.595	4.568	155.37	75.939	3.912	152.8
SF5	60.252	61.402	1.150	86.47	62.548	2.296	87.97	62.851	2.599	88.40	62.503	2.251	87.93
SF10	57.284	58.313	1.029	77.37	59.334	2.05	78.54	59.603	2.319	78.88	59.294	2.01	78.52
Al_2O_3	55.217	56.173	0.956	71.88	57.118	1.901	72.84	57.365	2.148	73.06	57.08	1.863	72.77
SF11	54.64	55.577	0.937	70.45	56.502	1.862	71.34	56.745	2.105	71.60	56.466	1.826	71.33

Analyzing the information provided in Tables 4.1, 4.2, and 4.3, it is observed that the resonance angle increases with respect to the decrease in RI of prism material at zero concentration of alcohol. This trend persists across all other concentrations. Additionally, the sensitivity analysis reveals that the BK7 based SPR configuration consistently exhibits the highest sensitivity compared to other optical glass prism-based configurations. Notably, the maximum sensitivity is observed in SPR configurations utilizing active Au-metal.

Furthermore, an interesting observation is that as the concentration of the sensing medium increases, sensitivity also rises, reaching its peak at 80 percent alcohol in water. This happens as the sensing medium's RI decreases beyond 80% concentration.

4.4. Summary

A sensitivity comparison of SPR sensors, based on the three layers configuration with three noble metals (Ag, Au, Cu) and five different prisms, is undertaken in this study. Simulations, conducted using MATLAB, analyze performance metrics such as sensitivity and resonance angle shifts, with results summarized in Tables 4.1, 4.2, and 4.3. The findings highlight the noteworthy influence of the refractive index of glass prisms on these parameters. Initially, the study focused on Ag as the active metal and tested it with

different prisms. Among these, the BK7 glass prism demonstrated significantly better performance compared to the other prisms. Encouraged by this result, the study further investigated the performance of BK7 with the other two noble metals, Au and Cu. Notably, the results reveal that the sensitivity, a crucial performance parameter, reaches its peak in the SPR configuration employing a BK7 glass prism, surpassing other prism materials, regardless of the active metal used. The analysis highlights BK7 as the most effective prism material, while SF11 is the least effective, with the remaining materials forming a graded performance spectrum. In addition to the prism materials, the choice of noble metal also plays a critical role in sensor performance. Among the metals under the study, Ag-based configurations provide sharper SPR curves, resulting in a minimum FWHM, which can enhance the detection accuracy of the sensor when compared with other noble metals. Additionally, the study extends its investigation by varying the alcohol concentration in water. Intriguingly, it is established that sensitivity experiences an upward trend, reaching a peak at 80 percent alcohol concentration across all configurations.

A limitation in the study is that Ag and Cu are oxidized materials, whereas Au is a stable material and delivers promising outcomes with all the prisms. However, due to the sharpness of the SPR curve provided by Ag, its performance could potentially be improved by incorporating alternative materials, such as semiconductors and 2D materials over it. This aspect will be further explored in the upcoming chapters.

CHAPTER 5

IMPACT OF VARIOUS HETEROSTRUCTURES COMBINING III-V NITRIDES AND 2D MATERIALS ON THE PERFORMANCE OF SPR SENSOR

This study focuses on enhancing the performance of a surface plasmon resonance (SPR) sensor by strategically integrating diverse heterostructures. These heterostructures involve a semiconductor and a two-dimensional (2D) material, specifically Wurtzite nitride as semiconductor candidates and Transition Metal Dichalcogenide (TMDC) family members as 2D materials. Among the combinations studied, GaN-WS_2 exhibits the highest sensitivity, while AlN-WS_2 performs well in terms of detection accuracy (DA), figure of merit (FOM), and evanescent electric field (EF) intensity factor. Notably, InN-WS_2 and AlN-WS_2 show significant resonance angle changes within specific sensing refractive index (RI) ranges.

Chapter Built Upon

- **T. M. S. Ashrafi** and G. Mohanty, "Highly Sensitive GaN-WS_2-based surface plasmon resonance sensor: A theoretical approach," Plasmonics 17(4), 1673-1680 (2022).
- **T. M. S. Ashrafi** and G. Mohanty, "High-Performance Plasmonic Sensor Using Indium Nitride–Tungsten Disulphide Heterostructure for Bio-Sensing Applications," Iranian Journal of Science, 1-5 (2024).
- **T. M. Ashrafi** and G. Mohanty, "High-Performance SPR Sensor Using Wurtzite Nitride Semiconductors and TMDC: a Comparative Study," Plasmonics, 1-7 (2023).

Chapter 5

5.1 Introduction

In the previous chapter, we discussed different prism and metal combinations in a 3-layer SPR sensor configuration and compared their performance based on sensitivity. Now, to further enhance the performance of the SPR sensor, focus of current work is directed towards the incorporation of different materials, such as semiconductors and 2D materials, into the sensor design. The properties of these materials were extensively discussed in Chapter 2. Chapter 5 embarks on exploring the effects of incorporating these various materials into the SPR sensor design and how they can improve sensitivity and detection limits. Understanding the properties of semiconductors and 2D materials enables us to tailor the sensor configuration for specific applications, thereby optimizing its performance.

Furthermore, recent research in 2021 demonstrated that 5-layer prism based hybrid heterostructures with a double layer of 2D materials effectively improved SPR sensor performance [145]. Previous studies also suggests that the heterostructures offers several advantages, including enhanced sensitivity, better control of electromagnetic fields, increased stability, and potential multifunctionality [49,146]. This insight suggests that a heterostructure combining III-V nitride semiconductor and TMDCs is seen to be a novel approach to developing high-performance SPR sensors, as it allows for precise tuning of the device properties by adjusting the thickness and composition of each layer. Building upon this research, the current study focuses on examining heterostructures composed of semiconductors and 2D materials. The effect of these heterostructures on SPR sensor performance parameters such as sensitivity, FOM, DA, and electric field enhancement factors are now being investigated thoroughly and compared. Additionally, the investigation extends to analyzing the range of refractive indices for which the proposed SPR sensor may yield optimal responses. This will give an in-depth understanding of the sensor's capabilities in different scenarios.

5.2 Computational Methodology

A significant impact of semiconductor materials on SPR performance was brought to light by theoretical study in 2016. This study shows that in comparison to

silicon (Si) and germanium (Ge), wurtzite nitride semiconductors perform better with good sensitivity when integrated into a graphene on gold SPR sensor [147]. In 2021, a study proposed an SPR biosensor with a silicon and 2D MXene (Ti3C2Tx) layer structure, demonstrating the continued advancement of SPR biosensor technology [75]. This progression purposefully combines different materials to improve performance of sensor in visible spectrum applications.

Based on the above, a heterostructure composed of Wurtzite nitride semiconductor and the TMDC materials is coated over the metal layer in the Kretschmann and Raether configuration prior to the interface dielectric medium in this investigation. This structural difference transforms a three-layer system into a five-layer system. The configuration considers a prism such as BK7 with an Ag metal layer coated on its base, followed by semiconductor and 2D materials, and lastly, the sensing medium. The p-polarized light of a He-Ne laser with a wavelength of 632.8 nm illuminates the proposed structure. The proposed design for the SPR sensor in this work is shown schematically in Fig. 5.1, which is adapted from our previous research paper [148].

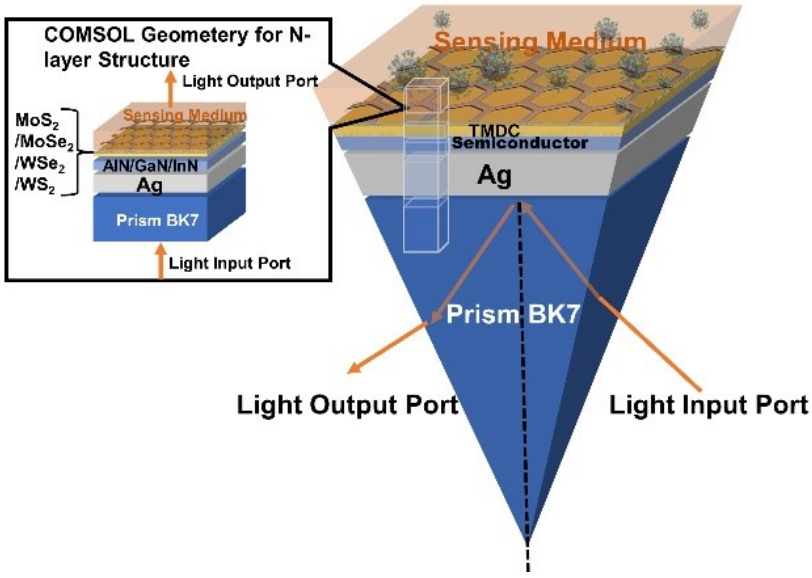

Fig. 5.1 The schematic diagram for the proposed structure of SPR sensor

The numerical model based on the schematic diagram of Fig. 5.1 has been designed utilizing the TMM in MATLAB and the COMSOL Multiphysics environment for a comprehensive analysis. The reflectance, calculated as a function of

the matrix elements M(i,j) of the total matrix M of the complete system using the TMM for p-polarized light, is extensively discussed in Chapter 3. The reflectance (*R*) is expressed as follows:

$$R = \left| \frac{(M_{11} + M_{12} q_N) q_1 - (M_{21} + M_{22} q_N)}{(M_{11} + M_{12} q_N) q_1 + (M_{21} + M_{22} q_N)} \right|^2 \tag{5.1}$$

It has dimensionless unit. Additionally, the magnetic field ($H_\perp$) and electric field intensity (E_Π) are calculated as follows [149]:

$$H_\perp = \frac{2q_1}{(M_{11} + M_{12} q_N) q_1 + (M_{21} + M_{22} q_N)} \tag{5.2}$$

$$E_\Pi = \left(\frac{\mu_N n_1}{\mu_1 n_N} \right) H_\perp \tag{5.3}$$

Electric field measured V/nm in the study. Complementing this discussion, Table 5.1 provides essential information about the refractive indices of the materials involved.

Table 5.1 The refractive indices (RI) of the materials at a wavelength of 632.8 nm.

Materials	**Refractive index (RIU)**
BK7	1.5151 [34]
Ag	0.056253 + 4.2760i [38]
Si	3.8827 + 0.019626i [57]
GaN	2.3848 + 0i [58]
AlN	2.1496+0i [59]
InN	2.9+0i [60]
Graphene	3 + 1.149i [51]
WSe_2	5.2302 + 0.50229i [52]
WS_2	5.0646 + 0.23623i [52]
MoS_2	4.9168 + 1.0554i [52]
$MoSe_2$	5.2069 + 0.92551i [52]

5.3 Results and Discussion

The study commenced with an examination of a conventional three-layer structure consisting of BK7, Ag, and the sensing medium. Subsequently, an investigation is conducted on a four-layer system, wherein Semiconductor or 2D

material is incorporated into the structure. Both the three- and four-layer systems' SPR intensity curves are shown graphically in Fig. 5.2. Figure 5.2 shows the notable impact of InN in relation to the resonance angle θ_R as the RI of the sensing medium increases. The data indicates that InN stands out by contributing the most substantial increase in the resonance angle within the examined structures. This finding underscores the significance of InN in enhancing the performance and sensitivity of SPR, making it a crucial element to consider in the design and optimization of SPR structures for effective sensing applications.

Figure 5.2(a) indicates that the wurtzite nitride semiconductor family yields the maximum shift in resonance angle as compared to silicon or conventional structure of SPR sensor. This represents a pivotal accomplishment in SPR sensor studies, as a greater shift in resonance angle contributes to improved precision in biomolecular interaction measurements. The SPR curve, depicted in Fig. 5.2(b), illustrates the influence of 2D materials directly integrated over Ag without a semiconductor layer in the SPR sensor response .

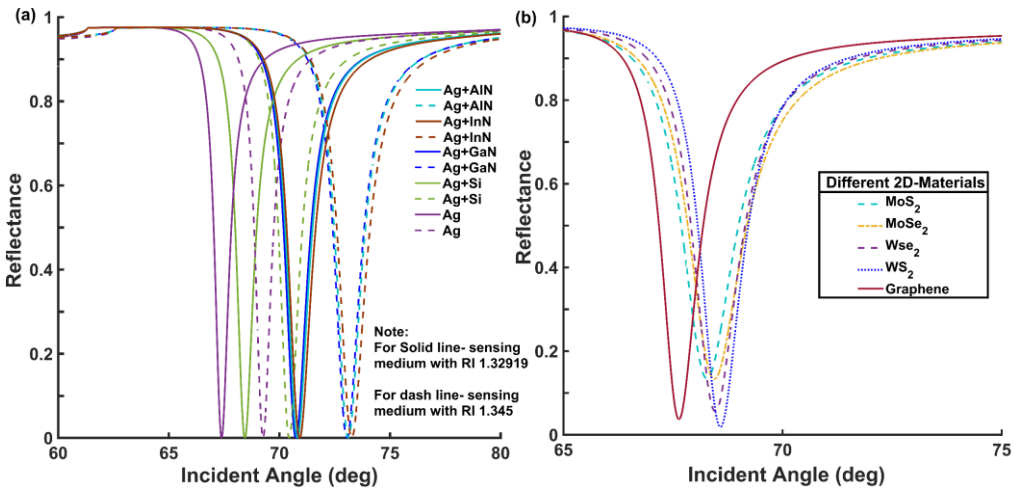

Fig. 5.2 SPR Curves (a) Comparative Study in Three- and Four-Layers Structure, (b) different 2D materials SPR structures without semiconductor on Ag-based SPR structure

Specifically, the findings reveal that among the various 2D materials examined, WS2 stands out by yielding a remarkably sharp SPR curve. This distinctive attribute, highlighted in Fig. 5.2(b), underscores the superior response of the sensor structure when incorporating WS2 in accordance with our prior research [150]. The three-layer

system of SPR demonstrates notable sensitivity, with a value of 118 (°/RIU), DA of 2.174 (dimensionless), and as FOM of 137.53 (RIU^{-1}). Figure 5.3 depicts the effect of introducing various wurtzite nitride semiconductors over the Ag layer in terms of performance parameters like sensitivity, DA and FOM, where sensitivity had unit of °/RIU , DA is dimensionless quantity, and FOM has unit as RIU^{-1} as studied in chapter 3. In reference to the three-layer SPR system, AlN provides a 17.6% improvement in sensitivity. Likewise, inclusion of GaN and InN improved the sensitivity by 23% and 25.9%, respectively. A silicon based SPR sensor, on the other hand, shows just a 7.2% improvement. These observations show that InN based SPR structure provides highest sensitivity because InN has large dielectric constant with zero imaginary part. This observation shows that wurtzite nitride family members give notable performance in SPR configuration as compared to Si.

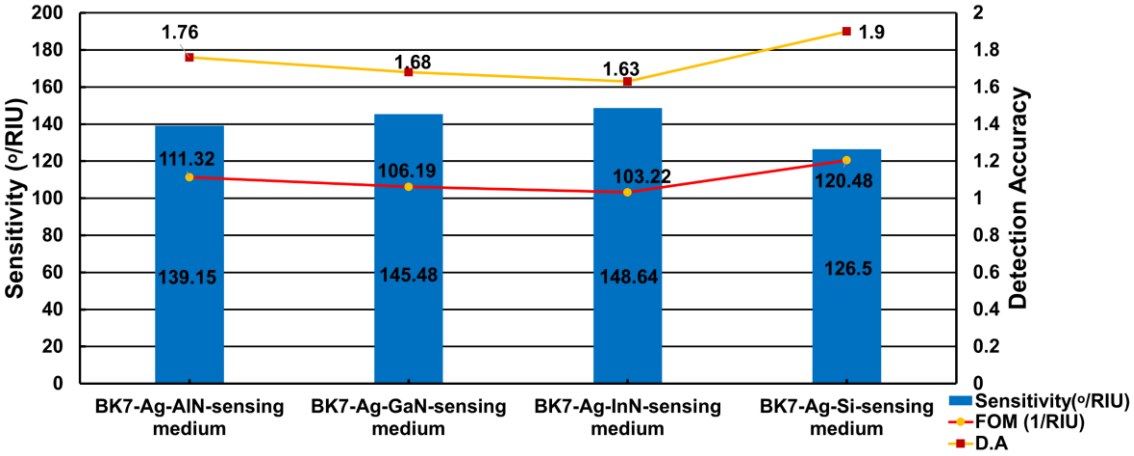

Fig. 5.3 Performance parameters comparison of semiconductor based SPR structure

Figure 5.4 illustrates the performance with 2D material like graphene and TMDC material over Ag in SPR structure. This comparison highlights the potential of 2D materials to boost SPR sensor performance, offering enhanced sensitivity and functionality compared to traditional configurations.The analysis leads to a conclusive observation: the integration of WS_2, a specific TMDC material, significantly enhances the overall performance of the SPR sensor. The influence of various 2D layers is examined, and compared to the conventional SPR sensor, with the sensitivity gains being 1.60% with graphene, 5.89% with MoS_2, 7.5% with $MoSe_2$, 7.5% with WSe_2, and 8.55% with WS_2. Similar enhancements are seen in the FOM and DA.

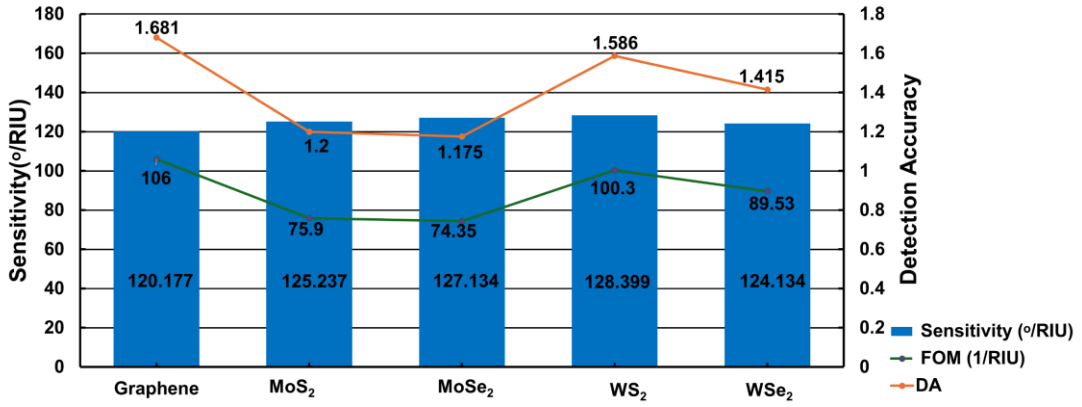

Fig. 5.4 Performance parameters of 2D material over Ag based SPR structure

This outcome highlights the exceptional sensing capabilities of TMDC material when integrated into the SPR setup, outperforming graphene in terms of sensitivity. Such findings emphasize the significant potential of TMDC material as a highly effective and sensitive material for sensing applications, promising exciting opportunities for advancements in sensing technologies and related fields. Expanding on this approach, the study has been broadened to incorporate heterostructure of Wurtzite nitride semiconductor and TMDC into Ag based SPR structure.

5.3.1 Performance of silver based SPR structure using GaN-TMDC

In this section, the GaN-TMDC heterostructure is integrated between the metal layer and sensing medium. Figure 5.5 illustrates the comparative SPR intensity curve for different heterostructures of GaN-TMDC, such as GaN-$MoSe_2$, GaN-MoS_2, GaN-WSe_2, and GaN-WS_2, where the refractive index (RI) of the sensing medium varies from 1.32919 (RIU) to 1.345 (RIU). The SPR curve depicts the relationship between reflectance, a dimensionless quantity, and the incident angle in degree for TMDC material over conventional Ag based SPR sensor, shown in Fig. 5.5, as discussed in our earlier study [150]. From Fig. 5.5, it is evident that the heterostructure GaN-WS_2 had sharp SPR curve as compared to other heterostructure. The sharpness of the SPR response in this sensor holds significance as it underscores the enhanced detection capabilities for biomolecular interactions. To further investigate the impact of heterostructures on the SPR sensor's performance, various performance parameters including Sensitivity, DA, and FOM have been computed for different GaN-TMDC based heterostructures, as illustrated in Table 5.2.

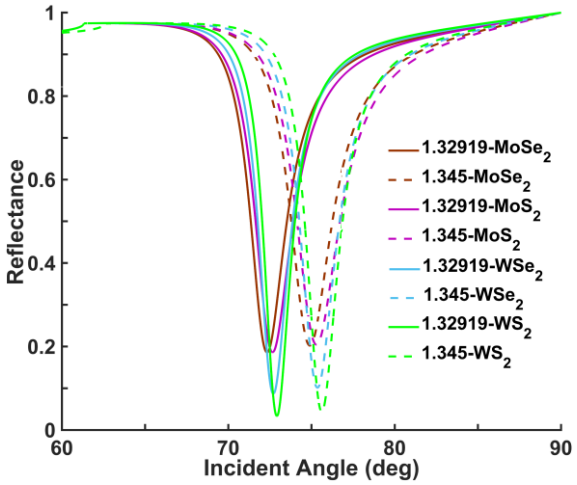

Fig. 5.5 SPR curves for heterostructures of GaN-TMDC on Ag-based SPR

Table 5.2 Performance parameters for GaN-TMDC Heterostructures

Structure	**Thickness (m)**	$\Delta\theta_R$ (°)	**Sensitivity (°/RIU)**	**DA**	**FOM (RIU^{-1})**
BK7-Ag-GaN-TMDC-sensing medium	Ag=55nm,GaN=5nm, MoS_2=0.65nm	2.57	162.55	0.8	52.6
	Ag=55nm,GaN=5nm, $MoSe_2$=0.7nm	2.64	166.98	0.8	51.53
	Ag=55nm,GaN=5nm, WSe_2=0.7nm	2.65	167.61	1.0	64.22
	Ag=55nm,GaN=5nm, WS_2=0.8nm	2.95	186.59	1.1	70.14

Table 5.2 shows values of the resonance angle shift due to change in refractive index after the biomolecular interaction for different heterostructures under investigation. Notably, GaN-WS_2 heterostructure based SPR sensor exhibits maximum shift. The outcomes of the study in table 5.2 suggest that, in terms of the performance parameters, the heterostructure GaN-WS_2 has a more significant impact on SPR sensor performance compared to other GaN-TMDC heterostructures. In biosensing applications, the SPR sensor is used to immobilize typically a few nanometers thick ligands on the metal surface to capture the desired analyte. Therefore, it is crucial that the EF intensity, which penetrates the biological sample, requires sufficient strength to detect the analyte attached to the ligand. Also, higher EF intensity enhancement factor is beneficial for sensor's imaging sensitivity. The investigation further extended in the COMSOL Multiphysics environment to explore the EF intensity at the interface of the sensing medium, as illustrated in Fig. 5.6.

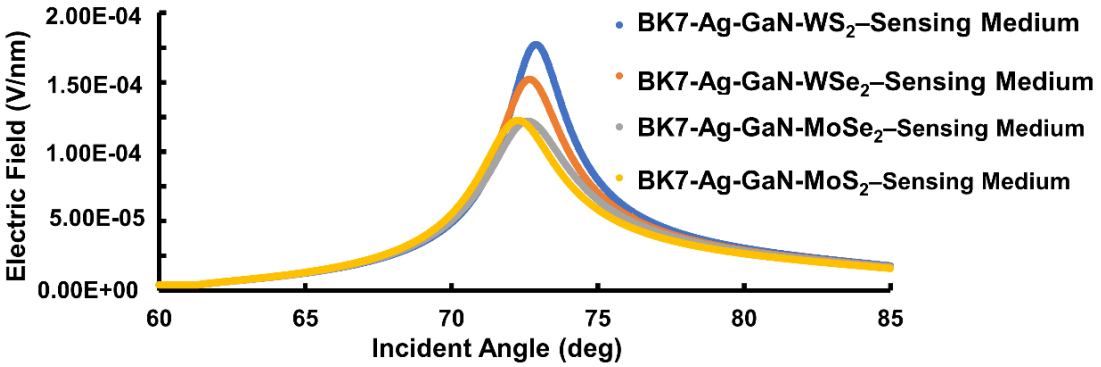

Fig. 5.6 Evanescent electric fielddue to GaN-TMDC layer

From Fig. 5.6, the maximum intensity of evanescent field has been noted as 1.74E-04 (V/nm) for GaN-WS_2, 1.23E-04 (V/nm) for GaN-WSe_2, 1.71E-04 (V/nm) for GaN-MoS_2, and 1.70E-04 (V/nm) for GaN-$MoSe_2$. It has been observed that the GaN-WS_2-based heterostructure exhibits maximum intensity at the sensing medium interface near the resonance angle of the proposed SPR structure. The propagation of electromagnetic waves in materials with complex refractive indices is attenuated with distance, primarily due to the imaginary component (i.e., the extinction coefficient), which governs this attenuation. Since WS_2 has a lower imaginary component compared to other TMDC materials, the results reveal that the GaN-WS_2 heterostructure produces the strongest evanescent field in the SPR sensor. 2D graphs in COMSOL Multiphysics environment are crucial for gaining a deep understanding of sensor behavior and validating models. Figure 5.7 visually represents 2D graphs, offering insights into the sensor section's behavior utilizing GaN-WS_2 heterostructure in SPR sensor design. This section of the SPR sensor is designed in COMSOL Multiphysics environment as rectangle geometry with width twice the wavelength of the incident light and height three times the wavelength of the incident light, as shown in Fig. 5.7. The height of the section under study is divided into layers of BK7 prism, Ag, GaN, WS_2, and sensing medium. As seen in Figure 5.7, EF reaches its maximum at the interface and then exponentially decreases in a direction perpendicular to the direction of propagation. This verifies the theoretical concept of EF concept discussed in chapter 2, section 2.3.2. As per the study strategy, various heterostructures involving AlN-TMDC materials are investigated in the following section.

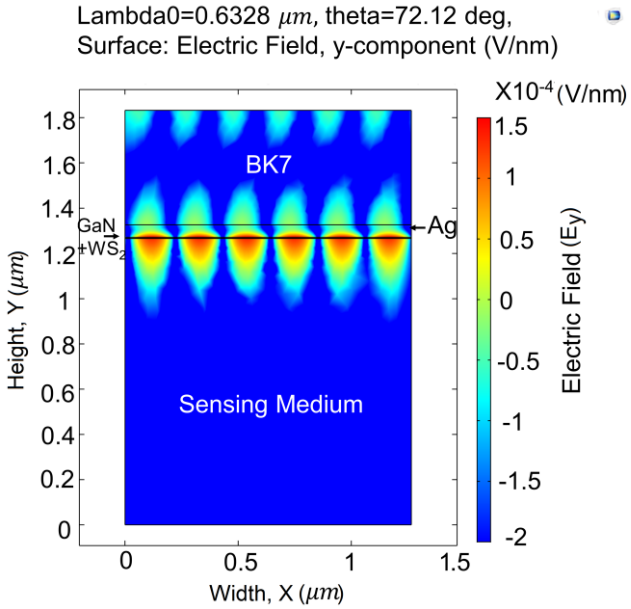

Fig. 5.7 2D Graphs of evanescent electric field intensity for BK7-Ag-GaN-WS_2-sensing medium (RI=1.32919)

5.3.2 Performance of silver based SPR structure using AlN-TMDC

This section focuses on the performance of an Ag based SPR structure utilizing AlN-TMDC. The examination specifically centers on heterostructures formed with AlN and various TMDC materials incorporated in the Ag coated BK7 prism SPR structure. Heterostructures, including AlN-MoS_2, AlN-$MoSe_2$, AlN-WSe_2, and AlN-WS_2 are considered in this study. The primary focus is the investigation of the SPR curve for the aforementioned structures, as illustrated in Fig. 5.8.

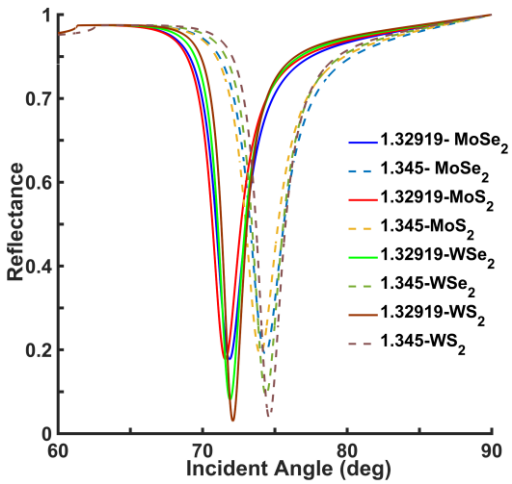

Fig. 5.8 SPR curves for heterostructures of AlN-TMDC on Ag based SPR

A comprehensive examination of Fig. 5.8 reveals similarities with Fig. 5.5. The AlN-WS_2 heterostructure based SPR sensor exhibits maximum depth and a notable shift in resonance angles. To extend the study, performance parameters for various heterostructures based on AlN-TMDC materials are calculated and presented in Table 5.3.

Table 5.3 Performance parameters for AlN-TMDC Heterostructures

Structure	Thickness (m)	$\Delta\theta_R$ (°)	Sensitivity (°/RIU)	DA	FOM (RIU^{-1})
BK7-Ag-AlN-TMDC-sensing medium	Ag=55nm,AlN=5nm, WSe_2=0.7nm	2.49	157.4953	1.0733	67.885
	Ag=55nm,AlN=5nm, WS_2=0.8nm	2.52	159.3928	1.2293	77.752
	Ag=55nm,AlN=5nm, MoS_2=0.65nm	2.42	153.0677	0.8832	55.864
	Ag=55nm,AlN=5nm, $MoSe_2$=0.7nm	2.48	156.8627	0.8641	54.656

Table 5.3 reveals a parallel outcome to Table 5.2; the integration of AlN-WS_2 demonstrates enhanced sensitivity, DA, and FOM performance in the SPR sensor compared to other studied heterostructures of this section. This enhancement underscores the critical role of material selection in optimizing sensor efficiency, particularly through the integration of AlN-TMDC based heterostructures. However, a comparison between Table 5.2 and Table 5.3 reveals that the incorporation of AlN-WS_2 yields a 15.9% lower enhancement than the GaN-WS_2 heterostructure. Furthermore, an investigation into the EF intensity concerning the incident angle is conducted for a more profound understanding of the impact of heterostructures under the study of this section, as shows in Fig. 5.9.

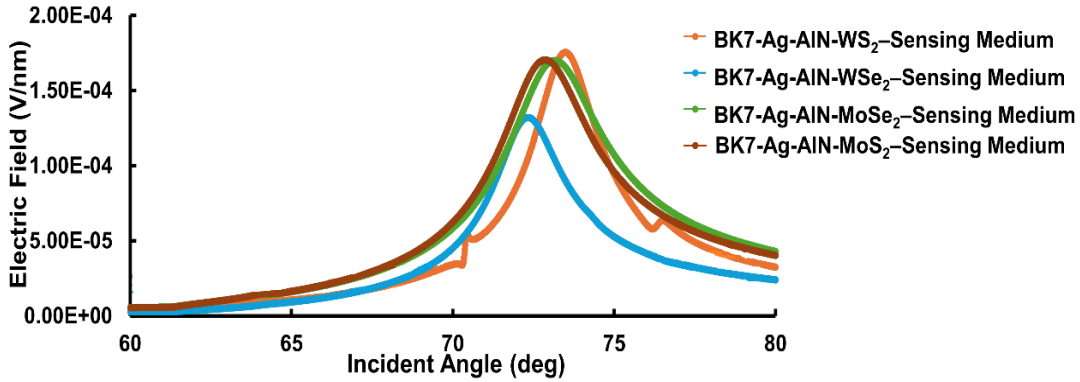

Fig. 5.9 Evanescent electric field due to AlN-TMDC layer

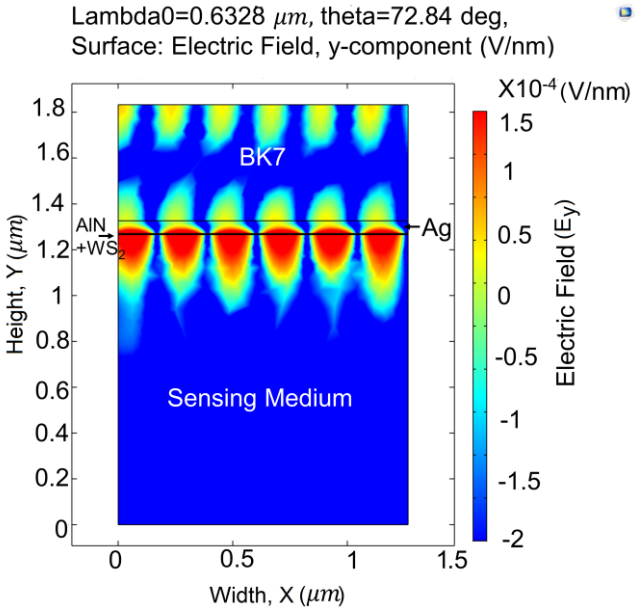

Fig. 5.10 2D Graphs of evanescent electric field intensity for BK7-Ag-AlN-WS_2-sensing medium (RI=1.32919)

As similar impact of GaN-TMDC heterostructure, peak in the intensity of EF seen to be near to resonance angle of proposed SPR sensor structure. The analysis of Fig. 5.9 shows that the maximum intensity of EF has been noted as 1.76E-04 (V/nm) for AlN-WS_2, 1.27E-04 (V/nm) for AlN-WSe_2, 1.71E-04 (V/nm) for AlN-MoS_2, and 1.70E-04 (V/nm) for AlN-$MoSe_2$. To delve deeper into the behavior of the SPR sensor structure incorporating the AlN-WS_2 heterostructure, an extensive analysis is performed using a 2D graph within the sensor section, as shown in Fig. 5.10. Figure 5.10 presents a graphical representation of the EF at the interface of the sensing medium in the section of the proposed structure. In the subsequent section of this study, diverse heterostructures based on InN-TMDC materials are explored.

5.3.3 Performance of silver based SPR structure using InN-TMDC

This section focuses on studying various heterostructures created by combining InN and TMDC materials on an Ag based BK7 SPR structure. The emphasis is specifically on analyzing the SPR curve concerning the incident angle, as depicted in Fig. 5.11 based on our prior investigation [151]. Heterostructures, including InN-MoS_2, InN-$MoSe_2$, InN-WSe_2, and InN-WS_2, are subjects of investigation.

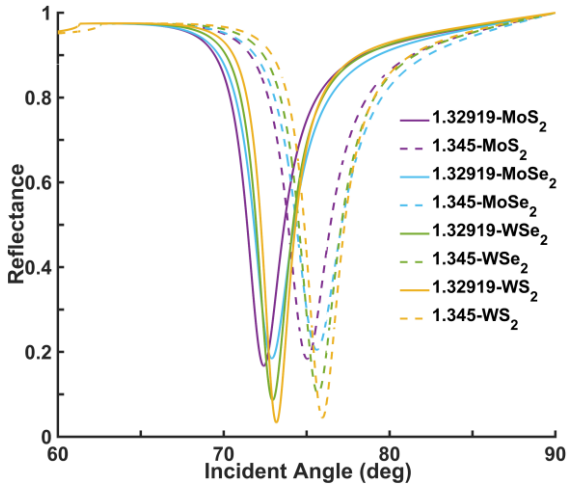

Fig. 5.11 SPR curve for heterostructures of InN-TMDC on Ag based SPR

The influence of incorporating InN-TMDC heterostructures exhibits similarities to the studies in the previous section, particularly in the SPR curve of Fig. 5.5 and Fig. 5.8. The investigation extends to the computation of performance parameters, as detailed in Table 5.4.

Table 5.4 Performance parameters for InN-TMDC Heterostructures

Structure	Thickness (m)	$\Delta\theta_R$(°)	Sensitivity (°/RIU)	DA	FOM (RIU^{-1})
BK7-Ag-InN-TMDC-sensing medium	Ag=55nm,InN=4nm,WSe_2=0.7nm	2.73	172.6755	0.9856	62.337
	Ag=55nm,InN=4nm, WS_2=0.8nm	2.78	175.8381	1.1347	71.77
	Ag=55nm,InN=4nm, MoS_2=0.65nm	2.62	165.7179	0.8479	50.158
	Ag=55nm,InN=4nm, $MoSe_2$=0.7nm	2.72	172.043	0.7930	53.630

The examination of Table 5.4 underscores the significance of the InN-WS_2 heterostructure compared to other heterostructures in the study of this section, highlighting its superior potential for enhancing sensor performance. Additionally, this observation is further corroborated by its distinct electric field characteristics. Furthermore, an in-depth investigation of the EF is conducted for various InN-TMDC heterostructures. Figure 5.12 illustrates the electric field's behavior concerning the incident angle at the sensor interface. The analysis of Fig. 5.12 reveals that the maximum intensity of EF is recorded as 1.73E-04 (V/nm) for InN-WS_2, 1.31E-04 (V/nm) for InN-WSe_2, 1.7E-04 (V/nm) for InN-MoS_2, and 1.69E-04 (V/nm) for InN-$MoSe_2$, showcasing a clear distinction in performance among the heterostructures.

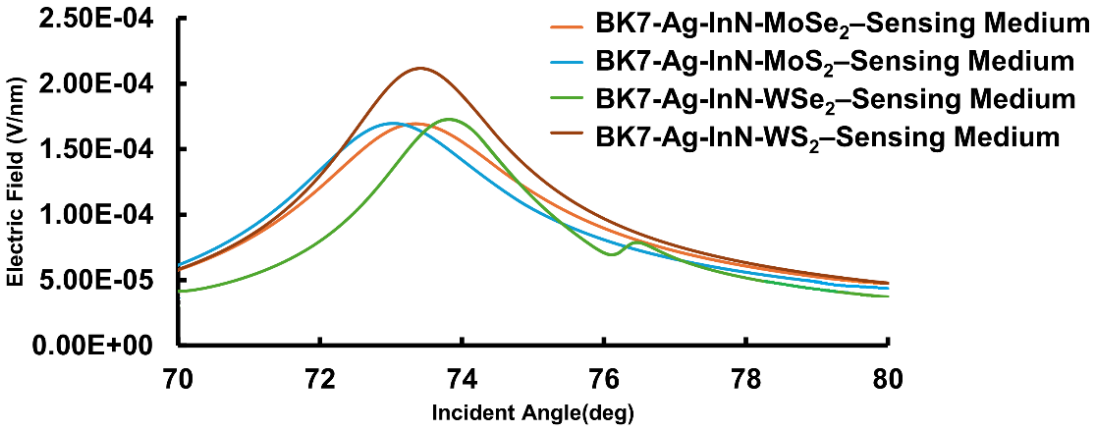

Fig. 5.12 Evanescent electric field due to InN-TMDC layer

To acquire a better understanding of the SPR sensor structure with the InN-WS_2 heterostructure, a significant study is carried out utilizing a 2D graph within the sensor section in COMSOL Multiphysics environment, as shown in Fig. 5.13.

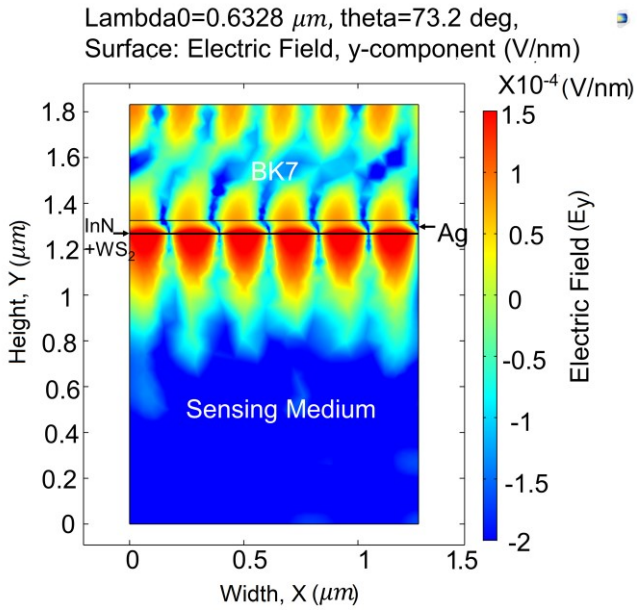

Fig. 5.13 2D Graphs of evanescent electric field intensity for BK7-Ag-InN-WS_2-sensing medium (RI=1.32919)

In summarizing this investigation, the study extends to assess the precise performance of the proposed sensor under varying sensing medium refractive indices. The resonance angle shift of the proposed SPR structure is accurately determined by systematically adjusting the refractive index within the range of 1.32919 (RIU) to 1.345 (RIU), with a step size of 0.001. This chosen refractive index range corresponds

to the optical characteristics of human hemoglobin in the visible spectrum [152]. Figure 5.14 portrays the sensor's response as a substantial shift in resonance angle, indicating an infinitesimally small change in the detecting refractive index following our previous research findings [148]. Remarkably, the InN-WS_2 heterostructure achieves the largest resonance angle shift. The optimal response from the proposed SPR sensor with InN-WS_2 is observed in the refractive index range of 1.372 (RIU) to 1.389 (RIU). Similarly, AlN-WS_2 provides the best response in the range of 1.387 (RIU) to 1.4 (RIU), whereas GaN-WS_2 exhibits the best response in the range of 1.38 (RIU) to 1.396 (RIU).

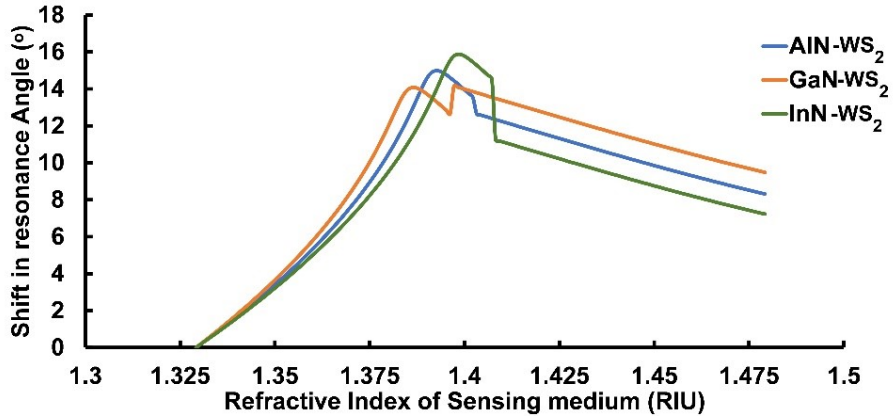

Fig. 5.14 Variation of shift in resonance angle w.r.t RI of sensing medium.

Recent research has shown experimental proof of integration heterostructure in SPR based on semiconductors and 2D materials with metals. For instance, cadmium sulfide (CdS) quantum dots composited with graphene oxide functionalized with IgM for dengue virus detection have been developed [153]. Silicon carbide (SiC) is ideal for sensing in aqueous media, and when combined with 2D materials like graphene or TMDCs, SPR sensors show improved sensitivity [154]. These examples demonstrate how combining semiconductors and 2D materials with metals enables the development of high-performance SPR sensors, advancing their applications in diverse fields.

5.4 Summary

This investigation thoroughly assessed the performance parameters of semiconductor-TMDC heterostructures based SPR sensor using the angular

interrogation technique. Compared to a conventional 3-layer configuration, the SPR sensor's sensitivity increases by 17.64%, 23%, and 25.9%, with the inclusion of AlN, GaN, and InN, over Ag, respectively. A similar enhancement in sensitivity is observed with the incorporation of 2D materials over Ag, as illustrated in Figure 5.4. The analysis reveals that the wurtzite nitride layer contributes more significantly to sensitivity improvement than 2D materials over Ag. Among the wurtzite nitrides, InN provides 8.02% more sensitivity than AlN and 2.7% more sensitivity than GaN compared to the 3-layer SPR structure. However, AlN exhibits superior DA and FOM values compared to other wurtzite nitride semiconductors.

To further enhance performance, a heterostructure is introduced between the metallic layer and sensing layer. Among the various heterostructures examined, the wurtzite nitride-WS_2-based SPR sensor performs exceptionally well. This heightened performance is indicated by improved sensitivity, significant DA, a noteworthy FOM, and EF intensity at the sensor's interface. While GaN-WS_2 demonstrates the highest sensitivity value, AlN-WS_2 exhibits a much better response in terms of DA, FOM, and electric field intensity values. Figure 5.14 illustrates additional findings, indicating that the GaN-WS_2, AlN-WS_2, and InN-WS_2 heterostructures yield the highest sensitivity values at 250.18 (^{o}/RIU), 239.83 (^{o}/RIU), and 232.0588 (^{o}/RIU), respectively, for a sensing medium refractive index of 1.3842 (RIU), 1.3912 (RIU), and 1.3972 (RIU). This study also highlights that the heterostructure with WS_2, in contrast to other TMDC materials, offers the highest field enhancement factor at the sensor interface, resulting in improved overall performance of the SPR sensor..

Building on these findings, the sensor's performance is anticipated to improve further with the incorporation of a bimetallic layer. This approach is expected to optimize the balance between sensitivity, detection accuracy, and FOM while addressing limitations such as the sharpness of the SPR curve and the evanescent field intensity. The exploration of bimetallic layers to improve the SPR sensor's capabilities will be discussed in the subsequent chapters.

CHAPTER 6

PERFORMANCE OF SPR SENSOR IN THE PRESENCE OF VARIOUS HETEROSTRUCTURES ON THE SINGLE/ BIMETAL SURFACE

The functionality of a single/bimetal based SPR sensor has been explored. A 2D heterostructure, comprising AlN and TMDC, was strategically placed on an optimized bimetallic surface of Ag and Au, enhancing sensor stability and responsiveness. The high-index AlN layer increased sensitivity, while TMDC material boosted the adsorption of target biological molecules, while protective layers prevented oxidation. The research specifically focused on the meticulous design of bimetallic structures within SPR sensor configurations, leveraging the TMM through MATLAB and the COMSOL Multiphysics environment software.

Chapter Built Upon

- **T. M. S. Ashrafi** and G. Mohanty, "Single and bimetal-based surface plasmon resonance sensor using AlN-TMDC heterostructure: a comparison study," Opt. Quantum. Electron. **55**(1), 59 (2023).

Chapter 6

6.1 Introduction

The findings from Chapter 4 show that SPR based sensors using Ag metal exhibit a minimal reflection (Rmin) value in the SPR curve. However, they are subject to oxidation, which makes them weak. On the contrary, sensors that use Au have higher sensitivity but lower accuracy due to the inability of the Rmin value to reach the minimum, as seen in the previous case. According to study of 2002, Ag-Au bimetallic layers provide a significant resonance angle shift in response to variations in the refractive index (RI) with minimum Rmin. This property increases the signal-to-noise ratio of SPR devices. Furthermore, the study shows that outer Au layer, which is chemically inert, serves as a barrier, shielding the inner Ag layer from oxidation [155]. Moreover, a study in 2019 found that bimetallic sensor chips had a significant reduction in FWHM values, which were nearly six times lower than those of only Au-based sensor chips. This reduction helped with significant improvement in DA [156]. Past studies have proven that using Au and Ag nanoparticle multilayer films in the construction of plasmonic sensors produces encouraging outcomes. These sensors demonstrate a strong ability to detect binding events and are versatile, working well in both bulk and surface biosensing applications. Moreover, their simplicity and cost efficiency provide them attractive substitutes for complex sensing techniques [157,158]. Curiously, the concept of integrating Ag-Au bimetallic layers into sensor design has attracted attention as a means to enhance sensor capabilities.

This chapter covers the study of single and bimetallic layers based on SPR sensor with a heterostructure combination of AlN and 2D material. Finally, all of the calculated performance metrics, including sensitivity, DA, FOM, and electric field enhancement factor, are analyzed and compared.

6.2 Computational Methodology

The proposed SPR sensor design works according to Kretschmann-Reather configuration with angular interrogation, utilizing a transverse magnetic wave with a

wavelength of 632.8 nm. In standard bimetallic SPR structures, the Au film covering the Ag film works as a barrier, preventing oxidation of the underlying Ag layer. The 2021 study's conclusive results show that the proposed Au/Ag/Si/Graphene sensor has a significantly higher sensitivity than the bare gold sensor [75]. Following the principles of the Kretschmann configuration, a novel SPR structure is precisely designed. The sequential arrangement comprises a BK7 glass prism as the foundational substrate, followed by a single or bimetal layer, TMDC, and the sensing medium. This design strategy includes the combination of different noble metals, notably Ag and Au, both individually and in combinations. In the present study, the SPR structure is designed by placing the different materials in the following chronological order i.e., BK7 glass prism, single/bimetal layer, AlN, TMDC, and sensing medium. The conceptual framework for this proposed SPR structure is visually captured in Fig. 6.1 from our previous work on this topic [159].

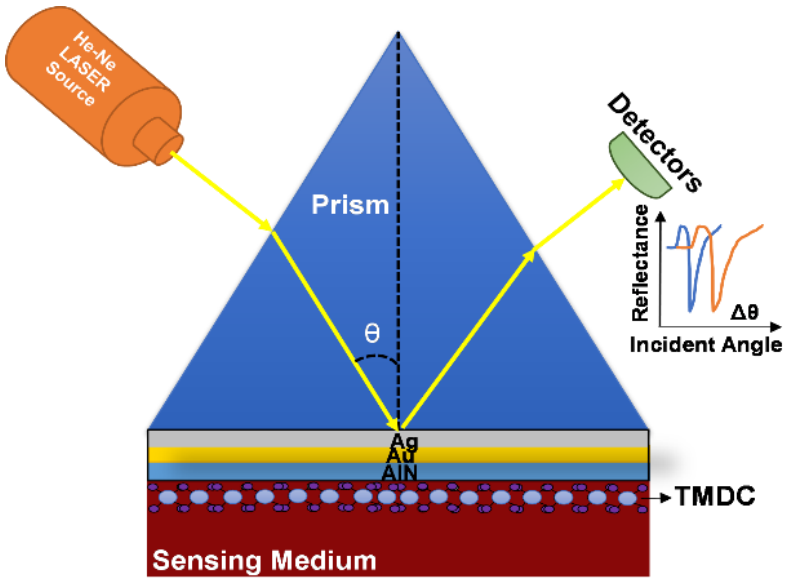

Fig. 6.1 The conceptual framework for proposed SPR structure

To comprehensively evaluate the performance parameters intrinsic to this structure, a precise mathematical model is applied. The TMM is carefully applied for mathematical modelling in order to examine the SPR structure's output response, especially when it is structured in multilayered N-layers, as is covered in Chapter 3. This

methodology thus offers a robust foundation for exploring and understanding the intricate interplay of materials and layers within the SPR context, with the TMM providing a rigorous analytical tool for insights into its performance dynamics, as studied in chapter 3. In the N-layer system, the reflectance can be computed using the expression discussed in chapter 3. The expression of R is:

$$R = \left| \frac{(M_{11} + M_{12} q_N) q_1 - (M_{21} + M_{22} q_N)}{(M_{11} + M_{12} q_N) q_1 + (M_{21} + M_{22} q_N)} \right|^2 \tag{6.1}$$

Additionally, the electric field intensity (E_{Π}) and magnetic field ($H_{\perp}$) are calculated as follows:

$$H_{\perp} = \frac{2q_1}{(M_{11} + M_{12} q_N) q_1 + (M_{21} + M_{22} q_N)} \tag{6.2}$$

$$E_{\Pi} = \left(\frac{\mu_N n_1}{\mu_1 n_N} \right) H_{\perp} \tag{6.3}$$

In this study, Table 6.1 presents the RIs of the materials at a wavelength of 632.8 nm.

Table 6.1 The refractive indices (RI) of the materials at a wavelength of 632.8 nm.

Materials	**Refractive index (RIU)**
BK7	1.5151+0i [34]
Ag	0.056253 + 4.2760i [38]
Au	0.18377 + i3.4313 [38]
AlN	2.1496+0i [59]
WSe_2	5.2302 + 0.50229i [52]
WS_2	5.0646 + 0.23623i [52]
MoS_2	4.9168 + 1.0554i [52]
$MoSe_2$	5.2069 + 0.92551i [52]

To gauge the sensitivity of the proposed sensor structure, a range of RI values for the sensing medium is investigated, spanning from 1.32919 to 1.345. Notably, the chosen range of RI corresponds to that of human hemoglobin in the visible region, a relevant benchmark for biomedical applications [152].

6.3 Results and Discussion

This section is structured systematically into single metal-based SPR sensors, bimetallic metal-based SPR sensors, and explores the effects of AlN layers in both single and bimetallic SPR sensors, as well as the impact of heterostructure AlN-TMDC on bimetallic SPR sensors.

6.3.1 Single Metal-based SPR sensor

According to the fundamental principle of energy conservation, the maximal energy content delivered by incident photons interacts with a greater number of electrons at the interface, leading to SPP, the resulting reflecting intensity of light reduction. As a consequence, the most favourable thickness would correspond to the point of minimum reflectance, resulting in an optimal scenario with the highest achievable EF at the interface of the metal and dielectric components. In this investigation, the optimization of various layer thicknesses is based on the pursuit of minimal reflectance values, simplified by the TMM, and executed through the MATLAB software. Notably, Ag is optimized at a thickness of 55 nm, whereas Au is optimized at a thickness of 47 nm. The performance parameters are computed and tabulated below Table 6.2:

Table 6.2 Performance parameters of the single metallic layer in SPR

Thickness of Ag (nm)	Thickness of Au (nm)	Sensing Medium RI	Minimum Reflectance	$\Delta\theta_R$ (°)	S (°/RIU)	DA	FOM (RIU^{-1})
55	0	1.32919 1.345	0.000219 0.000147	67.39 69.26	118.2796	2.174	137.534
0	47	1.32919 1.345	0.0003657 0.002277	71.65 74.03	150.5376	0.425	26.881

6.3.2 Bimetallic layered based SPR sensor

The thickness of bimetallic layers is computed based on minimal reflectance values as reflected. To study the impact of different metals thickness in bimetallic structure, the minimal reflectance values, sensitivity and FOM are calculated and tabulated in Table 6.3. In Table 6.3, scenarios requiring a combination of bimetallic

structure, the combination of 46 nm-thick Ag and 4 nm-thick Au emerge as the most advantageous with Rmin value, delivering superior results in terms of DA and FOM.

Table 6.3 Performance parameters of the bimetallic layers in SPR

Thickness of Ag (nm)	Thickness of Au (nm)	Sensing Medium RI	Minimum Reflectance	$\Delta\theta_R$ (°)	S (°/RIU)	DA	FOM (RIU^{-1})
46	4	1.32919	0.00007	68.41	125.2372	1.185	74.99
		1.345	3.30E-05	70.29			
43	6	1.32919	0.00014	68.82	127.7672	0.985	62.325
		1.345	0.00028	70.74			
41	7	1.32919	8.21E-05	69.01	129.0323	0.89	56.59
		1.345	1.96E-05	70.95			

The SPR curve illustrates the relationship between the incident angle, measured in degrees, and reflectance, a dimensionless ratio representing the intensity of reflected light compared to incident light. Figure 6.2 depicts the SPR curves for single metals such as Ag, Au, and bimetallic Ag-Au without the heterostructure of AlN-TMDC as discussed in our previous work [159].

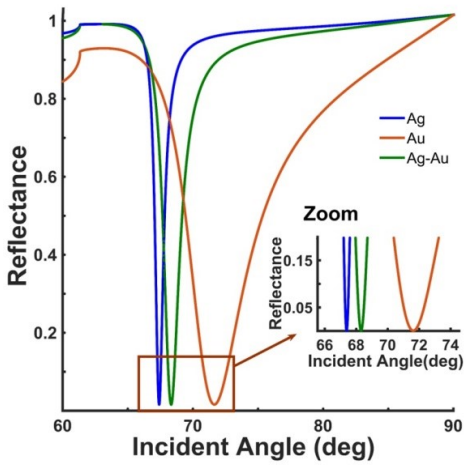

Fig. 6.2 SPR intensity curve for single and bimetal-based structure with sensing medium RI 1.32919

The SPR dip in the Ag-Au bimetallic SPR structure is clearly visible, occupying a position intermediate to the response profiles of the monometallic structures. Notably, the

Rmin of the Ag monolayer is 0.0002191, whereas the Au monolayer has a value of 0.0003657 for sensing medium with RI 1.32919 (RIU). In contrast, with the same RI of sensing medium, the bimetallic combination has an exceptionally low Rmin of 0.00007547. Clearly, the bimetallic combination has an incredibly low Rmin value of the order of 10^{-5}, compared to the monometallic configuration's value of around 10^{-4}.

6.3.3 Impact of Aluminium Nitride (AlN) layer in single/ bimetallic layer SPR sensor

In order to get better performance, the AlN layer is sandwiched between the metal layer and the sensing medium. As the extinction coefficient of AlN iszero at 6328 Å wavelength of light, the strength of the EF will not be attenuated by this layer. The optimal thickness of AlN has been determined to be 5 nm for all noble metals and their combinations under consideration in this study. The impact of AlN is studied in the four-layer structure, where it is coated on the metallic layer of the SPR sensor and sensing medium RI changes from 1.32919 (RIU) to 1.345 (RIU). Figure 6.3 shows the impact of AlN layer for SPR sensor [159].

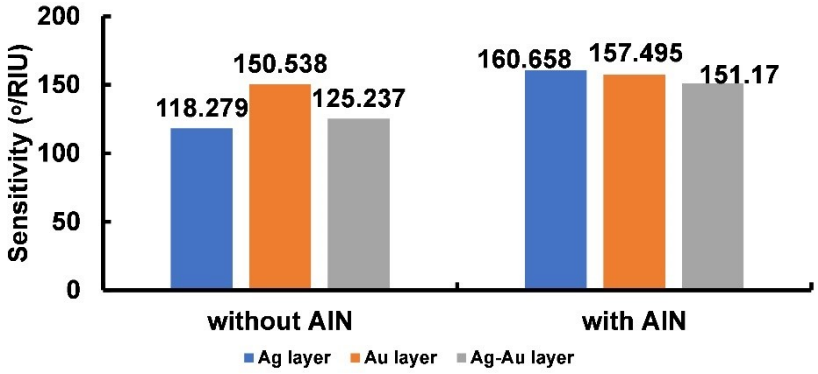

Fig. 6.3 Sensitivity comparison between the three-layer structure and four-layer structure

The results show that when AlN is applied to the single metal layer of Ag and Au, it leads to a substantial 35.82% improvement in Ag and a 4.62% enhancement in Au. Furthermore, when AlN is utilized in the bimetallic combination of Ag-Au, it still significantly improves sensitivity by 20.70%, as depicted in Fig. 6.3. On average, AlN enhances sensitivity across these various scenarios by approximately 19.10%. This

suggests that AlN is a valuable addition to SPR sensor designs, as it consistently boosts their ability to identify shift in the RI of the surrounding medium.

6.3.4 Impact of heterostructure AlN-TMDC on the bimetallic based SPR sensor

Next, 2D materials such as TMDC are incorporated into the previous SPR structure. The impact of AlN-TMDC heterostructure on the over-all performance of the SPR sensor has been studied and analyzed. This study considered TMDC materials, such as WSe_2, WS_2, $MoSe_2$, and MoS_2 with optimal thickness 0.7, 0.8, 0.7, and 0.65 nm, respectively. The sensitivity of the proposed structure is computed by shifting the RI of the sensing medium from 1.32919 (RIU) to 1.345 (RIU). The SPR dip of the bimetallic structure with different heterostructure between AlN- TMDC materials at the sensing medium, ranging refractive indices from 1.32919 (RIU) to 1.345 (RIU), is illustrated in Fig. 6.4 [159].

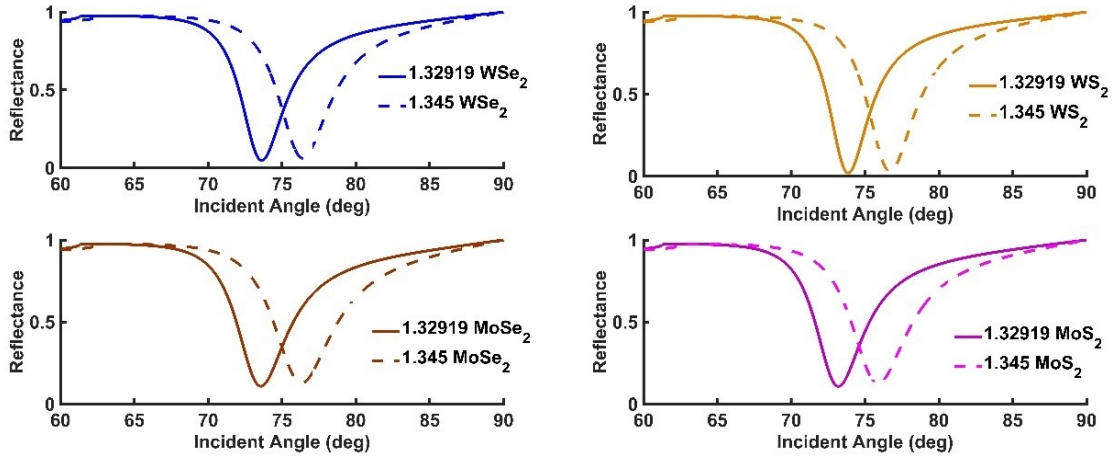

Fig. 6.4 SPR dip shifts for different TMDC material-based structures

The calculated Rmin and θ_R for the proposed structure of sensor, consisting of a BK7 prism coated with a bimetallic structure of Ag-Au and a TMDC layer, are tabulated in Table 6.4 below for the sensing medium. For the proposed structure, performance parameters including sensitivity, DA, and FOM have been systematically computed and are tabulated in Table 6.4.

Table 6.4 Performance parameters of proposed heterostructure based SPR sensor

Ag layer thickness (nm)	Au layer thickness (nm)	AlN layer thickness (nm)	TMDC layer thickness (nm)	RI of Sensing medium	Rmin value	θ_R (°)	Δθ (°)	S (°/RIU)	FWHM (°)	DA	FOM (RIU^{-1})
46	4	5	WSe_2=0.7	1.32919	0.0466	73.62	3	176	4.2	0.66	41.97
				1.345	0.0614	76.4					
46	4	5	WS_2=0.8	1.32919	0.0179	73.86	3	179	3.9	0.73	46.13
				1.345	0.0287	76.69					
46	4	5	$MoSe_2$=0.65	1.32919	0.1068	73.2	3	170	4.6	0.58	36.61
				1.345	0.1245	75.88					
46	4	5	MoS_2=0.65	1.32919	0.108	73.56	3	175	4.9	0.57	35.99
				1.345	0.1279	76.32					

Table 6.4 presents the observed shift in resonance angles for various TMDC materials, including WSe_2, WS_2, $MoSe_2$, and MoS_2 [159]. The calculated shifts are as follows: 2.78° for WSe_2, 2.83° for WS_2, 2.68° for $MoSe_2$, and 2.76° for MoS_2. The analysis of both Fig. 6.4 and Table 6.4 reveals that WS_2 yields the lowest reflectance along with the most significant resonance angle shift, measured at 2.13°.

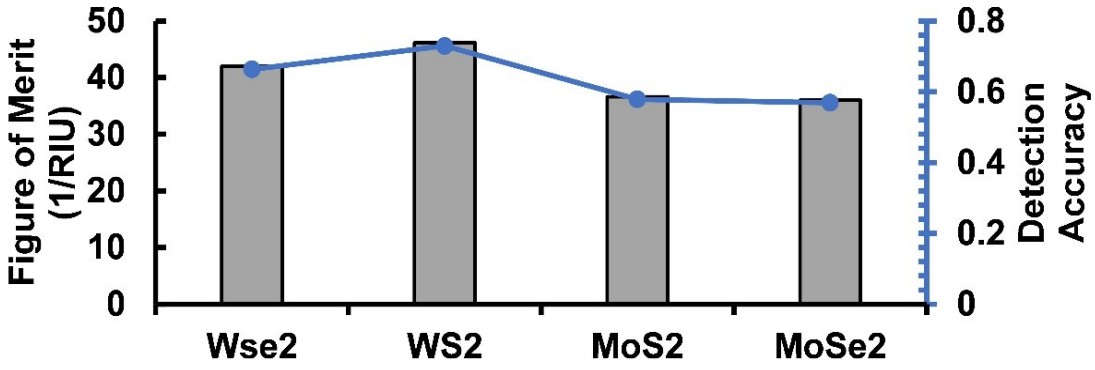

Fig. 6.5 Comparison values of FOM and DA for AlN-TMDC based SPR structures

The term DA a dimensionless quantity, in this context, denotes accurately and precisely the Rmin in the SPR intensity curve are tabulated in Table 6.4. A narrow SPR curve produces a higher DA. Simultaneously, FOM is a comprehensive parameter to study the performance of SPR sensors, measured with unit RIU^{-1}. Contrary to common perception, studies show that increasing sensitivity does not always result in a higher FOM for SPR sensors, as shown in various research studies [160]. This phenomenon can be explained by the SPR curve broadening, which increases FWHM value and subsequently lowers the FOM value. Figure 6.5 shows the comparison results of FOM and DA for all structures. It is observed that both FOM and DA are maximum for the AlN-WS_2 heterostructure-based SPR structure in comparison to other heterostructure under study. Notably, the results reveal that both the FOM and DA are maximized for the SPR structure incorporating the AlN-WS_2 heterostructure. Interestingly, the same structure also exhibits the highest sensitivity, as detailed in Table 6.4.

Furthermore, an in-depth analysis of the EF at the interface of the sensing layer for the proposed SPR structure with various AlN-TMDC heterostructures has been

conducted. Given that the EF exhibits exponential decay into the sample medium, it is crucial to extend the sensing region for monitoring biomolecular interactions effectively. Consequently, a robust EF at the sensor surface plays a pivotal role in achieving high sensitivity. Figure 6.6 presents a visualization of the computed electric fields plotted against the incidence angle.

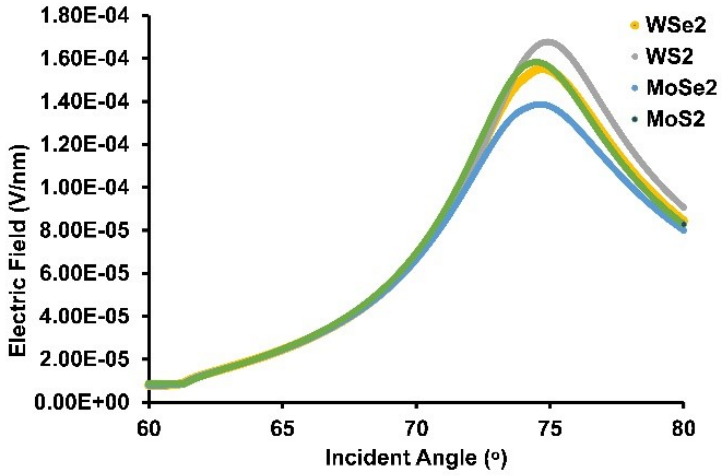

Fig. 6.6 Electric field of proposed structure with respect to incident angle

It is noteworthy from Fig. 6.6 that the intensity of the EF attains its maximum value precisely when the reflected intensity of light reaches its dip. Remarkably, the AlN-WS_2 heterostructure demonstrates the highest observed maximum electric field with a value of 1.68E-04(V/nm). This strong electric field plays a pivotal role in achieving maximum sensitivity, as corroborated in Table 6.4. It underscores the significance of the AlN-WS_2 heterostructure in creating a powerful EF critical for enhancing the sensor's sensitivity in biomolecular interaction monitoring.

To substantiate the presence of this maximum EF at the sensing interface, finite element analysis (FEA) has been employed. The wave optics module of COMSOL Multiphysics serves as a valuable tool for visualizing the electric field. Figure 6.7 provides a comprehensive illustration of the electric field enhancement at the interface, specifically focusing on the AlN-WS_2 heterostructure-based Ag-Au SPR structure. The analysis unequivocally confirms that the electric field intensity reaches its peak precisely

at the interface, occurring at the incident angle of 73.86 degrees. This empirical verification underscores the precision and significance of the AlN-WS_2 heterostructure in generating the strongest EF at the sensing interface, a key factor contributing to the maximized sensitivity observed in this SPR structure.

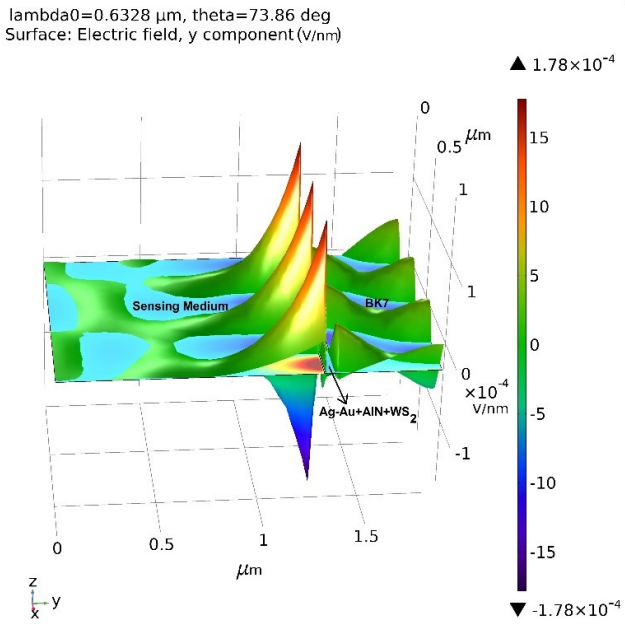

Fig. 6.7 Evanescent field at sensing interface for AlN-WS_2 heterostructure based SPR configuration

Table 6.5 compares the performance of the proposed sensor with previously documented attempts, highlighting its competitive edge and advancements in SPR sensor technology. It is clearly seen that the sensitivity is significantly enhanced by incorporating the AlN–WS_2 heterostructure on a bimetallic SPR configuration. However, a detailed analysis of the FOM values reveals limitations compared to other configurations. Upon comparing the data from Table 5.3 (Chapter 5) with Tables 6.4 and 6.5, it becomes clear that the inclusion of the AlN–WS_2 heterostructure in the bimetallic layer improves the sensor's sensitivity. However, other performance parameters such as DA and FOM are lower than those in the single-metallic configuration with the AlN–WS_2 heterostructure. Similar results are observed in terms of EF intensity when comparing Fig. 5.9 and Fig. 6.7; bimetallic based configuration shows less intensity in terms of EF wave than the single metal with AlN–WS_2 based configuration.

Table 6.5 Performance parameters comparison with literature

Metal	Wavelength	Structure	S (°/RIU)	FOM (RIU^{-1})
Ag	633 nm	BK7/Ag/WS_2/Analyte [69]	125.33	67.745
Ag	633 nm	BK7/Ag/Graphene/Analyte [62]	97.76	–
Au	633 nm	BK7/Au/WS_2/Analyte [69]	138.33	38.70
Au	632.8 nm	BK7/Au/MoS_2/Analyte [70]	174.15	27.86
Au	633 nm	BK7/Au/Si/graphene/Analyte [4]	134.60	–
Ag-Au	633 nm	BK7/Ag/Au/ Graphene/ Analyte [69]	125	55.55
Ag-Au	633 nm	BK7/Ag/Au/ WS_2/ Analyte [69]	132	49.07
Ag-Au	633 nm	BK7/Ag/Au/WS_2/Graphene/Analyte [69]	135	39.91
Ag-Au	632.8 nm	BK7/Ag/Au/AlN/WS_2/Analyte	179.00	46.134

6.4 Summary

The study investigates the impact of bimetallic layers on the performance of SPR sensors, with a focus on heterostructures formed by AlN and TMDC materials. Layer thicknesses were optimized using the Transfer Matrix Method (TMM) in MATLAB. The findings emphasize the advantages of bimetallic architecture, specifically the Ag-Au combination, optimized at 46 nm and 4 nm for Ag and Au, respectively. This configuration yielded a sensitivity of 125.2372 °/RIU, which is intermediate compared to single-metal configurations - lower than Au (150 °/RIU) but slightly higher than Ag (118 °/RIU). Sensitivity improved by 19.10% with the addition of an AlN layer, paving the way for further enhancements using AlN-TMDC heterostructures. These heterostructures maximize resonance angle shifts while reducing Rmin values. Among the TMDC materials studied, WS_2 proved most effective, with the AlN-WS_2 heterostructure achieving a sensitivity of 179 °/RIU, DA of 0.73, and FOM of 46.134 RIU^{-1}. Also, the electric field intensity at the sensor surface shows a value of 1.68 E-04 (V/nm), which is lower than the 1.76 E-04 (V/nm) observed in single-metal structures. Thus, the bimetallic SPR setups although improve the sensitivity but are less effective in DA, FOM, and EF intensity at the sensor surface in comparison to Ag based SPR sensor. Because the single

metal (Specifically for Ag) based SPR configurations achieve balanced performance across all parameters, including a sensitivity of 159.3928 (°/RIU), a DA value of 1.2293, and an FOM of 77.752 RIU^{-1} with reference to Table 5.3. This makes single metal based SPR configuration promising rather than bimetal based configuration. Building on these insights, the next chapter is dedicated for practical application such as detection of honey adulteration using SPR sensor with a focus on all key performance parameters such as sensitivity, DA, FOM, and EF intensity at the surface interface.

CHAPTER 7

APPLICATION: DETECTION OF HONEY ADULTERATION USING III-V NITRIDE AND TUNGSTEN DISULFIDE BASED SPR SENSOR

This study investigates the use of a wurtzite nitride semiconductor material, in conjunction with tungsten disulfide (WS_2), in a surface plasmon resonance (SPR) sensor design for detecting honey adulteration. The sensor is made up of a BK7 glass prism with a silver-coated base and a heterostructure of GaN-WS_2, AlN-WS_2, and InN-WS_2. By intentionally introducing various sugar concentrations into honey to mimic adulteration, the study utilizes angle interrogation in a computational environment to analyze sensor performance. The InN-WS_2 based SPR sensor outperforms alternative structures and offers potential for highly sensitive detection of honey adulteration, benefiting the biomedical and food industries.

Chapter Built Upon

- **T. M. S. Ashrafi** and G. Mohanty, "Ultra-sensitive plasmonic sensor for detecting honey adulteration with III-V Nitride and Tungsten Disulfide," Sens. Imaging **25**, 19 (2024).

Chapter 7

7.1 Introduction

The global population's rapid expansion has spurred a heightened demand for high-quality food products. Honey, a natural sweet substance produced by bees, is admired for its scarcity and esteemed medicinal properties [161]. However, the issue of honey adulteration looms large due to its economic value [162]. This poses a significant concern as honey is a staple in human diets, acclaimed for its natural sweetness composed mainly of glucose and fructose. Furthermore, honey is known for its impressive profile of 181 health-promoting phytochemicals and antioxidants, making it a potent preventive measure against various diseases [163]. It also finds utility in wound healing, diabetes management, and mitigating cardiovascular, neurological, and gastrointestinal issues [164]. Honey typically comprises 16% to 20% water, 76% to 80% glucose and fructose, and contains less than 5% sucrose [165]. According to Indian Standards and FSS rules, the fructose-to-glucose (F/G) ratio should ideally range between 0.95 and 1.0, with sucrose content not exceeding 5% by mass. Elevated sucrose levels may indicate deliberate adulteration, a practice with known detrimental health effects.

Recognizing the gravity of sugar adulteration and its potential health risks, previous research has highlighted the significance of identifying such adulteration [166,167]. Detection of honey adulteration is for ensuring product quality and authenticity. Several specific methods are utilized to detect honey adulteration, ensuring the accuracy and reliability of assessments. These methods encompass various scientific approaches, including sugar composition analysis, moisture content measurement, spectroscopy techniques [168–170], microscopic analysis [171], stable isotope analysis [172], gas/ liquid chromatography [173], DNA-based techniques [174], nuclear magnetic resonance (NMR) spectroscopy [175], enzyme analysis, and sensor-based technologies [176]. While each method offers valuable insights into specific aspects of honey authenticity, relying on a single technique is insufficient for obtaining a comprehensive and accurate result.

Chapter 7

Comparing the outcome of Chapter 6 and Chapter 5, it is clear that the sensitivity of the SPR sensor increases when a bimetallic layer is added. However, this improvement comes at the cost of a decrease in the FOM value. Hence, the sensor's performance with the bimetallic structure is not as remarkable as expected. A number of studies have shown the effectiveness of SPR-based fiber optic sensors in detecting honey adulteration [177,178]. TMDC materials are significant due to their varied features, including a layered structure, adjustable band gap, and catalytic activity. These qualities make them very promising for sensor applications. Some studies have specifically investigated the use of WS_2 for sensing sugar concentrations [179,180]. Agrawal et al. have successfully shown the effective interaction between functionalized WS_2 and sucrose [181]. In addition, Yadav et al. introduced a fiber optic plasmonic sensor that uses Ag and Ag-coated graphene oxide (GO) to detect the presence of glucose and fructose in honey as a form of adulteration [182].

Previous chapters have shown that incorporating high refractive index semiconductors between metal and 2D materials can improve the performance of SPR-based sensors. This integration helps shield against oxidation and enhances sensor sensitivity. Hence, in order to develop a highly responsive and consistent SPR sensor for detecting honey adulteration, it is necessary to do more research on the combination of heterostructures, namely III-V nitride and TMDC. The current study examines potential of an SPR sensor based on a wurtzite nitride-WS_2 heterostructure for detecting sugar concentrations in honey. The SPR sensor is composed of a five-layer structure arranged in a specific sequence: a BK7 prism, Ag, wurtzite nitride semiconductors, WS_2, and a sensing medium. To ensure clarity, the experimental and theoretical plots are distinctly categorized within two separate subheadings: Experiment Methodology and Computation Methodology for ease of interpretation. The proposed sensor utilizes a heterostructure that protects the Ag-metal layer against oxidation and other problems with the environment, while simultaneously enhancing the overall performance. The main discovery and innovation of this study is the proposed SPR sensor that provides excellent sensitivity, enhanced adjustability, versatility, and a similar FOM. These advancements

are highly significant, not just for the advancement of cutting-edge sensing technologies, but also for their wider applications in photonics and optoelectronics.

7.2 Experiment

In this section, the focus is divided into three key subsections: Material, Sample Solutions Preparation, and Measurement of Refractive Index (RI). In the Material section, different honey samples, particularly various sugars, are meticulously studied to understand their properties and behaviors. Moving on to the Sample Solutions Preparation section, a critical aspect emerges that the density of the samples under study does not align uniformly [131]. As a result, to ensure accurate measurements and consistent experimental conditions, diluted and adulterated samples are meticulously prepared, allowing for controlled variations in concentration. Finally, in the Measurement of Refractive Index (RI) section, precise measurements of the refractive index are conducted on the prepared samples. This crucial step provides invaluable insights into the optical properties of the materials, contributing to a deeper understanding of their characteristics and behaviors within the experimental context.

7.2.1 Material

To achieve adulteration, three types of sugars-glucose (dextrose extra pure $C_6H_{12}O_6$), fructose ($C_6H_{12}O_6$), and sucrose ($C_{12}H_{22}O_{11}$) are obtained from Researchlab firm. The RI of each sample is measured using a portable digital refractometer manufactured by Parisa Technology in refractive index units (RIU). Unprocessed honey samples are generously provided by a well-established beekeeping company in Nashik, Maharashtra, called Raw and Real honey, following the winter 2023 flowering season Fig. 7.1 (a). Physical and chemical characteristics of the collected samples are directly measured: density (1.2 g/ml), refractive index (1.4953 RIU), and moisture content (16.5%) [131]. The analysis also included the commercially available honey brand Dabur Fig. 7.1 (b), with density (0.90 g/ml), refractive index (1.4886 RIU), and moisture content (19.5%). An attempt is made to determine the percentage of adulteration in an unknown honey sample. A sample of unknown honey is taken from the local market Fig. 7.1 (c).

Primary physicochemical parameters measured with a pocket refractometer are RI (1.4944 RIU) and moisture (17.2%) [131].

Fig. 7.1 (a) Unprocessed honey samples; (b) Dabur Honey; (c) Unknown honey

7.2.2 Sample Solutions preparation

The density of a solution depends on two variables: solute mass and solvent volume. Solutions with the same mass and volume have the same density regardless of the solute present. It measures how much mass is present in a specific volume of the solution. As density is equivalent to mass per unit volume, For example, if mass is in grams (g) and volume is in milliliters (ml), density will be in grams per milliliter (g/ml). To match the density of sugar solutions (glucose, fructose, and sucrose) with the honey sample, 50g of each sugar and honey sample are dissolved in 100ml of distilled water at room temperature, resulting in a 50% concentration, as recorded in Table 7.1 [131].

Table 7.1 Density of different sugar and unprocessed honey samples after 50% dilution

Type of solvent	Solvents weight (g)	Distilled water (ml)	Concentration (%)	Weight (g)	Total Volume (ml)	Density (g/ml)
Unprocessed honey sample	50	100	50	148	135	1.09
Glucose	50	100	50	154	132	1.16
Fructose	50	100	50	152	132	1.15
Sucrose	50	100	50	147	132	1.11

Diluted unprocessed honey is mixed with different sugar samples at various concentrations to create adulterated honey samples with a consistent density [183]. These prepared solutions are used as adulterated honey samples. To dilute Dabur honey while maintaining consistent density, 50g of Dabur honey is mixed with 100ml of distilled water. This results in a combined mass of 146g and a total volume of 132 ml, yielding a density of 1.106 g/ml. The diluted unknown honey sample is prepared by initially diluting 50g of the unknown honey sample in 100 ml of distilled water. The resulting diluted unknown honey sample has a mass of 138g and a volume of 130 ml, resulting in a density of 1.06 g/ml [131].

7.2.3 Measurement of refractive index (RI)

The RI of the diluted unprocessed honey sample, glucose, fructose, and sucrose solution after a 50% dilution in distilled water are recorded as 1.3781, 1.3872, 1.3902, and 1.3882 (RIU), respectively. Adulterated honey samples with consistent density are created by mixing diluted unprocessed honey with different diluted sugar samples at various concentrations, as shown in Fig. 7.2 [131]. The RI of various adulterated unprocessed honey samples is recorded and tabulated in Table 7.2.

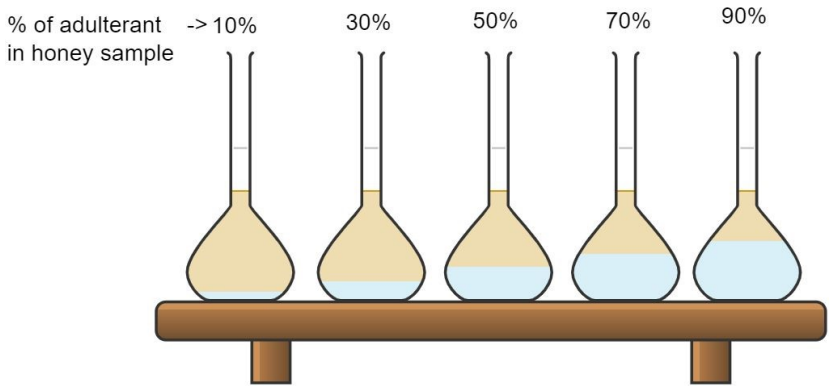

Fig. 7.2 Percentage of adulterant in diluted unprocessed honey sample

Sucrose fed to bees for food is converted to honey sugars (fructose and glucose) by over 95%. As a result, honey must have less than 5% sucrose naturally. Therefore, honey needs to have more than 5% sucrose to be adulterated, while less than 20% sucrose adulteration prevents crystallization. Therefore, the refractive indices of adulterated

unprocessed honey samples are recorded with different low concentrations (2 - 20 %) of sucrose adulterant. These are 1.3779, 1.378, 1.3784, 1.3787, 1.379, 1.3795, 1.380, 1.3801, 1.3803, and 1.3807 (RIU) at 2, 4, 6, 8, 10, 12, 14, 16, 18 and 20 % concentrations, respectively. Diluted Dabur honey sample has an observed RI of 1.374 (RIU) [131]. Different sugar samples are mixed with diluted Dabur honey in 10ml solutions at various concentrations to create a sample of adulterated Dabur honey. The RI of various adulterated Dabur honey samples is recorded and presented in Table 7.2 [131].

Table 7.2 RI of different adulterated Unprocessed and Dabur honey samples

Conc. of sugar solution (%)	Unprocessed honey with			Dabur Honey with		
	Glucose adulterant (RIU)	Fructose adulterant (RIU)	Sucrose adulterant (RIU)	Glucose adulterant (RIU)	Fructose adulterant (RIU)	Sucrose adulterant (RIU)
10	1.3791	1.3800	1.3790	1.3746	1.3806	1.3766
20	1.3792	1.3810	1.3807	1.3752	1.3847	1.3778
30	1.3809	1.3827	1.3810	1.3758	1.3870	1.3785
40	1.3823	1.3842	1.3835	1.3763	1.3852	1.3798
50	1.3831	1.3853	1.3850	1.3794	1.3867	1.3818
60	1.3845	1.3880	1.3860	1.3818	1.3882	1.3835
70	1.3850	1.3886	1.3865	1.3835	1.3900	1.3850
80	1.3862	1.3895	1.3884	1.3842	1.3911	1.3866
90	1.3870	1.3904	1.3894	1.3859	1.3920	1.3900

7.3 Computational Methodology

The Kretschmann and Reather model serves as the foundation for the design of the proposed SPR structure. The proposed structure is arranged in the subsequent sequences: BK7 glass prism, Ag-metal, wurtzite nitride semiconductor, WS_2, and sensing medium honey as shown in Fig. 7.3 [131]. The RI of prism BK7 with prescribed wavelength is 1.5151+i0 (RIU) [34]. Whereas Ag, GaN, AlN, InN and WS_2 refractive indices are 0.056253 + i4.2760 (RIU) [38], 2.3848 + i0 (RIU) [58], 2.1496 +i0 (RIU)

[59], 2.9+i0(RIU) [60], and 5.0646 + i0.23623 (RIU) [52], respectively. The RIs of the sensing medium are tabulated in the above section.

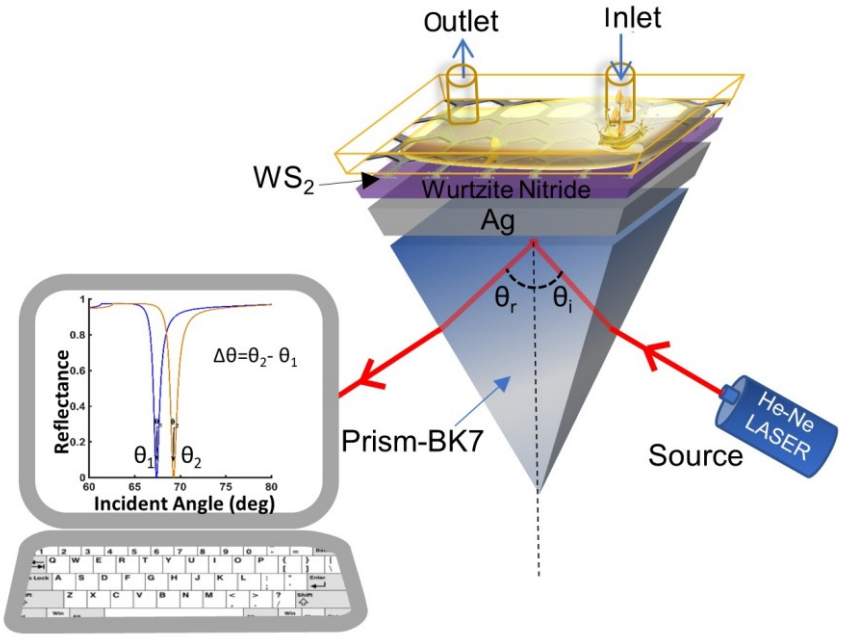

Fig. 7.3 Schematic diagram of proposed SPR sensor

In the current computation or simulation process, a monochromatic p-polarized He-Ne laser beam with a wavelength of 632.8 nm has been employed as the incident light source. As the proposed structure contains six layers, to get power reflection coefficient or *reflectance* at the interface, TMM is usually the best option comparable to the Fresnel equations. To find out the reflectance value, each layer is defined by RI n_k, dielectric constant ε_k, thickness d_k. The following equation represents the relation between the tangential fields at the first and last boundary.

$$\begin{bmatrix} E_1 \\ B_1 \end{bmatrix} = M \begin{bmatrix} E_{N-1} \\ B_{N-1} \end{bmatrix} \tag{7.1}$$

Where E_1 and B_1 are the electric and magnetic component at the first boundary respectively. E_{N-1} and B_{N-1} are the electric and magnetic component at the last

boundary respectively. Here $N = 6$ and M is the characteristic matrix represented by the following expression:

$$M_{ij} = \left(\prod_{k=2}^{N-1} M_k \right); i, j = 1, 2 \tag{7.2}$$

Where $M_k = \begin{pmatrix} \cos\beta_k & -(i\sin\beta_k)/q_k \\ -iq_k \sin\beta_k & \cos\beta_k \end{pmatrix}$; $q_k = \frac{\sqrt{(\varepsilon_k - n_1^2 \sin^2\theta)}}{\varepsilon_k}$; $\beta_k = d_k \left(\frac{2\pi}{\lambda} \right) \sqrt{(\varepsilon_k - n_1^2 \sin^2\theta)}$

Now the *reflectance* value computes using the following expression [149],

$$R = \left| \frac{(M_{11} + M_{12} q_N) q_1 - (M_{21} + M_{22} q_N)}{(M_{11} + M_{12} q_N) q_1 + (M_{21} + M_{22} q_N)} \right|^2 \tag{7.3}$$

Where, the angle of incidence and the wavelength of the incident light are denoted by θ and λ, respectively. To analyze the performance of the proposed structure, sensitivity (S), FOM, EF parameters have been studied at the interface. Sensitivity and FOM are calculated using the formulas outlined in chapter 3.

7.4 Results and Discussion

In this section, we discuss the series of steps undertaken to achieve an optimized design for detecting honey adulteration using SPR. Optimizing each layer within the proposed structure is crucial to achieving optimal performance. In MATLAB environment, the TMM is employed to determine the minimum achievable reflectance within the SPR sensor profile, enabling layer thickness optimization. To get the most effective from the proposed sensor, it is essential to minimize the reflectance value within the SPR curve. This lower reflectance indicates increased absorption of incident light. As a result at the sensor interface, the strength of the EF increases. The minimal reflectance value is used in the current study to optimize the thickness of several layers. Optimizing the Ag-metal layer's thickness, with a focus on identifying the point of minimum reflectance, is the initial adjustment required for the proposed construction. This optimization is achieved at 55nm, resulting in a minimal reflectance value of 0.000219.

Subsequently, the thickness of semiconductors is fine-tuned using a similar approach. For GaN, as the thickness increments in step of 1nm, Rmin values vary as follows: 0.000198, 0.000185, 0.000184, 0.000111, 8.11E-05, and 0.000189 until reaching 6nm. Notably, the observation reveals that the reflectance achieves its minimum at a 5nm thickness of GaN. Similarly, the increment in InN thickness results in a decrement of Rmin value until 4nm, reaching a value of 6.33E-05. Beyond this point, an increment is observed, with the reflectance increasing to 0.000392571 as InN reaches 5nm. A comparable variation is noted in the Rmin value of the proposed structure based on AlN. As the thickness increases, the Rmin value decreases as AlN till 5nm, reaching a value of 7.51E-05, and subsequently increases for succeeding values. Additionally, the number of WS_2 layers increases, leading to increment in Rmin values for proposed SPR sensor structure. It is noteworthy that the Rmin is achieved with a monolayer of WS_2. The proposed structure introduces layers sequentially, with the optimization of the Ag layer at 55 nm, followed by wurtzite nitrides set at 5 nm for GaN, 5 nm for AlN, and 4 nm for InN, respectively. The optimized thickness of WS_2 is 0.8 nm (monolayer) placed over the III-V nitride semiconductor family. Adulterant content in diluted honey samples ranges from 0% to 90%, serving as a sensing medium for the structure. The study of RI in adulterated honey samples aids SPR analysis. Using distilled water as a reference, the shift in SPR resonance angle is studied relative to the percentage of concentration of adulterants present in honey samples. The study has been categorized into distinct groups for the analysis of various honey samples, as outlined below:

7.4.1 Unprocessed Honey Study: Insights from SPR Curves

The SPR curve, which captures the response of different adulterants, is observed by utilizing a heterostructure (combination of wurtzite nitride and WS_2) in the proposed structure. The diluted honey sample is used to match the density of various adulterants. Figure 7.4 below illustrates the SPR curve for a diluted unprocessed honey sample, as well as the varying concentrations of glucose and fructose in the same sample for different heterostructures [131].

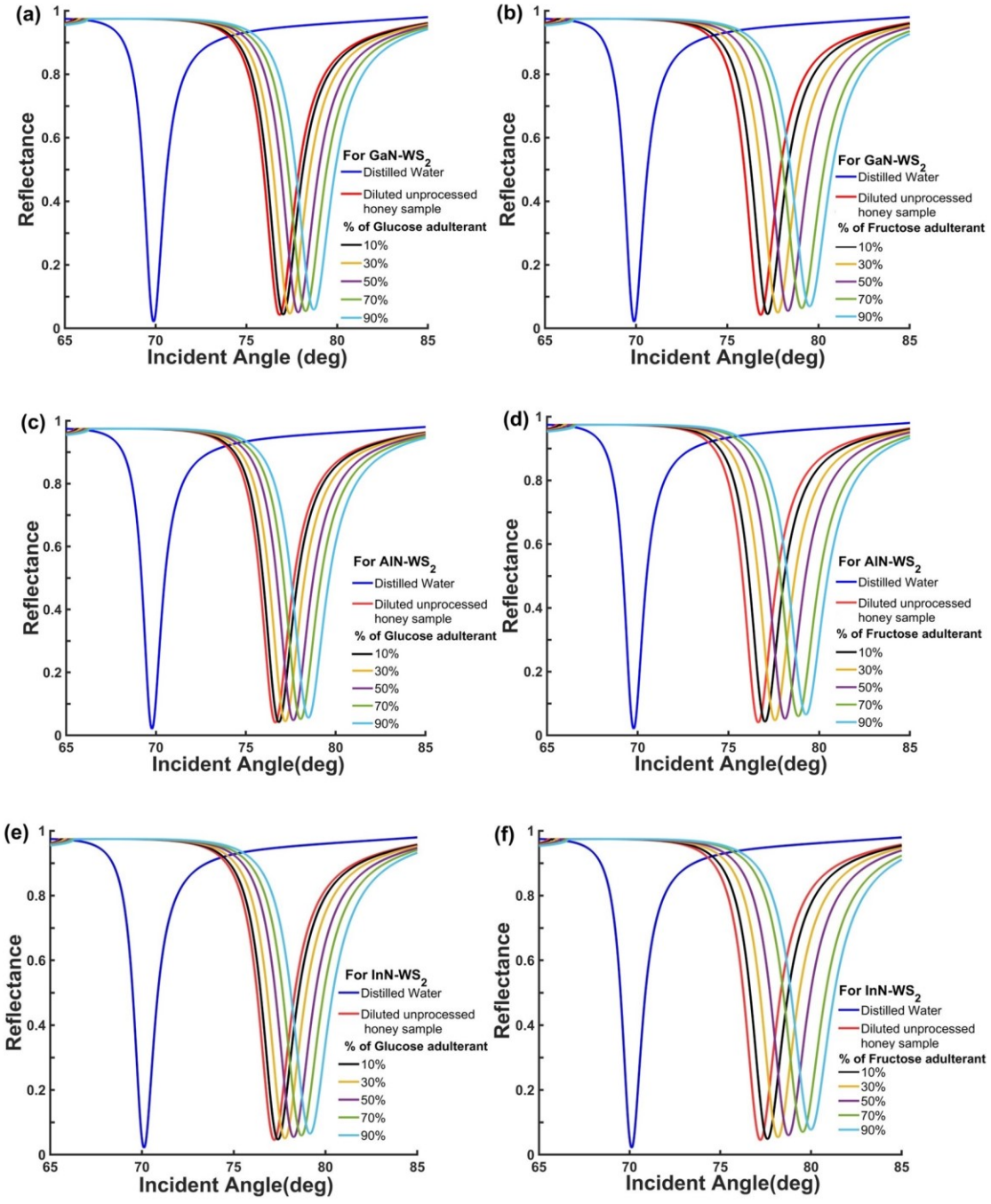

Fig. 7.4 SPR curve for a diluted unprocessed honey sample, highlighting the detection of varying concentrations of glucose (labelled as (a), (c), (e)) and fructose (labelled as (b), (d), (f)) adulterants.

The SPR curve for sucrose adulteration in diluted unprocessed honey sample is shown in Fig. 7.5 [131]. From Fig. 7.4 and Fig. 7.5, it is observed that, as the

concentration of adulterants in the honey sample increases, the resonance angle also increases. This suggests that the SPR sensor is capable of detecting and responding to different levels of adulteration in the honey sample. In essence, the resonance angle serves as a sensitive indicator, with higher angles corresponding to higher levels of adulteration, thus allowing for the quantification or identification of adulterants in the honey. Table sugar, scientifically known as sucrose, is composed equally of glucose and fructose. Fructose and glucose are independent of each other due to the presence of enzymes called invertases in honey, erected by honeybees. A rise in the sucrose concentration detected in honey may indicate the potential presence of honey adulteration.

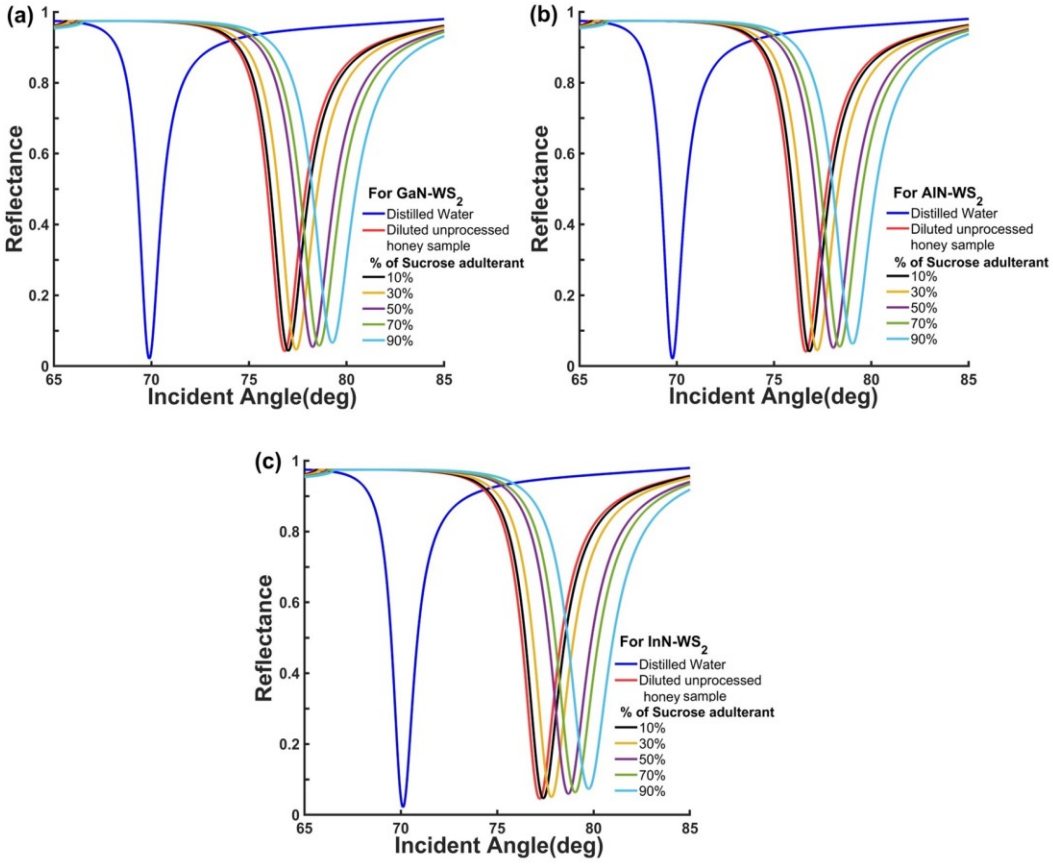

Fig.7.5 SPR curve for the detection of sucrose adulteration in diluted unprocessed honey samples using various heterostructures, namely: (a) GaN-WS_2, (b) AlN-WS_2, and (c) InN-WS_2.

An in-depth analysis is done to explore deeper into this concept, focusing on the shift in resonance angle of SPR and its correlation with the different concentration of adulterants in unprocessed honey samples. Figure 7.6 depicts how different types of adulteration affect the resonance angle in the SPR sensor in the presence of the above mentioned heterostructures. Specifically, it shows that the InN-WS_2 heterostructure exhibits the highest shift in resonance angle among all heterostructures when subjected to the different honey adulterations. This suggests that, in comparison to AlN-WS_2 and GaN-WS_2, the InN-WS_2 combination is particularly highly sensitive to changes in the honey sample due to adulteration. However, further investigation is required to ensure its reliability and accuracy in detecting adulteration in honey samples.

7.4.2 Intra-Wurtzite Nitride Semiconductor Comparison: Analyzing Comparative Differences

In a subsequent investigation, the sensitivity of the proposed SPR sensor with different concentrations of adulterants in unprocessed honey samples is examined. The findings and key outcomes of this study are graphically represented in Fig. 7.6 [131]. The graphical representation provides a clear and concise depiction of the sensor's performance, showcasing its consistent behavior across varying conditions. Figure 7.7 illustrates the relationship between the sensitivity and the percentage of concentration of adulterants in the honey samples [131]. The trend depicted in the graph reinforces the sensor's capability to deliver stable results, even under varying adulteration levels, which is critical for practical applications. Notably, the graph indicates that the sensitivity remains nearly constant across different concentrations of adulterants. This constancy of sensitivity highlights the sensor's design efficiency, ensuring accurate adulteration detection irrespective of sample variability. In essence, the study's findings imply that the proposed sensor maintains its sensitivity regardless of the concentration of adulterants, indicating its robustness, reliability, and suitability for detecting adulteration in honey samples. This degree of robustness not only highlights the technological potential of the sensor, but it also demonstrates that it is ready to be used in real-world applications for monitoring food quality.

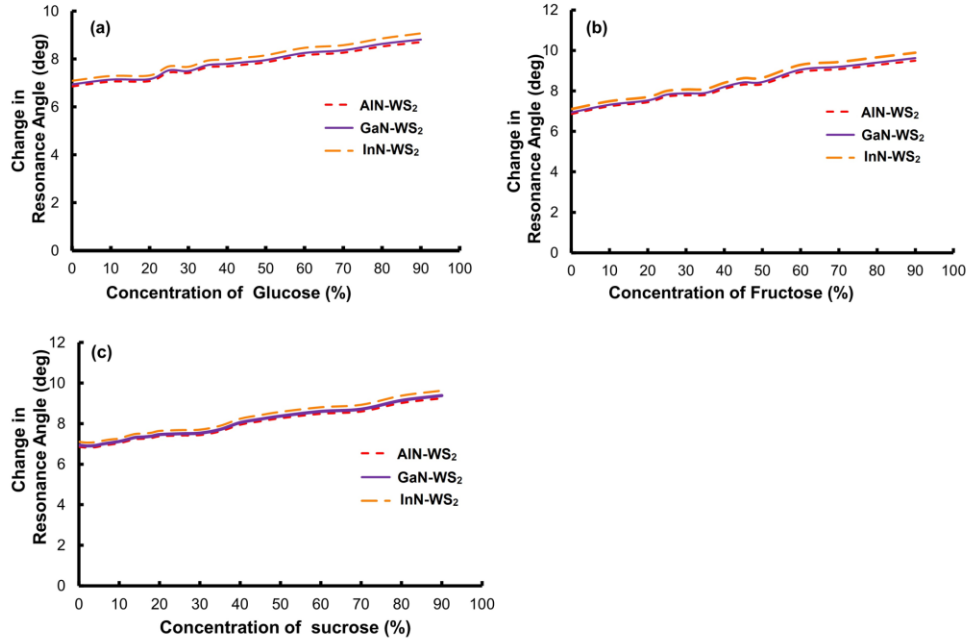

Fig. 7.6 Change in resonance angle of proposed sensor with respect to concentration of different adulterations for diverse heterostructures: (a) Glucose adulteration, (b) Fructose adulteration, and (c) Sucrose adulteration.

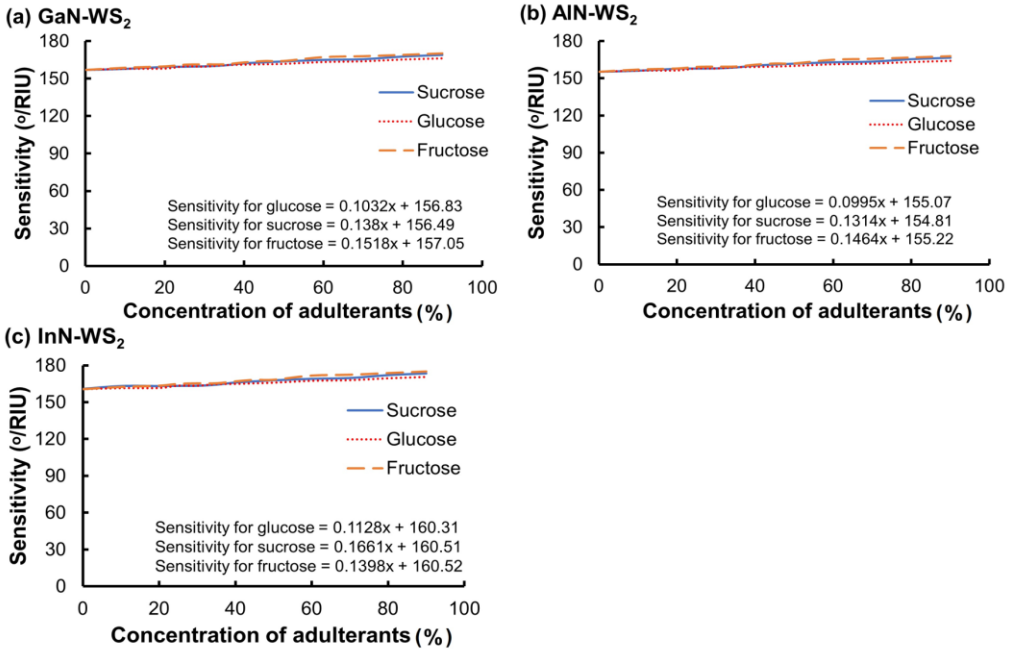

Fig. 7.7 Sensitivity of the proposed SPR sensor to different concentrations of adulterants in unprocessed honey samples for different heterostructure such as: (a) GaN-WS_2, (b) AlN-WS_2, and (c) InN-WS_2

Finite element analysis (FEA) is utilized to visualize the maximum EF at the sensing interface. Specifically, the wave optics module of COMSOL Multiphysics is employed for this purpose. Figure 7.8 provides a visual representation of the influence of distinct heterostructures, consisting of wurtzite nitride and WS_2, on the intensity of the EF at the interface [131]. It is observed that the InN-WS_2 heterostructure exhibits the highest recorded maximum electric field at resonance angle, measuring at 1.13E-04 V/nm. This observation is of paramount significance as it plays a critical role in achieving maximum sensitivity in the proposed sensor.

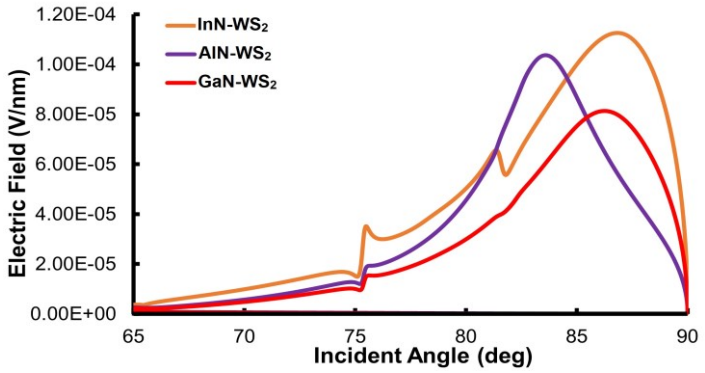

Fig. 7.8 Electric field of proposed structure with different heterostructures

From the above discussions, the proposed sensor with InN-WS_2 heterostructure outperforms that of GaN-WS_2 and AlN-WS_2. An extensive investigation is undertaken to detect adulterants in honey using the proposed SPR sensor structure based on InN-WS_2 is shown in Fig. 7.9 [131]. Figure 7.9 demonstrates how the inclusion of sucrose as an adulterant affects the resonance angle, positioned between the adulteration of glucose and fructose. This finding suggests that sucrose is a composite of glucose and fructose. Consequently, identifying sucrose adulteration in honey poses a challenging task. The proposed SPR sensor structure based on InN-WS_2 heterostructure with sensitivity 160.63 $^{\circ}$/RIU provides shift in resonance angle 7.09° with respect to the reference medium (distilled water) for diluted unprocessed honey sample. Figure 7.10 illustrates a 3D visualization, showcasing the EF at the sensing interface of the proposed sensor with InN-WS_2 heterostructure [131].

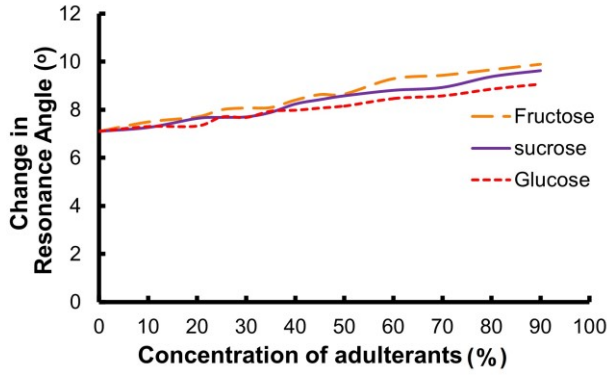

Fig. 7.9 Change in resonance angle with respect to concentration of different adulterations for unprocessed honey sample.

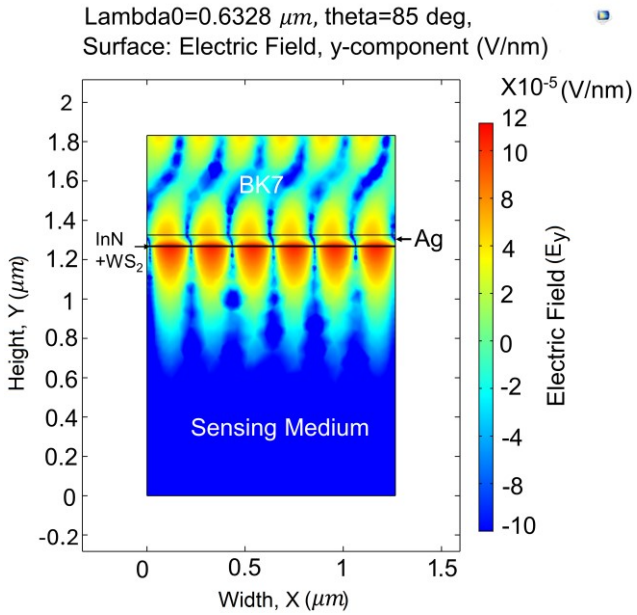

Fig. 7.10 Evanescent field at the sensing interface of the proposed InN-WS_2 based SPR configuration.

7.4.3 Exploring Diverse Samples: A Comparative Study

Sample 1: Dabur Honey, a renowned commercial brand

Dabur honey samples are intentionally adulterated with various adulterants, such as glucose, fructose, and sucrose. Table 7.2 shows the refractive indices of these adulterated samples, each with different concentrations of the adulterants. These recorded

refractive indices are utilized to analyze the characteristics of the SPR curves associated with the proposed structure.

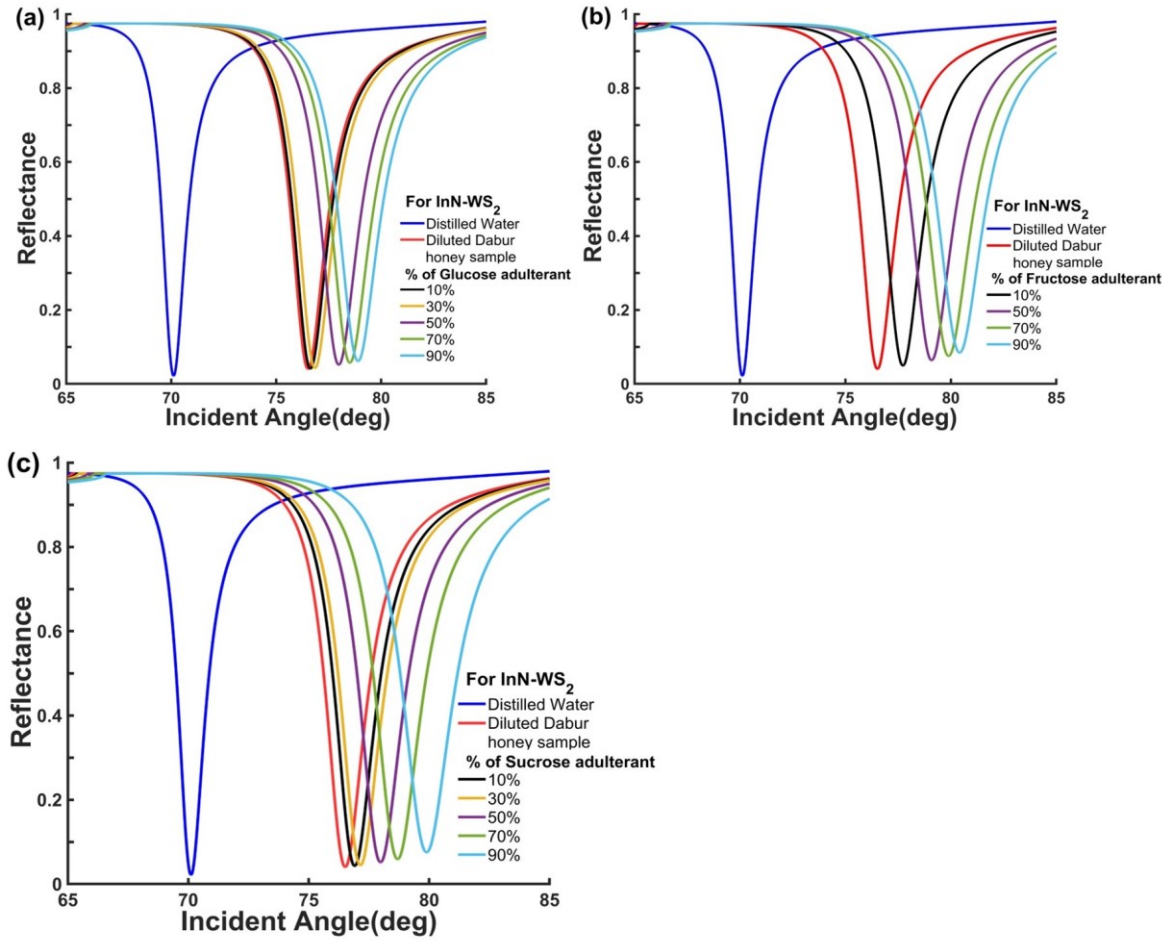

Fig. 7.11 SPR curve for a diluted Dabur honey sample at different concentrations of adulterants: (a) Glucose, (b) Fructose, and (c) Sucrose.

Figure 7.11 provides an insightful analysis of the SPR curve for diluted and adulterated Dabur honey samples [131]. The patterns shown by these SPR curves are intriguing. When the adulterant is glucose, the SPR curves seem to be densely grouped. In contrast, when fructose is used as an adulterant, the SPR curves show a significant spread. Similarly, when sucrose is employed as the adulterant, the SPR curves at lower concentrations of sucrose adulterant exhibit characteristics akin to those seen with

glucose adulterants. However, as the concentration of the sucrose adulterant increases, the nature of the SPR curves closely resembles that of fructose adulterants.

Additionally, Fig. 7.12 presents the outcomes of the proposed SPR sensor structure [131]. This figure includes an examination of varying concentrations of glucose, fructose, and sucrose adulterants with respect change in resonance angle. The results in Fig. 7.12 align with the trends observed in Fig. 7.9. Importantly, they emphasize that as the concentration of adulteration increases, the resonance angle shifts to its maximum value, highlighting the sensor's effectiveness in detecting adulterants.

Sample 2: Unknown Honey, local market

Figure 7.13 illustrates the SPR curve that depicts the behaviour of a diluted sample of unknown honey [131]. The sharp shift in the resonance angle, resulting in 7.39º, is a remarkable aspect of this curve. This shift corresponds to a sensitivity value of 162.06 (º/RIU). These findings highlight the proposed sensor's promising utility within the realm of honey quality assessment and the identification of adulteration, showcasing its ability to accurately discern and respond to minute variations in the RI of honey samples. A comparative overview of the proposed SPR sensor alongside previously reported works in literature is tabulated in table 7.3

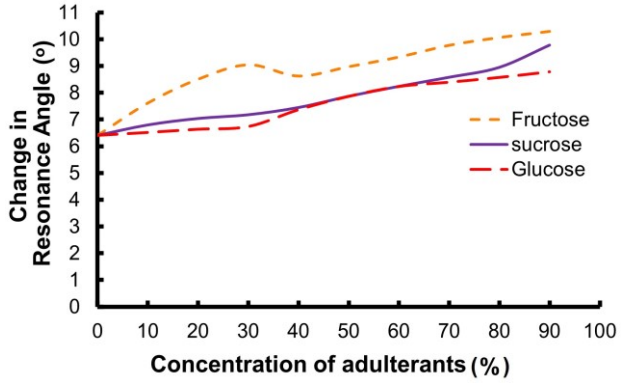

Fig. 7.12 Change in resonance angle with respect to concentration of different adulterations for Dabur honey sample.

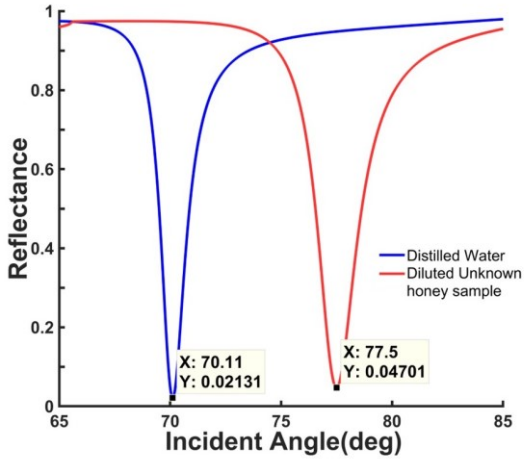

Fig. 7.13 SPR Intensity curve for a diluted unknown honey sample.

Table 7.3 Summary of sugar content in pure honey samples from previous studies

Study	Fructose	Glucose	F/G	Sucrose
Can et al. (2015) [184]	29.45%-54.04%	25.38%-22.14%	1.16-2.44	<5%
Geană et al. (2020) [185]	15.5%-49.3%	18.2%-48.0%	0.32–1.97	Not detected/ low amoun
Aykas (2023) [186]	31.2%-48.4%	15.3%-39.2%	NG	0.3-12.6%

These studies provide valuable insights into the composition of pure honey, indicating varying ranges of fructose, glucose, and sucrose content. The composition of pure honey typically exhibits an F/G ratio ranging from 0.95 to 1.50, while the sucrose content remains below 5% as per Table 7.3. However, the predicted fructose content of the unknown honey sample falls within the range of 4-8%, and the glucose content falls within 15-38%, which does not correspond to the expected F/G ratio. Similarly, the predicted sucrose content of the unknown sample ranges from 13-30%, which exceeds the acceptable limit of less than 5% found in pure honey. These comparisons indicate that the sugar composition of the unknown honey sample does not align with the typical sugar content observed in pure honey. It suggests the possibility of adulteration, such as table sugar.

7.4.4 Contrasting Findings: A Comparative Analysis

Furthermore, the performance of the proposed structure has been rigorously assessed in comparison to other contemporary SPR structures. Table 7.4 illustrates a comparative analysis of key performance metrics pertaining to the proposed SPR configuration. The sensitivity of the InN-WS_2, GaN-WS_2, and AlN-WS_2 based SPR configuration are found as 160.63 ^{0}/RIU, 157.01 ^{0}/RIU, 155.20 ^{0}/RIU respectively and corresponding SPR structure's FOM values are found as 77.6 RIU^{-1}, 79.70 RIU^{-1}, 80.42 RIU^{-1} respectively at operating wavelength 632.8 nm. All these performance parameters are significantly improved values in comparison to other reported results. Moreover, the SPR sensor utilizing InN-WS_2 exhibits the highest sensitivity and maximal enhancement of the EF at the sensor interface when compared to other structures based on wurtzite nitride-TMDC. Thus, the current research demonstrates superior functionality over existing SPR sensor structures, consequently, these high performance sensor structures hold significant potential for various detection applications.

Table 7.4 Comparison of the proposed sensor to previously reported sensors

Sensor structure	Operating wavelength	Sensitivity (^{0}/RIU)	FOM/QF RIU^{-1}	Reference
BK7-Ag-InN-WS_2	632.8 nm	160.63	77.6	Proposed
BK7-Ag-GaN-WS_2	632.8 nm	157.01	79.70	Proposed
BK7-Ag-AlN-WS_2	632.8 nm	155.20	80.42	Proposed
Prism/Ag/Mxene/ZnO/Graphene	633 nm	136.5	38.7	[187]
Prism/ZnO/Ag/Au/BaTiO3/Graphene	632.8 nm	116.67	37.87	[79]
Prism/Ag/graphene	633 nm	91.76	52.31	[62]
SF10-Au-ZnO-graphene	633 nm	141.9	9.14	[46]

In summary, the synergy among researchers, progress in fabrication techniques, and continuous efforts will play a vital role in advancing the development of the proposed SPR sensor for diverse applications.

7.5 Summary

The performance of SPR sensor based on wurtzite nitride and WS_2 heterostructure is studied and analyzed for the purpose of detecting honey adulteration. The heterostructure is incorporated on Ag novel metal surface and the honey sample serves as the sensing medium in the present study, and the refractive index of different honey samples at various concentrations is experimentally measured. This process presents challenges in maintaining precise conditions due to variations in the density and temperature of the samples. These factors require careful calibration to ensure consistency in measurements. In the high level computational environment, the TMM computes all the required performance parameters and generates theoretical plots to analyze sensor behavior. The outcomes show that the proposed structure based on the InN-WS_2 heterostructure provides the largest shift in θ_R for detecting all types of adulterants in honey, resulting in the highest sensitivity (160.63°/RIU). In comparison, the GaN-WS_2 configuration demonstrates a sensitivity of 157.01°/RIU, and the AlN-WS_2 configuration, which has a sensitivity of 155.20°/RIU, is lower than the InN-WS_2 configuration. Additionally, the EF intensity at the interface is examined, showing that the InN-WS_2 based SPR configuration achieves the maximum value among all combinations. Hence, InN-WS_2 is a suitable option for developing a highly sensitive, accurate, and reliable SPR sensor for the screening of honey from adulteration. Comparative analyses with previously reported SPR sensors further validate the superior functionality of the proposed wurtzite nitride -TMDC heterostructure based SPR sensor, demonstrating improved overall performance.

As the adulterated honey can cause a range of health and ethical concerns, the proposed sensor will help to maintain the integrity of the honey industry, protect consumers from deceptive practices, support ethical beekeepers and producers, and ensure that honey products meet regulatory standards and quality expectations.

CHAPTER 8

CONCLUSION AND FUTURE ASPECTS

This chapter concludes an in-depth exploration of thesis, focusing on conclusion and future aspect of the said study. The conclusion shows the impact and outcome of proposed structure of SPR sensor. Future aspects underscore the need for SPR sensors in food matrices, emphasizing the need for regulatory cooperation, ethical considerations, and the societal impact of SPR technology in the food industry.

Chapter 8

8.1 Conclusion

In present thesis, analysis of multilayered systems and surface waves within different material configurations has been extensively studied. This analysis is essential for understanding the underlying principles of the SPR phenomenon and for calculating SPR performance parameters. Different numerical models are explored to comprehensively understand sensor behavior. While Fresnel equations are a sensible choice for studying three-layer structures, as structure under the study is based on multiple layers. These equations become less effective for complex multilayer systems. Therefore, TMM is explored as it is suitable for studying multilayer structures. The TMM systematically breaks down a layered structure into a cascade of individual interfaces. The propagation of electromagnetic waves through such structure are examined at each interface. In TMM, multiplying the transfer matrices of each layer makes the calculation of the coefficient of reflection very convenient. The coefficient of reflection varies with incidence angle and reaches its smallest value, almost equal to zero, at resonance angle. This signifies the maximum absorption of incident photon energy for exciting the SPP at sensing medium interface. Resonance angle tracing in TMM becomes very simple and logical. The computation of performance parameters is made easier with the information embedded in SPR curves. The numerical models based on TMM have been designed with the help of simulation software such as MATLAB and COMSOL Multiphysics environment, making it very convenient to study the behaviour of SPR based sensors.

Building on this foundation, the first goal is to explore different prism and metal configurations to understand the impact of high refractive index prisms combined with various metals on the performance of SPR-based sensors. It is noteworthy that sensitivity, a critical performance parameter, reaches its maximum value in the SPR configuration using a BK7 glass prism. This outcome holds true across various active metals such as Au, Ag, and Cu, surpassing the performance of other prism materials. Ag-based SPR sensors show a sharp SPR curve, indicating improved detection accuracy with all types of prism. Although Au-based SPR provides maximum sensitivity, it also results in a wider

FWHM, making this type of sensor less accurate in determining the resonance angle. Additionally, the absorbed energy in Au-based sensors is not only used to generate evanescent waves but also dissipates as heat. Similarly, Cu-based SPR sensors show an impact similar to Au-based sensors but with lower sensitivity and a wider FWHM, making them less reliable. Furthermore, it was observed that as the percentage concentration of alcohol in water increases, the resonance angle value also increases, peaking at 80% alcohol concentration. However, at 100% alcohol concentration, the resonance angle value decreases compared to the previous one.

Moreover, the thesis explored innovative opportunities for advancing SPR technology by strategically integrating diverse heterostructures. This involved careful consideration of semiconductor candidates and 2D materials, with a particular focus on wurtzite nitrides as promising semiconductor options and members of TMDC family as suitable 2D materials. The incorporation of heterostructures between AlN-TMDC, GaN-TMDC, and InN-TMDC in SPR boosts the sensor's sensitivity by an average of 32.51%, 44.55%, and 45.08%, respectively. This deliberate integration of diverse heterostructures opens up new possibilities for enhancing SPR sensor performance and responsiveness, demonstrating the thesis's commitment to pushing the boundaries of SPR technology.

The next phase of the study examines the influence of bimetallic layers on the SPR structure compared to a single metallic layer. Building upon this exploration, the focus shifts to investigating the functionality of a heterostructure based on AlN and TMDC in a bimetallic based SPR structure. This heterostructure is placed strategically on an optimized bimetallic surface, which is a combination of Ag and Au, with the intention of not only enhancing sensor stability but also maximizing responsiveness. This deliberate integration of advanced materials and bimetallic surfaces marks a significant step forward in refining SPR sensor capabilities and underscores the thesis's dedication to pioneering advancements in the field. Expanding the scope of thesis, the study investigates the effectiveness of a SPR sensor utilizing wurtzite nitride and WS_2 heterostructure for detecting honey adulteration. Experimental measurements of refractive indices in various honey samples at different concentrations serve as the

foundation. Upon examining the performance parameters of the sensor, it is seen that the InN-WS_2 heterostructure produces a particularly notable resonance angle shift, resulting in increased sensitivity above other configurations. This makes InN-WS_2 a good candidate for constructing a highly sensitive and dependable SPR sensor. The proposed studies are compared with the existing studies in Table 7.4 with the intention of highlighting the importance of the study.

From an experimental standpoint, the realization of the proposed sensor is feasible, and the stacked layers can be grown using advanced fabrication techniques. Ag – metal can be deposited using physical vapor deposition (PVD) technique [188]. III-V nitride can be grown on the silver metal surface by Molecular-beam epitaxy (MBE) technique [189]. The utilization of the chemical vapour deposition (CVD) technique facilitates the production of a high quality WS_2 layer on the surface of III-V nitride [190]. Finally, a flow cell can be mounted on the top of the proposed sensor (as shown in Fig. 7.3), where the flow cell controls the sample flow. Furthermore, certain study groups have experimentally shown that functionalized WS_2 nanosheet plays a vital role in the identification of biological molecules like sucrose, maltose, glucose, and peptides [191,192]. However, to achieve a highly sensitive, stable, and selective InN-WS_2 based SPR sensor poses a few challenges like layer-by-layer (LbL) material deposition, high quality uniform WS_2 layer, tuned bandgap, material stability, biocompatibility, and integration with sensing platform. To overcome these challenges, it requires optimized synthesis techniques, encapsulation techniques to enhance material stability, precise bandgap engineering, surface functionalization with linkers and expertise in sensor integration.

8.2 Future Aspect

The literature of chapter 2 suggests an increasing interest in using SPR sensors to detect adulteration in a variety of food items. Studies show that SPR technology is adaptable to the particular compositional problems found in several food matrices. The literature indicates the flexibility of SPR sensors to detect adulteration in a variety of

food businesses though less work till recorded. As the literature grows, both problems and possibilities emerge for expanding SPR sensor applications to varied food matrices. Researchers investigate the difficulty of adapting sensor systems to distinct product features, emphasizing the importance of specialized techniques to manage unique adulteration concerns across a diverse range of food products. Miniaturization and mobility may enable speedy and convenient screening, making it more accessible for field applications and even meeting the practical demands of the honey business.

SPR sensor technology integration in the food business requires cooperation with regulatory agencies and industry stakeholders. This partnership assures that the proposed detection methods meet industry standards, which promotes credibility and general acceptance. By following regulatory criteria, the adoption of SPR sensors becomes smoother, enhancing their effectiveness in monitoring and preserving food quality.

Examine the social and ethical consequences of using SPR sensor technology in the food business, including issues about safeguarding sensitive data generated by the sensors to prevent unauthorized access, and the possible impact on small scale honey producers. Develop careful rules to ensure the responsible and ethical usage of SPR sensors, creating confidence and long term integration within the sector.

REFERENCES

References

1. M. J. McGrath and C. N. Scanaill, *Sensor Technologies: Healthcare, Wellness, and Environmental Applications* (Springer Nature, 2013).
2. C. Nylander, B. Liedberg, and T. Lind, "Gas detection by means of surface plasmon resonance," Sens. Actuators **3**, 79–88 (1982).
3. J. Homola, "Present and future of surface plasmon resonance biosensors," Anal. Bioanal. Chem. **377**, 528–539 (2003).
4. R. Verma, B. D. Gupta, and R. Jha, "Sensitivity enhancement of a surface plasmon resonance based biomolecules sensor using graphene and silicon layers," Sens. Actuators. B Chem. **160**, 623–631 (2011).
5. L. C. Clark and C. Lyons, "Electrode Systems for Continuous Monitoring in Cardiovascular Surgery," Ann. N. Y. Acad. Sci. **102**, 29–45 (1962).
6. R. A. S. Luz, R. M. Iost, and F. N. Crespilho, "Nanomaterials for Biosensors and Implantable Biodevices," in *Nanobioelectrochemistry: From Implantable Biosensors to Green Power Generation*, F. N. Crespilho, ed. (Springer Berlin Heidelberg, 2013), pp. 27–48.
7. V. Naresh and N. Lee, "A review on biosensors and recent development of nanostructured materials-enabled biosensors," Sensors **21**, 1109 (2021).
8. A. K. Singh, S. Mittal, M. Das, A. Saharia, and M. Tiwari, "Optical biosensors: a decade in review," Alexandria Eng. J. **67**, 673–691 (2023).
9. J. Homola, "Electromagnetic Theory of Surface Plasmons," in *Surface Plasmon Resonance Based Sensors*, J. Homola, ed. (Springer Berlin Heidelberg, 2006), pp. 3–44.
10. R. W. Wood, "On a remarkable case of uneven distribution of light in a diffraction grating spectrum.," London, Edinburgh, Dublin Philos. Mag. J. Sci. **4**, 396–402 (1902).
11. B. Liedberg, C. Nylander, and I. Lunström, "Surface plasmon resonance for gas detection and biosensing," Sens. Actuators **4**, 299–304 (1983).
12. J. Van Gent, P. V Lambeck, H. J. M. Kreuwel, G. J. Gerritsma, E. J. R. Sudholter, D. N. Reinhoudt, and T. J. A. Popma, "Optimization of a

chemooptical surface plasmon resonance based sensor," Appl. Opt. **29**, 2843 (1990).

13. B. Chadwick and M. Gal, "An optical temperature sensor using surface plasmons," Jpn. J. Appl. Phys. **32**, 2716–2717 (1993).
14. Ó. Esteban, F. B. Naranjo, N. Díaz-Herrera, S. Valdueza-Felip, M. C. Navarrete, and A. González-Cano, "High-sensitive SPR sensing with Indium Nitride as a dielectric overlay of optical fibers," Sens. Actuators. B Chem. **158**, 372–376 (2011).
15. W. L. Mochán, "Plasmons," in *Reference Module in Materials Science and Materials Engineering* (Elsevier Inc., 2016), pp. 1–13.
16. M. Achlan, "Surface Plasmon Polariton and Wave Guide Modes in a Six Layer Thin Film Stack," University of Paris-Saclay (2018).
17. J. J. Greffet, "Introduction to Surface Plasmon Theory," in *Plasmonics: From Basics to Advanced Topics*, S. Enoch and N. Bonod, eds. (Springer Berlin Heidelberg, 2012), pp. 105–148.
18. H. Raether, *Surface Plasmons on Smooth and Rough Surfaces and on Gratings*, 1st ed. (Springer Berlin, Heidelberg, 1988), Vol. 111.
19. M. Eldlio, F. Che, and M. Cada, "Drude-Lorentz Model of Semiconductor Optical Plasmons," in *IAENG Transactions on Engineering Technologies: Special Issue of the World Congress on Engineering and Computer Science 2012*, H. K. Kim, S. I. Ao, M. A. Amouzegar, and B. B. Rieger, eds. (Springer Netherlands, 2014), pp. 41–49.
20. M. A. Ordal, L. L. Long, R. J. Bell, S. E. Bell, R. R. Bell, R. W. Alexander, and C. A. Ward, "Optical properties of the metals Al, Co, Cu, Au, Fe, Pb, Ni, Pd, Pt, Ag, Ti, and W in the infrared and far infrared," Appl. Opt. **22**, 1099–1119 (1983).
21. S. A. Maier, *Plasmonics : Fundamentals and Applications* (Springer, 2007).
22. S. Kaya, "Photo-thermal control of surface plasmon mode propagation at telecom wavelengths," University of Bourgogne (2016).
23. S. K. Srivastava and B. D. Gupta, "Fiber optic plasmonic sensors: past, present and future," Open Opt. J. **7**, 58–83 (2013).
24. W. M. Mukhtar, S. Shaari, and P. Susthitha Menon, "Influences of light

coupling techniques to the excitation of surface plasmon polaritons," Adv. Sci. Lett. **19**, 66–69 (2013).

25. R. Bruns and H. Raether, "Plasma resonance radiation from non radiative plasmons," Zeitschrift für Phys. **237**, 98–106 (1970).
26. P. Lalanne and H. Liu, "A New Look at Grating Theories Through the Extraordinary Optical Transmission Phenomenon," in *Plasmonics: From Basics to Advanced Topics*, S. Enoch and N. Bonod, eds. (Springer Berlin Heidelberg, 2012), pp. 85–103.
27. A. Otto, "Excitation of nonradiative surface plasma waves in silver by the method of frustrated total reflection," Zeitschrift für Phys. A Hadron. Nucl. **216**, 398–410 (1968).
28. E. Kretschmann and H. Raether, "Radiative decay of non radiative surface plasmons excited by light," Zeitschrift für Naturforsch. A **23**, 2135–2136 (1968).
29. M. Milosevic, "Internal reflection and ATR spectroscopy," Appl. Spectrosc. Rev. **39**, 365–384 (2004).
30. J. Homola, S. S. Yee, and D. Myszka, "Surface plasmon resonance biosensors," in *Optical Biosensors: Today and Tomorrow*, F. S. L. and C. R. Taitt, ed., second ed (Elsevier, 2008), pp. 185–242.
31. V. Yesudasu, H. S. Pradhan, and R. J. Pandya, "Recent progress in surface plasmon resonance based sensors: A comprehensive review," Heliyon **7**, e06321 (2021).
32. J. Divya, S. Selvendran, A. S. Raja, and A. Sivasubramanian, "Surface plasmon based plasmonic sensors: A review on their past, present and future," Biosens. Bioelectron. X **11**, 100175 (2022).
33. W. Widayanti, K. Abraha, and A. B. Utomo, "A comparative study of applying different prisms and metalic layers in the surface plasmon resonance-based biosensor enhanced by the inclusion of the core-shell nanoparticles," AIP Conf. Proc. **2014**, 020080 (2018).
34. "SCHOTT Zemax catalog," available: http://www.schott.com.
35. J. Homola, S. S. Yee, and G. Gauglitz, "Surface plasmon resonance sensors: review," Sens. Actuators. B Chem. **54**, 3–15 (1999).

36. H. E. de Bruijn, R. P. H. Kooyman, and J. Greve, "Choice of metal and wavelength for surface-plasmon resonance sensors: some considerations," Appl. Opt. **31**, 440–442 (1992).
37. H. U. Yang, J. D'Archangel, M. L. Sundheimer, E. Tucker, G. D. Boreman, and M. B. Raschke, "Optical dielectric function of silver," Phys. Rev. B **91**, 235137 (2015).
38. P. B. Johnson and R. W. Christy, "Optical constant of the nobel metals," Phys. Rev. B **6**, 4370–4379 (1972).
39. A. Lahav, M. Auslender, and I. Abdulhalim, "Sensitivity enhancement of guided-wave surface-plasmon resonance sensors," Opt. Lett. **33**, 2539–2541 (2008).
40. J. B. Maurya and Y. K. Prajapati, "Influence of dielectric coating on performance of surface plasmon resonance sensor," Plasmonics **12**, 1121–1130 (2017).
41. G. V. Naik, V. M. Shalaev, and A. Boltasseva, "Alternative plasmonic materials: Beyond gold and silver," Adv. Mater. **25**, 3264–3294 (2013).
42. Y. Liu, X. Dong, and P. Chen, "Biological and chemical sensors based on graphene materials," Chem. Soc. Rev. **41**, 2283–2307 (2012).
43. Q. Ye, J. Wang, Z. Liu, Z. C. Deng, X. T. Kong, F. Xing, X. D. Chen, W. Y. Zhou, C. P. Zhang, and J. G. Tian, "Polarization-dependent optical absorption of graphene under total internal reflection," Appl. Phys. Lett. **102**, 021912 (2013).
44. B. Vasić, G. Isić, and R. Gajić, "Localized surface plasmon resonances in graphene ribbon arrays for sensing of dielectric environment at infrared frequencies," J. Appl. Phys. **113**, 013110 (2013).
45. Y. Zhu, S. Murali, W. Cai, X. Li, J. W. Suk, J. R. Potts, and R. S. Ruoff, "Graphene and graphene oxide: Synthesis, properties, and applications," Adv. Mater. **22**, 3906–3924 (2010).
46. S. Pal, Y. K. Prajapati, and J. P. Saini, "Influence of graphene's chemical potential on SPR biosensor using ZnO for DNA hybridization," Opt. Rev. **27**, 57–64 (2020).
47. A. V. Kolobov and J. Tominaga, *Two-Dimensional Transition-Metal*

Dichalcogenides (Springer, 2016), Vol. 239.

48. X. Zhao, T. Huang, P. S. Ping, X. Wu, P. Huang, J. Pan, Y. Wu, and Z. Cheng, "Sensitivity enhancement in surface plasmon resonance biochemical sensor based on transition metal dichalcogenides/graphene heterostructure," Sensors **18**, 2056 (2018).
49. Q. Ouyang, S. Zeng, L. Jiang, L. Hong, G. Xu, X. Q. Dinh, J. Qian, S. He, J. Qu, P. Coquet, and K. T. Yong, "Sensitivity enhancement of transition metal dichalcogenides/silicon nanostructure-based surface plasmon resonance biosensor," Sci. Rep. **6**, 28190 (2016).
50. W. Tang, S. Rassay, and N. Ravindra, "Electronic & optical properties of transition- metal dichalcogenides," Madridge J. Nanotechnol. Nanosci. **2**, 59–65 (2017).
51. M. Bruna and S. Borini, "Optical constants of graphene layers in the visible range," Appl. Phys. Lett. **94**, 031901 (2009).
52. C. Hsu, R. Frisenda, R. Schmidt, A. Arora, S. M. de Vasconcellos, R. Bratschitsch, H. S. J. van der Zant, and A. Castellanos Gomez, "Thickness-dependent refractive index of 1L, 2L, and 3L MoS2, MoSe2, WS2, and WSe2," Adv. Opt. Mater. **7**, 1900239 (2019).
53. S. Meng, Y. Zhang, H. Wang, L. Wang, T. Kong, H. Zhang, and S. Meng, "Recent advances on TMDCs for medical diagnosis," Biomaterials **269**, 120471 (2021).
54. P. Bhatia and B. D. Gupta, "Surface-plasmon-resonance-based fiber-optic refractive index sensor: sensitivity enhancement," Appl. Opt. **50**, 2032–2036 (2011).
55. X. Li and X. Liu, "Group III nitride nanomaterials for biosensing," Nanoscale **9**, 7320–7341 (2017).
56. J. Wu, "When group-III nitrides go infrared: New properties and perspectives," J. Appl. Phys. **106**, 011101 (2009).
57. D. E. Aspnes and A. A. Studna, "Dielectric functions and optical parameters of Si, Ge, GaP, GaAs, GaSb, InP, InAs, and InSb from 1.5 to 6.0 eV," Phys. Rev. B **27**, 985–1009 (1983).
58. A. S. Barker and M. Ilegems, "Infrared lattice vibrations and free-electron

dispersion in GaN," Phys. Rev. B **7**, 743–750 (1973).

59. J. Pastrňák and L. Roskovcová, "Refraction index measurements on AlN single crystals," Phys. Stat. Sol. **14**, K5–K8 (1966).
60. M. E. Levinshtein, S. L. Rumyantsev, and M. S. Shur, *Properties of Advanced Semiconductor Materials GaN, AlN, InN, BN, SiC, SiGe* (John Wiley & Sons, 2001).
61. L. Xia, S. Yin, H. Gao, Q. Deng, and C. Du, "Sensitivity enhancement for surface plasmon resonance imaging biosensor by utilizing gold-silver bimetallic film configuration," Plasmonics **6**, 245–250 (2011).
62. P. K. Maharana, P. Padhy, and R. Jha, "On the field enhancement and performance of an ultra-stable SPR biosensor based on graphene," IEEE Photonics Technol. Lett. **25**, 2156–2159 (2013).
63. A. Verma, A. Prakash, and R. Tripathi, "Sensitivity enhancement of surface plasmon resonance biosensor using graphene and air gap," Opt. Commun. **357**, 106–112 (2015).
64. Z. Lin, L. Jiang, L. Wu, J. Guo, X. Dai, Y. Xiang, and D. Fan, "Tuning and sensitivity enhancement of surface plasmon resonance biosensor with graphene covered Au-MoS2-Au films," IEEE Photonics J. **8**, 1–8 (2016).
65. A. K. Mishra and S. K. Mishra, "MgF2 prism/rhodium/graphene: efficient refractive index sensing structure in optical domain," J. Phys. Condens. Matter **29**, 145001 (2017).
66. M. S. Rahman, M. S. Anower, M. R. Hasan, M. B. Hossain, and M. I. Haque, "Design and numerical analysis of highly sensitive Au-MoS2-graphene based hybrid surface plasmon resonance biosensor," Opt. Commun. **396**, 36–43 (2017).
67. S. Aksimsek, H. Jussila, and Z. Sun, "Graphene–MoS2–metal hybrid structures for plasmonic biosensors," Opt. Commun. **428**, 233–239 (2018).
68. A. K. Sharma and A. K. Pandey, "Blue phosphorene/MoS2 heterostructure based SPR sensor with enhanced sensitivity," IEEE Photonics Technol. Lett. **30**, 595–598 (2018).
69. J. Banerjee and M. Ray, "Comparative performance evaluation of mono-metallic and bi-metallic plasmonic sensors using WS2 and graphene with

optical bio-sensing application," Sens. Actuators. B Chem. **281**, 520–526 (2019).

70. A. Srivastava, A. Verma, R. Das, and Y. K. Prajapati, "A theoretical approach to improve the performance of SPR biosensor using MXene and black phosphorus," Optik. **203**, 163430 (2020).
71. A. Nisha, P. Maheswari, P. M. Anbarasan, K. B. Rajesh, and Z. Jaroszewicz, "Sensitivity enhancement of surface plasmon resonance sensor with 2D material covered noble and magnetic material (Ni)," Opt. Quant. Electron. **51**, 19 (2019).
72. Y. Jia, Z. Li, H. Wang, M. Saeed, and H. Cai, "Sensitivity enhancement of a surface plasmon resonance sensor with platinum diselenide," Sensors **20**, 131 (2020).
73. D. T. Nurrohman and N. F. Chiu, "Surface plasmon resonance biosensor performance analysis on 2D material based on graphene and transition metal dichalcogenides," ECS J. Solid State Sci. Technol. **9**, 115023 (2020).
74. K. A. Rikta, M. S. Anower, M. S. Rahman, and M. M. Rahman, "SPR biosensor using SnSe-phosphorene heterostructure," Sens. Biosensing. Res. **33**, 100442 (2021).
75. P. Zhang, J. Wang, G. Chen, J. Shen, C. Li, and T. Tang, "A high-sensitivity SPR sensor with bimetal/silicon/two-dimensional material structure: A theoretical analysis," Photonics **8**, 270 (2021).
76. R. Kumar, S. Pal, Y. K. Prajapati, and J. P. Saini, "Sensitivity enhancement of MXene based SPR sensor using silicon: theoretical analysis," Silicon **13**, 1887–1894 (2021).
77. B. Karki, A. Uniyal, A. Pal, and V. Srivastava, "Advances in Surface Plasmon Resonance-Based Biosensor Technologies for Cancer Cell Detection," Int. J. Opt. **2022**, 1476254 (2022).
78. Y. Jia, Y. Liao, and H. Cai, "High Quality TaS2 Nanosheet SPR Biosensors Improved Sensitivity and the Experimental Demonstration for the Detection of Hg2+," Nanomaterials **12**, 2075 (2022).
79. N. Mudgal, A. Saharia, A. Agarwal, and G. Singh, "ZnO and bi-metallic (Ag–Au) layers based surface plasmon resonance (SPR) biosensor with

BaTiO3 and graphene for biosensing applications," IETE J. Res. **69**, 932–939 (2023).

80. V. V. Kotha, S. Vankayalapati, Y. Vasimalla, J. Vaadaala, S. Jain, B. Ramachandran, C. Santhosh, S. Maloji, and S. Kumar, "Ultra-Sensitive Prism-Based Surface Plasmon Resonance Biosensor Utilizing Lead Molybdate and BlueP/TDMC Nanocomposites for Early Malaria Detection," Plasmonics (2024).
81. C. Hu, N. Gan, Y. Chen, L. Bi, X. Zhang, and L. Song, "Detection of microcystins in environmental samples using surface plasmon resonance biosensor," Talanta **80**, 407–410 (2009).
82. S. Neethirajan, V. Ragavan, X. Weng, and R. Chand, "Biosensors for sustainable food engineering: challenges and perspectives," Biosensors **8**, 23 (2018).
83. W. M. E. M. Mohd Daniyal, S. Saleviter, and Y. W. Fen, "Development of surface plasmon resonance spectroscopy for metal ion detection," Sensors Mater. **30**, 2023–2038 (2018).
84. B. G. Şolomonea, L. I. Jinga, V. A. Antohe, G. Socol, and I. Antohe, "Cadmium ions' trace-level detection using a portable fiber optic—surface plasmon resonance sensor," Biosensors **12**, 573 (2022).
85. H. Yuan, G. Sun, W. Peng, W. Ji, S. Chu, Q. Liu, and Y. Liang, "Thymine-functionalized gold nanoparticles (Au NPs) for a highly sensitive fiber-optic surface plasmon resonance mercury ion nanosensor," Nanomaterials **11**, 397 (2021).
86. Y. Zhao, S. Gan, L. Wu, J. Zhu, Y. Xiang, and X. Dai, "GeSe nanosheets modified surface plasmon resonance sensors for enhancing sensitivity," Nanophotonics **9**, 327–336 (2020).
87. A. Bajaj, A. M. Shrivastav, E. Eltzov, N. Alkan, and I. Abdulhalim, "Detection of necrotrophic DNA marker of anthracnose causing colletotrichum gloeosporioides fungi in harvested produce using surface plasmon resonance," Talanta **235**, 122776 (2021).
88. R. D'aurelio, J. Ashley, T. L. Rodgers, L. Trinh, J. Temblay, M. Pleasants, and I. E. Tothill, "Development of a nanomips-SPR-based sensor for β-

lactoglobulin detection," Chemosensors **8**, 94 (2020).

89. J. Zhou, Y. Wang, Y. Qian, T. Zhang, L. Zheng, and L. Fu, "Quantification of shellfish major allergen tropomyosin by SPR biosensor with gold patterned Biochips," Food Control **107**, 106547 (2020).
90. D. Bhandari, F. C. Chen, and R. C. Bridgman, "Detection of salmonella typhimurium in romaine lettuce using a surface plasmon resonance biosensor," Biosensors **9**, 94 (2019).
91. T. Wei, P. Ren, L. Huang, Z. Ouyang, Z. Wang, X. Kong, T. Li, Y. Yin, Y. Wu, and Q. He, "Simultaneous detection of aflatoxin B1, ochratoxin A, zearalenone and deoxynivalenol in corn and wheat using surface plasmon resonance," Food Chem. **300**, 125176 (2019).
92. I. Yazgan, N. M. Noah, O. Toure, S. Zhang, and O. A. Sadik, "Biosensor for selective detection of E. coli in spinach using the strong affinity of derivatized mannose with fimbrial lectin," Biosens. Bioelectron. **61**, 266–273 (2014).
93. S. Pal, A. Verma, S. Raikwar, Y. K. Prajapati, and J. P. Saini, "Detection of DNA hybridization using graphene-coated black phosphorus surface plasmon resonance sensor," Appl. Phys. A **124**, 394 (2018).
94. S. Ahmed and S. Kabir, "Copper- germanium-graphene based highly sensitive plasmonic biosensor for protein detection," in *2018 International Conference on Computer, Communication, Chemical, Material and Electronic Engineering (IC4ME2)* (IEEE, 2018), pp. 1–4.
95. H. Yoo, J. Shin, J. Sim, H. Cho, and S. Hong, "Reusable surface plasmon resonance biosensor chip for the detection of H1N1 influenza virus," Biosens. Bioelectron. **168**, 112561 (2020).
96. P. K. Sharma, J. S. Kumar, V. V. Singh, U. Biswas, S. S. Sarkar, S. I. Alam, P. K. Dash, M. Boopathi, K. Ganesan, and R. Jain, "Surface plasmon resonance sensing of Ebola virus: a biological threat," Anal. Bioanal. Chem. **412**, 4101–4112 (2020).
97. G. M. C. dos Santos, C. R. Alves, M. A. Pinto, L. A. Amado Leon, and F. Souza-Silva, "Detection of antibodies against hepatitis a virus (HAV) by a surface plasmon resonance (SPR) biosensor: a new diagnosis tool based on

the major HAV capsid protein VP1 (SPR-HAVP1)," Sensors **21**, 3167 (2021).

98. A. Sjahrurachman, B. E. Dewi, K. Lischer, D. K. Pratami, D. Flamandita, and M. Sahlan, "Surface plasmon resonance analysis for detecting non-structural protein 1 of dengue virus in Indonesia," Saudi J. Biol. Sci. **27**, 1931–1937 (2020).
99. S. Mostufa, A. K. Paul, and K. Chakrabarti, "Detection of hemoglobin in blood and urine glucose level samples using a graphene-coated SPR based biosensor," OSA Contin. **4**, 2164–2176 (2021).
100. D. Rithesh Raj, S. Prasanth, T. V. Vineeshkumar, and C. Sudarsanakumar, "Surface plasmon resonance based fiber optic sensor for mercury detection using gold nanoparticles PVA hybrid," Opt. Commun. **367**, 102–107 (2016).
101. C. Genslein, P. Hausler, E. M. Kirchner, R. Bierl, A. J. Baeumner, and T. Hirsch, "Graphene-enhanced plasmonic nanohole arrays for environmental sensing in aqueous samples," Beilstein J. Nanotechnol. **7**, 1564–1573 (2016).
102. J. Castillo, J. Chirinos, H. Gutiérrez, and M. La Cruz, "Surface plasmon resonance sensor based on golden nanoparticles and cold vapour generation technique for the detection of mercury in aqueous samples," Opt. Laser Technol. **94**, 34–39 (2017).
103. Y. Saylan, S. Akgönüllü, D. Çimen, A. Derazshamshir, N. Bereli, F. Yılmaz, and A. Denizli, "Development of surface plasmon resonance sensors based on molecularly imprinted nanofilms for sensitive and selective detection of pesticides," Sensors Actuators, B Chem. **241**, 446–454 (2017).
104. O. Çakır and Z. Baysal, "Pesticide analysis with molecularly imprinted nanofilms using surface plasmon resonance sensor and LC-MS/MS: comparative study for environmental water samples," Sens. Actuators. B Chem. **297**, 126764 (2019).
105. V. P. Prakashan, G. George, M. S. Sanu, M. S. Sajna, A. C. Saritha, C. Sudarsanakumar, P. R. Biju, C. Joseph, and N. V. Unnikrishnan,

"Investigations on SPR induced Cu@Ag core shell doped SiO2-TiO2-ZrO2 fiber optic sensor for mercury detection," Appl. Surf. Sci. **507**, 144957 (2020).

106. R. K. Verma, P. Suwalka, and J. Yadav, "Detection of adulteration in diesel and petrol by kerosene using SPR based fiber optic technique," Opt. Fiber Technol. **43**, 95–100 (2018).
107. H. S. Hashim, Y. W. Fen, N. A. Sheh Omar, J. Abdullah, W. M. E. M. M. Daniyal, and S. Saleviter, "Detection of phenol by incorporation of gold modified-enzyme based graphene oxide thin film with surface plasmon resonance technique," Opt. Express **28**, 9738–9752 (2020).
108. F. Li-Hui and D. Junfeng, "A Measuring Method of DOM Components Based on Fiber SPR Sensor and ICPSO-BP Neural Network," IEEE Access **10**, 23716–23731 (2022).
109. R. Rahad, A. K. M. Rakib, M. K. Mahadi, and M. O. Faruque, "Fuel classification and adulteration detection using a highly sensitive plasmonic sensor," Sens. Biosensing. Res. **40**, 100560 (2023).
110. P. Jahanshahi, S. D. Sekaran, and F. R. M. Adikan, "Optical and analytical investigations on dengue virus rapid diagnostic test for IgM antibody detection," Med. Biol. Eng. Comput. **53**, 679–687 (2015).
111. J. B. Maurya, Y. K. Prajapati, and R. Tripathi, "Effect of molybdenum disulfide layer on surface plasmon resonance biosensor for the detection of bacteria," Silicon **10**, 245–256 (2018).
112. S. Farooq and R. E. de Araujo, "Engineering a Localized Surface Plasmon Resonance Platform for Molecular Biosensing," Open J. Appl. Sci. **08**, 126–139 (2018).
113. S. Farooq, W. W. Neves, O. Pandoli, T. Del Rosso, L. M. de Lima, R. F. Dutra, and R. E. de Araujo, "Engineering a plasmonic sensing platform for Candida albicans antigen identification," J. Nanophotonics **12**, 033003 (2018).
114. M. Saifur Rahman, K. A. Rikta, L. F. Abdulrazak, and M. S. Anower, "Enhanced performance of SnSe-Graphene hybrid photonic surface plasmon refractive sensor for biosensing applications," Photonics.

Nanostruct. **39**, 100779 (2020).

115. A. K. Sharma, B. Kaur, and C. Marques, "Simulation and analysis of 2D material/metal carbide based fiber optic SPR probe for ultrasensitive cortisol detection," Optik. **218**, 164891 (2020).
116. T. aki Yano, T. Kajisa, M. Ono, Y. Miyasaka, Y. Hasegawa, A. Saito, K. Otsuka, A. Sakane, T. Sasaki, K. Yasutomo, R. Hamajima, Y. Kanai, T. Kobayashi, Y. Matsuura, M. Itonaga, and T. Yasui, "Ultrasensitive detection of SARS-CoV-2 nucleocapsid protein using large gold nanoparticle-enhanced surface plasmon resonance," Sci. Rep. **12**, 1060 (2022).
117. S. Farooq, F. Wali, D. M. Zezell, R. E. de Araujo, and D. Rativa, "Optimizing and Quantifying Gold Nanospheres Based on LSPR Label-Free Biosensor for Dengue Diagnosis," Polymers. **14**, 1592 (2022).
118. B. Karki, N. H. Salah, G. Srivastava, A. Muduli, and R. B. Yadav, "A simulation study for dengue virus detection using surface plasmon resonance sensor heterostructure of silver, barium titanate, and cerium oxide," Plasmonics **18**, 2031–2040 (2023).
119. S. Jiang, S. Qian, S. Zhu, J. Lu, Y. Hu, C. Zhang, Y. Geng, X. Chen, Y. Guo, Z. Chen, J. Pu, Z. Guo, and S. Liu, "A Point-of-Care Testing Device Utilizing Graphene-Enhanced Fiber Optic SPR Sensor for Real-Time Detection of Infectious Pathogens," Biosensors **13**, 1029 (2023).
120. K. Erol, G. Hasabnis, and Z. Altintas, "A Novel NanoMIP–SPR Sensor for the Point-of-Care Diagnosis of Breast Cancer," Micromachines **14**, 1086 (2023).
121. S. Dai, J. Mi, J. Dou, W. Shi, J. Zhang, and J. Zhao, "Label-free and dynamic monitoring of cell evolutions using wavelength-multiplexing surface plasmon resonance holographic microscopy," Biomed. Opt. Express **14**, 2028–2039 (2023).
122. D. Pal, A. H. M. Almawgani, S. Das, A. Pal, M. Kumar, A. Uniyal, and A. Alzahrani, "A Highly Sensitive Long-Range Surface Plasmon Resonance Biosensor for the Determination of Hemoglobin Content in Human Blood," Plasmonics (2024).

123. A. Pal, Y. Trabelsi, P. Sarkar, and R. Bharos, "Plasmonic pregnancy detector : enhancing sensitivity with SPR sensor," Opt. Quant. Electron. **56**, 1404 (2024).

124. A. Upadhyay, S. Singh, B. Chaudhary, R. Kumar, P. P. Singh, M. G. Daher, P. Bhardwaj, M. M. A. Eid, and A. N. Z. Rashed, "Biosensor Performance Signature Enhancement with Silver-MXene-Graphene for Brain Tumor Diagnosis Through the Employment of Surface Plasmon Resonance," Plasmonics (2024).

125. S. A. Rafi, W. Emon, A. A. Rafsan, R. R. Mahmud, M. F. Nayan, M. M. A. Eid, and A. N. Z. Rashed, "Optical Based Surface Plasmon Resonance Sensor for the Detection of the Various Kind of Cancerous Cell," Cell Biochem. Biophys. (2024).

126. M. Mansouri, F. Fathi, R. Jalili, S. Shoeibie, S. Dastmalchi, A. Khataee, and M. R. Rashidi, "SPR enhanced DNA biosensor for sensitive detection of donkey meat adulteration," Food Chem. **331**, 127163 (2020).

127. D. Çimen, S. Aslıyüce, T. D. Tanalp, and A. Denizli, "Molecularly imprinted nanofilms for endotoxin detection using an surface plasmon resonance sensor," Anal. Biochem. **632**, 114221 (2021).

128. V. Semwal and B. D. Gupta, "Highly selective SPR based fiber optic sensor for the detection of hydrogen peroxide," Sens. Actuators. B Chem. **329**, 129062 (2021).

129. S. K. Singh, A. Srivastava, and L. K. Dwivedi, "A theoretical analysis of milk adulteration/contamination detection in camel, buffalo and cow milk using SPR technique," J. Phys. Conf. Ser. **2426**, 012040 (2023).

130. B. Karki, Y. Trabelsi, A. Uniyal, A. Pal, and R. Bharos Yadav, "Detection of fat concentration milk using TMDC-based surface plasmon resonance sensor," Mod. Phys. Lett. B **38**, 2450253 (2024).

131. T. M. S. Ashrafi and G. Mohanty, "Ultra-sensitive plasmonic sensor for detecting honey adulteration with III-V Nitride and Tungsten Disulfide," Sens. Imaging **25**, 19 (2024).

132. F. Abelès, "Optical properties of very thin films," Thin Solid Films **34**, 291–302 (1976).

133. M. Milosevic, "Fresnel equations," in *Internal Reflection and ATR Spectroscopy*, First (John Wiley & Sons, Inc., 2012), pp. 39–49.
134. R. B. Balili, "Transfer matrix method in nanophotonics," Int. J. Mod. Phys. Conf. Ser. **17**, 159–168 (2012).
135. Z. H. Mohammed, "The fresnel coefficient of thin film multilayer using transfer matrix method TMM," in *IOP Conference Series: Materials Science and Engineering* (Institute of Physics Publishing, 2019), Vol. 518, p. 032026.
136. A. Shalabney and I. Abdulhalim, "Sensitivity-enhancement methods for surface plasmon sensors," Laser Photonics Rev. **5**, 571–606 (2011).
137. K. Brahmachari and M. Ray, "Effect of prism material on design of surface plasmon resonance sensor by admittance loci method," Front. Optoelectron. **6**, 185–193 (2013).
138. B. Meshginqalam and J. Barvestani, "Aluminum and phosphorene based ultrasensitive SPR biosensor," Opt. Mater. **86**, 119–125 (2018).
139. B. M. Younis, N. Y. M. Dawood, A. E. S. Abd-Elkader, D. Furniss, M. Farries, S. Phang, T. M. Benson, A. B. Seddon, M. F. O. Hameed, and S. S. A. Obayya, "Simulation of a Sensitive Mid-infrared (MIR) D-Shaped Optical Fiber Water Pollutant Sensor," Plasmonics **19**, 1823–1838 (2023).
140. G. Mohanty and B. K. Sahoo, "III-V nitrides and performance of graphene on copper plasmonic biosensor," Superlattices Microstruct. **93**, 226–233 (2016).
141. G. Mohanty, B. K. Sahoo, and J. Akhtar, "Comparative analysis for reflectivity of graphene based SPR biosensor," Opt. Quant. Electron. **47**, 1911–1918 (2015).
142. J. Homola, *Surface Plasmon Resonance Based Sensors* (Springer Berlin Heidelberg, 2006), Vol. 4.
143. T. M. S. Ashrafi and G. Mohanty, "Sensitivity calculation for different prism material based surface plasmon resonance sensor: a comparative study," J. Phys. Conf. Ser. **2267**, 012089 (2022).
144. C. Simmonds, "Alcohol: its production, properties, chemistry, and industrial applications," Nature **104**, 431–432 (1920).

145. M. S. Anower, M. M. Rahman, and M. S. Rahman, "Hybrid heterostructures for SPR biosensor," in *Biosensors-Current and Novel Strategies for Biosensing,* L. J. Villarreal-Gómez and A. L. Iglesias, eds. (IntechOpen, 2021), p. 157.

146. L. Wu, J. Guo, Q. Wang, S. Lu, X. Dai, Y. Xiang, and D. Fan, "Sensitivity enhancement by using few-layer black phosphorus-graphene/TMDCs heterostructure in surface plasmon resonance biochemical sensor," Sens. Actuators. B Chem. **249**, 542–548 (2017).

147. G. Mohanty, B. K. Sahoo, and J. Akhtar, "Performance of graphene-on-gold SPR biosensor using wurtzite nitrides," in *2016 International Symposium on Electronics and Smart Devices (ISESD)* (2016), pp. 219–224.

148. T. M. S. Ashrafi and G. Mohanty, "High-performance SPR sensor using wurtzite nitride semiconductors and TMDC: a comparative study," Plasmonics **19**, 817–823 (2023).

149. W. N. Hansen, "Electric fields produced by the propagation of plane coherent electromagnetic radiation in a stratified medium," J. Opt. Soc. Am. **58**, 380–390 (1968).

150. T. M. S. Ashrafi and G. Mohanty, "Highly sensitive GaN-WS2-based surface plasmon resonance sensor: a theoretical approach," Plasmonics **17**, 1673–1680 (2022).

151. T. M. S. Ashrafi and G. Mohanty, "High-performance plasmonic sensor using indium nitride–tungsten disulphide heterostructure for bio-sensing applications," Iran. J. Sci. **48**, 255–259 (2024).

152. E. N. Lazareva and V. V. Tuchin, "Measurement of refractive index of hemoglobin in the visible/NIR spectral range," J. Biomed. Opt. **23**, 035004 (2018).

153. N. A. S. Omar, Y. W. Fen, J. Abdullah, M. H. M. Zaid, and M. A. Mahdi, "Structural, optical and sensing properties of CdS-NH2GO thin film as a dengue virus E-protein sensing material," Optik. **171**, 934–940 (2018).

154. W. Du and F. Zhao, "Graphene/Au/SiC Optical Waveguide-Based Surface Plasmon Resonance Sensor for Chemical and Biomedical Sensing in

Aqueous Medium," ECS Meet. Abstr. **MA2020-01**, 2378 (2020).

155. S. A. Zynio, A. V Samoylov, E. R. Surovtseva, V. M. Mirsky, and Y. M. Shirshov, "Bimetallic layers increase sensitivity of affinity sensors based on surface plasmon resonance," Sensors **2**, 62–70 (2002).
156. R. Kashyap, S. Chakraborty, S. Swarnakar, G. Humbert, S. Zeng, and B. Mondal, "FWHM and sensitivity study of bimetallic SPR sensor chip," in *2019 IEEE International Conference on Electrical, Computer and Communication Technologies (ICECCT)* (2019), pp. 1–4.
157. A. L. C. M. D. Silva, M. G. Gutierres, A. Thesing, R. M. Lattuada, and J. Ferreira, "SPR biosensors based on gold and silver nanoparticle multilayer films," J. Braz. Chem. Soc. **25**, 928–934 (2014).
158. S. H. Kim, T. U. Kim, H. Y. Jung, H. C. Ki, D. G. Kim, and B. T. Lee, "The Effect of Au/Ag Bimetallic Thin-Films on Surface Plasmon Resonance Properties Comparing with Those of Au and Ag Single Thin-Films," J. Nanosci. Nanotechnol. **18**, 1777–1781 (2017).
159. T. M. S. Ashrafi and G. Mohanty, "Single and bimetal-based surface plasmon resonance sensor using AlN-TMDC heterostructure: a comparison study," Opt. Quant. Electron. **55**, 59 (2023).
160. A. Shalabney and I. Abdulhalim, "Figure-of-merit enhancement of surface plasmon resonance sensors in the spectral interrogation," Opt. Lett. **37**, 1175 (2012).
161. F. A. O. Joint, *Joint Fao/Who Food Standards Programme Codex Alimentarius Commission 37th Session: Report of the Eighth Session of the Codex Committe on Contaminants in Foods* (2014).
162. T. Damto, "A review on effect of adulteration on honey properties," SSRN Electron. 3359494 (2019).
163. M. F. N. Akhmazillah, M. M. Farid, and F. V. M. Silva, "High pressure processing (HPP) of honey for the improvement of nutritional value," Innov. Food Sci. Emerg. Technol. **20**, 59–63 (2013).
164. S. Samarghandian, T. Farkhondeh, and F. Samini, "Honey and health: a review of recent clinical research," Pharmacogn. Res. **9**, 121–127 (2017).
165. S. Bogdanov, T. Jurendic, R. Sieber, and P. Gallmann, "Honey for nutrition

and health: a review," J. Am. Coll. Nutr. **27**, 677–689 (2008).

166. R. Fakhlaei, J. Selamat, A. Khatib, A. Faizal, A. Razis, R. Sukor, S. Ahmad, and A. A. Babadi, "The toxic impact of honey adulteration: a review," Foods **9**, 1538 (2020).
167. M. B. Jaafar, M. B. Othman, M. Yaacob, B. A. Talip, M. A. Ilyas, N. H. Ngajikin, and N. A. M. Fauzi, "A review on honey adulteration and the available detection approaches," Int. J. Integr. Eng. **12**, 125–131 (2020).
168. M. García-Alvarez, J. F. Huidobro, M. Hermida, and J. L. Rodríguez-Otero, "Major components of honey analysis by near-infrared transflectance spectroscopy," J. Agric. Food Chem. **48**, 5154–5158 (2000).
169. O. Anjos, M. G. Campos, P. C. Ruiz, and P. Antunes, "Application of FTIR-ATR spectroscopy to the quantification of sugar in honey," Food Chem. **169**, 218–223 (2015).
170. R. Kizil and J. Irudayaraj, "Spectroscopic technique: fourier transform raman (FT-Raman) spectroscopy," in *Modern Techniques for Food Authentication*, D. W. Sun, ed., 2nd ed. (Academic Press, 2018), pp. 193–217.
171. A. Naila, S. H. Flint, A. Z. Sulaiman, A. Ajit, and Z. Weeds, "Classical and novel approaches to the analysis of honey and detection of adulterants," Food Control **90**, 152–165 (2018).
172. J. W. White, K. Winters, P. Martin, and A. Rossmann, "Stable carbon isotope ratio analysis of honey: validation of internal standard procedure for worldwide application," J. AOAC Int. **81**, 610–619 (1998).
173. L. Wiest, A. Buleté, B. Giroud, C. Fratta, S. Amic, O. Lambert, H. Pouliquen, and C. Arnaudguilhem, "Multi-residue analysis of 80 environmental contaminants in honeys, honeybees and pollens by one extraction procedure followed by liquid and gas chromatography coupled with mass spectrometric detection," J. Chromatogr. A **1218**, 5743–5756 (2011).
174. S. Carabetta, R. Di Sanzo, L. Campone, S. Fuda, L. Rastrelli, and M. Russo, "High-performance anion exchange chromatography with pulsed amperometric detection (HPAEC–PAD) and chemometrics for

geographical and floral authentication of honeys from southern Italy (Calabria region)," Foods **9**, 1625 (2020).

175. L. Mehryar and M. Esmaiili, "Honey & honey adulteration detection : a review," in *Proceedings of 11th International Congress on Engineering and Food* (2011), Vol. 3, pp. 1713–1714.
176. C. Cordella, J. P. Faucon, D. Cabrol-Bass, and N. Sbirrazzuoli, "Application of DSC as a tool for honey floral species characterization and adulteration detection," J. Therm. Anal. Calorim. **71**, 279–290 (2003).
177. N. M. Razali, A. N. Mazlan, M. F. Salebi, H. Mohamed, and S. Ambran, "Optical fiber tip sensor for glucose-adulterated honey detection," Telkomnika **17**, 2445–2450 (2019).
178. N. Bidin, N. H. Zainuddin, S. Islam, M. Abdullah, F. M. Marsin, and M. Yasin, "Sugar detection in adulterated honey via fiber optic displacement sensor for food industrial applications," IEEE Sens. J. **16**, 299–305 (2016).
179. Y. Song, H. C. Huang, W. Lu, N. Li, J. Su, S. B. Cheng, Y. Lai, J. Chen, and J. Zhan, "Ag@WS2 quantum dots for surface enhanced raman spectroscopy: enhanced charge transfer induced highly sensitive detection of thiram from honey and beverages," Food Chem. **344**, 128570 (2021).
180. X. Duan, Q. Liu, G. Wang, and X. Su, "WS2 quantum dots as a sensitive fluorescence probe for the detection of glucose," J. Lumin. **207**, 491–496 (2019).
181. D. C. Agrawal, A. Yadav, V. K. Singh, A. Srivastava, and A. M. Kayastha, "Immobilization of fenugreek β-amylase onto functionalized tungsten disulfide nanoparticles using response surface methodology: its characterization and interaction with maltose and sucrose," Colloids. Surf. B Biointerfaces. **185**, 110600 (2020).
182. Vikas, M. K. Yadav, P. Kumar, and R. K. Verma, "Detection of adulteration in pure honey utilizing Ag-graphene oxide coated fiber optic SPR probes," Food Chem. **332**, 127346 (2020).
183. N. H. Zainuddin, Y. W. Fen, A. A. Alwahib, M. H. Yaacob, N. Bidin, N. A. S. Omar, and M. A. Mahdi, "Detection of adulterated honey by surface plasmon resonance optical sensor," Optik. **168**, 134–139 (2018).

184. Z. Can, O. Yildiz, H. Sahin, E. Akyuz Turumtay, S. Silici, and S. Kolayli, "An investigation of Turkish honeys: their physico-chemical properties, antioxidant capacities and phenolic profiles," Food Chem. **180**, 133–141 (2015).

185. E. I. Geană, C. T. Ciucure, D. Costinel, and R. E. Ionete, "Evaluation of honey in terms of quality and authenticity based on the general physicochemical pattern, major sugar composition and δ13C signature," Food Control **109**, 106919 (2020).

186. D. P. Aykas, "Determination of possible adulteration and quality assessment in commercial honey," Foods **12**, 523 (2023).

187. B. Karki, A. Jha, A. Pal, and V. Srivastava, "Sensitivity enhancement of refractive index-based surface plasmon resonance sensor for glucose detection," Opt. Quant. Electron. **54**, 595 (2022).

188. N. Abbas, M. R. Shad, M. Hussain, S. M. Z. Mehdi, and U. Sajjad, "Fabrication and characterization of silver thin films using physical vapor deposition, and the investigation of annealing effects on their structures," Mater. Res. Express **6**, 116437 (2019).

189. M. Mikulics, M. Kočan, A. Rizzi, P. Javorka, Z. Sofer, J. Stejskal, M. Marso, P. Kordoš, and H. Lüth, "Growth and properties of GaN and AlN layers on silver substrates," Appl. Phys. Lett. **87**, 212109 (2005).

190. Y. Yu, P. W. K. Fong, S. Wang, and C. Surya, "Fabrication of WS2/GaN p-n junction by wafer-scale WS2 thin film transfer," Sci. Rep. **6**, 37833 (2016).

191. X. Sun, J. Fan, C. Fu, L. Yao, S. Zhao, J. Wang, and J. Xiao, "WS2 and MoS2 biosensing platforms using peptides as probe biomolecules," Sci. Rep. **7**, 10290 (2017).

192. Y. Jiao, J. Li, J. Xiang, and Z. Chen, "Tungsten disulfide nanosheets-based colorimetric assay for glucose sensing," Spectrochim. Acta. A. Mol. Biomol. Spectrosc. **242**, 118706 (2020).

APPENDIX

Explanation of Boundary Conditions in Programming

Boundary conditions are critical in computational models and simulations as they define how the system interacts with its environment, ensuring mathematical accuracy and physical relevance. In the context of the numerical and simulation models described, the boundary conditions implemented are tailored for the study of SPR sensors.

1. Electromagnetic Boundary Conditions

- Continuity of Electric and Magnetic Fields: At the interface of two materials, the tangential components of the electric field (E_t) and magnetic field (H_t) are continuous. This ensures that the boundary correctly models the interaction of light with the material layers.

$$E_{t1} = E_{t2} \text{ and } H_{t1} = H_{t2}$$

2. Geometric Boundary Conditions

- Layer Thickness: Each material layer's thickness is explicitly defined and optimized to achieve minimum reflectance. These thicknesses are critical in ensuring the propagation of SPPs and enhancing sensitivity.

3. Periodic and Port Conditions in COMSOL

- Periodic Conditions: The simulation assumes periodicity in certain geometries to model the repeated structures effectively. Floquet periodicity is applied to match the wave vector at periodic boundaries.
- Port Boundary Conditions: Ports are defined for wave excitation and transmission. The input port specifies the angle of incidence, and the output port measures the transmitted wave properties. This setup is essential for accurate SPR resonance modelling.
- Perfect Electric Conductor (PEC): The electric field is set to zero on a boundary representing a perfect conductor.

- Perfect Magnetic Conductor (PMC): Similar to PEC but applied to the magnetic field, setting the tangential component of the magnetic field to zero.
- Impedance Boundary Condition: This can be used to model wave propagation in structures where the electric and magnetic fields are related to the impedance at the boundary.
- Scattering Boundary Condition: This is used to simulate open domain problems where waves can scatter without reflection, commonly implemented through PML (Perfectly Matched Layer).

These boundary conditions collectively ensure the fidelity of simulations, whether conducted using MATLAB or COMSOL Multiphysics. They form the foundation for accurately predicting SPR phenomena and optimizing sensor performance.

LIST OF PUBLICATIONS BY AUTHOR

International/ National Journals

- **T. M. S. Ashrafi** and G. Mohanty, "Sensitivity calculation for different prism material based surface plasmon resonance sensor: A comparative study," in *Journal of Physics: Conference Series* (2022), Vol. 2267.
- **T. M. S. Ashrafi** and G. Mohanty, "Highly Sensitive GaN-WS_2-Based Surface Plasmon Resonance Sensor: a Theoretical Approach," Plasmonics **17**, 1673–1680 (2022).
- **T. M. S. Ashrafi** and G. Mohanty, "Single and bimetal-based surface plasmon resonance sensor using AlN-TMDC heterostructure: a comparison study," Opt. Quant. Electron. **55**, 59 (2022).
- **T. M. S. Ashrafi** and G. Mohanty, "High-Performance SPR Sensor Using Wurtzite Nitride Semiconductors and TMDC: a Comparative Study," Plasmonics **19**(2), 817-823 (2023).
- **T. M. S. Ashrafi** and G. Mohanty, "High-Performance Plasmonic Sensor Using Indium Nitride–Tungsten Disulphide Heterostructure for Bio-Sensing Applications," Iran. J. Sci. **6**, (2024).
- **T. M. S. Ashrafi** and G. Mohanty, "Ultra-sensitive plasmonic sensor for detecting honey adulteration with III-V Nitride and Tungsten Disulfide. " Sensing and Imaging **25**, 19 (2024).
- **T. M. S. Ashrafi** and G. Mohanty, "Surface Plasmon Resonance Sensors: A Critical Review of Recent Advances, Market Analysis, and Future Directions," Plasmonics, (2025)

International/ National conference series / Symposium

Oral Presentations

- **T. M. S. Ashrafi** and G. Mohanty, "Comparative study on the performance of an SPR sensor using Wurtzite Nitride semiconductors with TMDC heterostructure," 4th International Conference on Recent Advances in Findamental and Applied Sciences (RAFAS 2023), Punjab, India, during 24th-25th March, 2023. (Awarded

Second best Position in oral presentation)

- **T. M. S. Ashrafi** and G. Mohanty, "Design and simulation of surface plasmon resonance sensor using a heterostructure InN-WS_2 for biosensing application," 7th International Conference on Recent Advances in Material Chemistry Department of Chemistry (ICRAMC-2023), Kattankulathur, India, during 16th-18th February 2023.
- **T. M. S. Ashrafi** and G. Mohanty, "Exploring performance parameters of AlN-TMDC Heterostructures based SPR sensor," 5th International Conference on Recent Advances in Findamental and Applied Sciences (RAFAS 2024), Punjab, India, during 19th-20th April, 2024 .

Poster Presentation

- **T. M. S. Ashrafi** and G. Mohanty, " Sensitivity calculation for different prism material-based surface plasmon resonance sensor: A comparative study," 3rd International Conference on Recent Advances in Findamental and Applied Sciences (RAFAS 2021), Punjab, India, during 25th-26th June, 2021.
- **T. M. S. Ashrafi** and G. Mohanty, "Detection of sugar adulterants using an InN-WS_2 heterostructure SPR sensor in honey samples from local markets," International Conference on Advanced Sustainable Futuristic Materials (ASFM 2024), Nagpur-440024, India, during 26th-27th April, 2024.